

Design, Fabrication and Characterization of Terahertz Quantum-well Photodetectors

by

Shengxi Huang

Submitted to the Department of Electrical Engineering and Computer
Science

in partial fulfillment of the requirements for the degree of

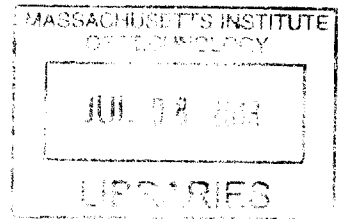
Master of Science in Electrical Engineering and Computer Science

at the

MASSACHUSETTS INSTITUTE OF TECHNOLOGY

June 2013

ARCHIVES



© Massachusetts Institute of Technology 2013. All rights reserved.

Author
Department of Electrical Engineering and Computer Science
May 22, 2013

Certified by
Qing Hu
Professor
Thesis Supervisor

Accepted by
Leslie A. Kolodziejski
Chairman, Department Committee on Graduate Theses

Design, Fabrication and Characterization of Terahertz Quantum-well Photodetectors

by

Shengxi Huang

Submitted to the Department of Electrical Engineering and Computer Science
on May 22, 2013, in partial fulfillment of the
requirements for the degree of
Master of Science in Electrical Engineering and Computer Science

Abstract

Terahertz (THz) photodetectors are important in the fully exploration and development of electromagnetic spectrum. However, a fast and sensitive THz photodetector ready for array integration is not available. A THz Quantum-well Photodetector (QWP) has the properties of being fast, sensitive, low-noise, and narrow-band. It is promising for large-array integration for THz imaging. In addition, a THz QWP-LED (Light-Emitting Diode) can upconvert the THz to NIR radiation and useful for THz imaging in Focal-Plane Array (FPA).

In this thesis project, the theory of the intersubband transition and carrier transport in a THz QWP is studied. The design, fabrication, measurement-system build-up, and characterization are performed. In addition, the design and fabrication process of THz QWP-LED are also carried out. Such devices have potential applications in many fields such as biology, medication and security.

Thesis Supervisor: Qing Hu

Title: Professor

Acknowledgments

There are many people that I would like to thank for their support and help during the period that this thesis work is being performed.

First, I would like to thank my advisor Prof. Qing Hu. He gave me the opportunity to work on this project. I am deeply impressed by Qing's persistence and endless pursuit for truth, which is the main motivation for me to continue the work in face of setbacks. From Qing, I also learn to be more resourceful and active as a researcher. I feel so lucky to have the chance to work with him and be his student.

I would like to thank our collaborators, Prof. H.C. Liu from Shanghai Jiaotong University, for the collaboration of this work and Dr. John Reno from Sandia National Lab as well for the MBE growth.

Many thanks should also be given to Xerox Corporation for their generous sponsor for my second year's work and study.

I would like to thank Prof. Leslie Kolodziejski, who is the EECS graduate officer and my mentor. She generously provided me with the BCB and adhesion promotor for my fabrication. She also guided me in terms of study, research and life. She offered me numerous helpful advices and informative discussions.

I am also deeply grateful to my dear group mates. Ivan Chan has been mentoring me from the very beginning when I joined the group. He is always so kind and patient in teaching and helping me on every aspect of my work. Wilt Kao offered me a lot of help and discussions on the electromagnetic analysis, fabrication, and measurement. David Burghoff had a lot of helpful discussion with me in terms of theory, design, and measurement, and his optical expertise is very important in the process I work on this project. Ningren Han shares a lot of his insights and experiences with me. It is also nice to have Xiaowei Cai, Qi Qin, Alan Lee, Amir Tavallae as supportive and enthusiastic fellows.

I would like to thank my undergraduate advisor, Prof. Zhiping Yu. By corresponding and talking with him, I never cease to feel enlightened and delighted. I am so lucky to have him as my undergraduate thesis supervisor, who turns out to become

my life-long advisor.

There are so many of my friends that I would like to thank. They offer me endless happiness and gave me unselfish care. Please forgive me for being unable list the names one by one.

Last but not the least, I would like to give my great gratitude to my family, especially my parents. No matter how far away I am from them in terms of distance, their love never fails to embrace me at any time and anywhere. I could never have this work done without you.

Contents

1	Introduction	15
1.1	Terahertz and Terahertz Gap	15
1.2	Terahertz Photodetectors	16
1.3	Review of THz QWP Development	18
1.3.1	Operation Principle of THz QWP	18
1.3.2	Optimization Method of THz QWP Design	20
1.4	Introduction of THz QWP-LED	25
1.5	Thesis Overview	26
2	Theory of Intersubband Transitions and Carrier Transport in QWP	29
2.1	Theory of Intersubband Transition	29
2.2	Theory of Carrier Transport in QWP	37
2.2.1	Dark Current	39
2.2.2	Photocurrent	47
2.3	Performance Analysis of QWP	52
2.3.1	QWP Noise	53
2.3.2	QWP Detectivity and Noise Equivalent Power	55
3	Design of QWP	61
3.1	Design of MQW Structure	61
3.2	Design of Grating Coupler	67
4	Fabrication of QWP	89

4.1	Fabrication of 45° QWP	89
4.2	Fabrication Steps of Grating Coupler QWP	95
4.3	Fabrication Steps of QWP-LED	99
5	Device Characterization	103
5.1	Measurement System Build-up	103
5.1.1	The Build-up of Cryogenic Dewar	104
5.1.2	The Build-up of Low-noise Electronic Measurement System . .	112
5.2	Measurement Results	121
6	Conclusion and Future Work	133
6.1	Conclusion	133
6.2	Future Work	134
A	Device Mounts used in dewar	135

List of Figures

1-1	Electromagnetic spectrum and the corresponding solid-state sources. There is a THz gap which few sources and reach.	16
1-2	Performance of Solid-state Sources in EM spectrum.	17
1-3	Intersubband absorptions of electrons and holes in a quantum well.	19
1-4	GaAs/Al _x Ga _{1-x} As MQW in a QWP. Upon THz radiation, electrons in the GaAs ground states are excited to the excited subbands in the quantum wells (GaAs regions) which then transport to the contact under voltage bias, forming the photoconductive current.	19
1-5	QWP structure with 45° incident radiation.	21
1-6	(a) Schematic of THz QWP with 1D metal grating on top of the device to increase absorption. (b) THz QWP with grating coupler developed by Zhang et al.	22
1-7	Simulated absorption efficiency of THz QWP with different 1D metal grating couplers on the top.	23
1-8	Dark current vs. bias voltage in different temperatures. In the simulation, mobility value is carefully selected under different temperatures and good match between simulation and experiment is obtained.	24
1-9	Energy band structure of QWP-LED.	26
1-10	Schematics of THz QWP-LED. (a) THz QWP-LED with 45° incidence (or other tilted angle). (b) THz QWP-LED with 1D metal grating on top of the device to increase absorption.	27

2-1	Illustration of the QWP MQW, incident THz radiation and polarization. The incident angle θ is shown.	34
2-2	GaAs/ $\text{Al}_x\text{Ga}_{1-x}\text{As}$ MQW in a QWP. Upon THz radiation, electrons in the GaAs ground states are excited to the excited subbands in the quantum wells (GaAs regions) which then transport to the contact under voltage bias, forming the photoconductive current.	38
2-3	The dark current model.	38
2-4	The band structure of one quantum well in QWP.	41
2-5	The scattering-assisted process in k-space.	44
2-6	The mechanism of the carrier transport across a quantum well under illumination.	48
3-1	Simulation results of absorption coefficient vs. frequency.	64
3-2	The absorption coefficient at 4THz vs. well width for different Aluminum fractions.	65
3-3	The tunneling current between each wells in MQW structure vs barrier widths.	67
3-4	The 2D simulation model for the QWP EM simulation.	69
3-5	A simulated figure of the 1D grating coupler QWP.	72
3-6	Simulated color figures of the 1D grating coupler QWP.	73
3-7	The simulated absorption efficiency vs. frequency of a THz microcavity-coupled QWP.	75
3-8	The layered structure of THz QWP-LED.	77
3-9	The simulated results for THz QWP-LED with the MQW structure described above but varying grating coupler periods and duty cycles.	79
3-10	The simulated absorption efficiency spectrum in THz QWP-LED with different p-type bottom contact layer thicknesses t_{pot}	83
3-11	The simulated absorption efficiency spectrum in THz QWP-LED with the p-type plasma reflector doping concentrations p_{PR} different from the optimized value $5 \times 10^{19} \text{cm}^{-3}$	84

3-12	The simulated absorption efficiency spectrum in THz QWP-LED with the p-type plasma reflector thickness $t_{PR} = 400nm$, which is different from the optimized value $800nm$	86
4-1	The flow chart of the processing steps of 45° THz QWP.	90
4-2	Photo of the device surface after this layer of photoresist is developed.	92
4-3	The SEM image of the 45° QWP after all the fabrication steps except for the last 45° facet lapping.	95
4-4	The flow chart of the processing steps of grating coupler THz QWP.	96
4-5	The top views of grating coupler THz QWP at the end of SiN mask patterning and after mesa etch and SiN mask removal.	97
4-6	The SEM image of the grating coupler QWP after the aforementioned processing steps.	99
4-7	The flow chart of the processing steps of grating coupler THz QWP-LED.	100
5-1	The layout of the LHE dewar used in the experiment.	105
5-2	Temperature vs. time curves during the cryogenic tests of the LHE dewar. Detailed description of each curve can be referred to the test.	111
5-3	3D plot of THz QWP mounted on the He tank inside the dewar. Incident THz radiation and dewar window are shown as well.	113
5-4	The top view of the dewar inner side layout.	114
5-5	A close view of the dewar inner settings with 45° THz QWP mounted.	115
5-6	THz 45° QWP mounted on device mounts.	116
5-7	The side view of the 45° QWP mounted on device mounts. The figure clearly shows the 45° facet.	116
5-8	The QWP measurement diagram.	118
5-9	Dewar and the metal box attached to it.	120
5-10	M0570's current-voltage character (in both linear and semi-log scales) in 4K in four cases: Dark, 300K Background, Blackbody radiation, and blackbody radiation with Aluminum foil covering the window.	122
5-11	The spectra of the DTGS detector and THz QWP M0570.	125

5-12	The I-V curve of THz QWP VB0570 at 4K.	126
5-13	The spectrum of one THz QWP VB0570.	128
5-14	The I-V curves for two of the eight grating coupler QWPs in wafer VB0572.	131
A-1	Mechanical drawings of the device mounts used for the 45° THz QWP.	136
A-2	Mechanical drawings of the device mounts used for the grating coupler THz QWP.	137
A-3	Mechanical drawings of the device mounts used for the grating coupler THz QWP-LED.	137

List of Tables

3.1	For different Aluminum fractions, the well widths for 1 st excited s-tate to align with conduction band, the peak absorption frequencies at alignment, and the corresponding peak absorption coefficients are shown in the table.	66
5.1	Dark current noise and dark current gain measured from the grating coupler THz QWP, wafer VB0572.	130

Chapter 1

Introduction

1.1 Terahertz and Terahertz Gap

Terahertz (1-10 THz, $\hbar\omega = 4 - 40meV$, and $\lambda = 30 - 300\mu m$) frequency range is very important in a variety of fields such as biology, medicine, chemical detection and communication [1, 2]. THz corresponds to the rotational and vibrational energies in many biological molecules, thus it is useful in the detection and sensing of biomolecules, chemical gas, and drugs. THz wave is remarkably subjective to water absorption, and because of the water concentration difference between cancerous cells and normal cells, THz can be used in biomedical imaging. Due to the higher frequency of THz than the current communication band, THz can be applied in high-speed, broad-band wireless communications and signal processing.

However, Terahertz range is the least studied and the least developed electromagnetic (EM) spectrum. The main reasons are the lack of powerful THz sources and the lack of fast and sensitive THz detectors. As shown in Fig. 1-1 and Fig.1-2, below 1THz, electronic sources such as transistors are the major EM source, but the frequencies they can provide are limited by carrier transit time and RC delay, and the source power scales as $1/f^4$, where f stands for the frequency. Above 10 THz, photonic sources such as laser diodes are the major sources, but the frequencies they can provide are limited by the material energy gap. Even for the ultra low-bandgap material Pb-salt, the laser frequency is larger than 10 THz. Additionally, as the frequency de-

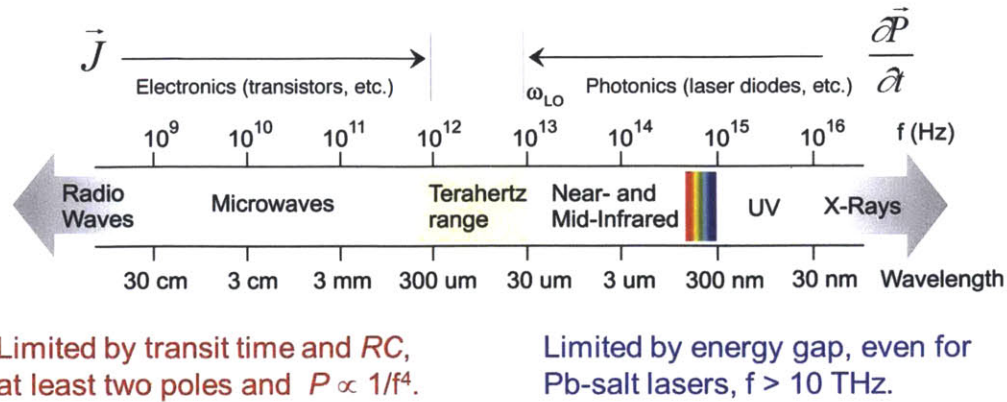


Figure 1-1: Electromagnetic spectrum and the corresponding solid-state sources. There is a THz gap which few sources and reach.

creases, the power of the laser diodes decreases rapidly and they are more subjective to thermal fluctuation, especially, for low-frequency photonic sources, temperature must be low enough to minimize the effect of thermal disturbance ($k_B T \ll \hbar\omega$).

To overcome the lack of the THz sources, THz Quantum Cascade Lasers (QCLs) [4, 5, 6, 7] have been developed in recent years and many performance records have been achieved. For example, the highest pulse-mode operating temperature reached 199K, the highest continuous-wave (CW) mode operating temperature reached 117K, the highest power achieved 250 mW, and the tuning range of exceeded 300GHz, etc.

Besides the THz sources, another challenge in THz study lies in the lack of fast and sensitive THz detectors. The main theme of this thesis is to develop a fast and sensitive THz photodetector called QWP (Quantum-well Photodetector).

1.2 Terahertz Photodetectors

In the aspect of detection mechanism, THz photodetectors can be categorized into two types: thermal detectors and semiconductor photoconductors.

Thermal detectors are usually broad-band and of low speed. Their operation principles are the change of electric properties (e.g. polarization, conductance, etc.) due to the thermal effect from THz radiation. Lithium Tantalate (LiTaO_3) pyroelectric detectors [8, 9] have quite flat spectrum response in THz and near-infrared (NIR)

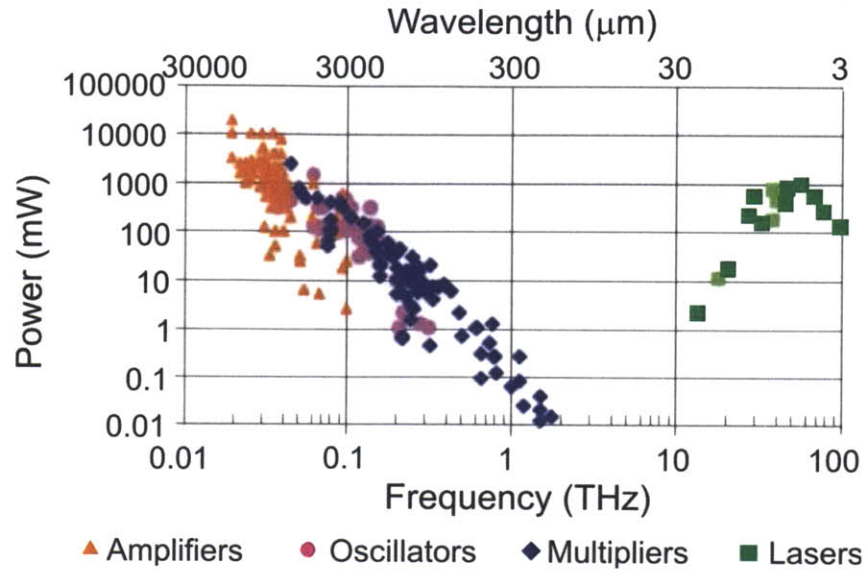


Figure 1-2: Performance of Solid-state Sources in EM spectrum. Plot adapted from [3].

range, so they are usually used to calibrate the laser-emission power [10] and the array of which were used to characterize the laser beam pattern [11]. Other examples of THz thermal detectors include deuterated triglycine sulfate (DTGS) pyroelectric detector [12, 13], and Si bolometer [14, 15]. They are usually used in the FTIR (Fourier Transform Infrared Spectrometer) to measure the absorption and reflection spectra of materials.

THz semiconductor photoconductors are faster and of narrower band compared to thermal detectors. They are based on the principle of carrier excitation from the lower energy level to the higher energy level due to THz radiation. Doped Ge: Ga photoconductor [16, 17] uses the excitation of electrons from the valence band to the shallow acceptor level. N-type GaAs detector [18] utilizes the transition between different atomic energy levels and sub-levels (due to Zeeman Effect with magnetic field). Homojunction and Heterojunction Interfacial Workfunction Internal Photoemission (HIWIP and HEIWIP) far-infrared detectors [19, 20, 21, 22] are based on the transition of holes from Fermi level of the intrinsic material to the valence band of the neighboring material. These devices have been used in astrophysics [17].

In the recent 20 years, QWP (Quantum-Well Photodetector) [23] has been de-

veloped as a fast and narrow-band photodetector in mid-infrared (MIR) range. It is based on the electron transition between different subbands in the quantum wells formed by MQWs (Multi-Quantum Wells). In recent years, due to the development of THz sources, the operating range of MIR QWP has been extended to THz range [24, 25, 26]. The main goal of this project is to develop a THz QWP operating at around 4 THz with fast speed and low noise. Therefore such a QWP can be conveniently integrated in detector arrays and be applied in real-time THz imaging.

1.3 Review of THz QWP Development

1.3.1 Operation Principle of THz QWP

As stated above, QWP is based on the inter-subband excitation of electrons in the quantum wells formed by MQWs. In quantum wells, the energy levels of the electrons and holes are discretized due to quantum effect, and electrons and holes can be excited from the lower subband to the higher subband if the incoming photon energy equals the subband energy difference, as shown in Fig. 1-3. The most widely used material system is GaAs/Al_xGa_{1-x}As, because the crystal lattices of these two materials are very well matched, and the growth and fabrication techniques of these materials have been maturely developed. In order to provide high quality MQW, MBE (Molecular Beam Epitaxy) growth is adopted here to get the QWP structure. Fig. 1-4 shows the formation of photoconductive current in the MQWs. Electrons in each of the quantum wells (GaAs regions) will be excited from the ground state to the excited state when absorbing the incoming photons. If the excited state is aligned well with the conduction band of the barrier material (Al_xGa_{1-x}As), electrons can move freely under voltage bias. Thus, the photoconductive current is formed and is literally proportional to the incident light intensity.

Since THz photons correspond to very low energy (on the order of tens of meV) and thermal fluctuation can easily affect the correct operation of QWP, these THz photodetectors have to operate in cryogenic temperature to satisfy the relation of

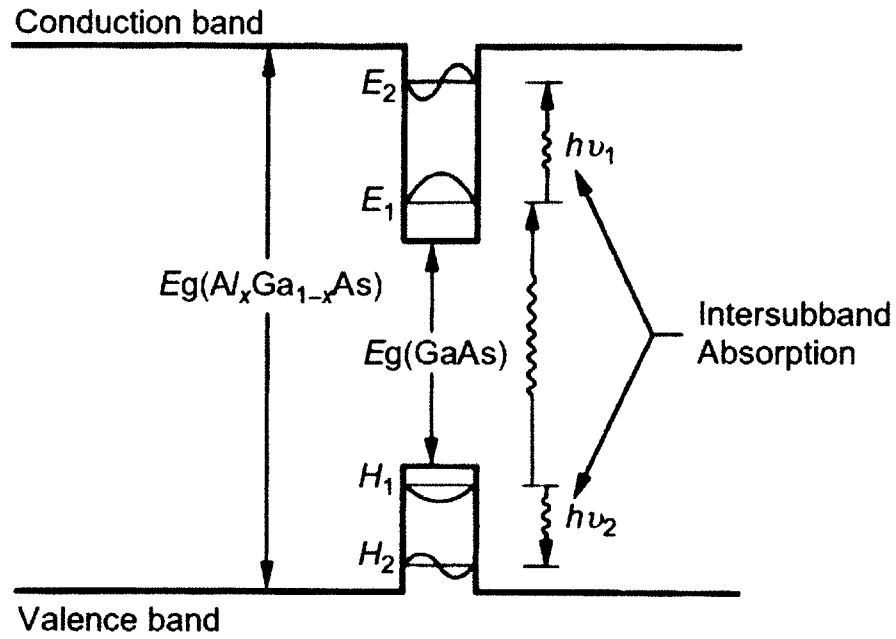


Figure 1-3: Intersubband absorptions of electrons and holes in a quantum well [23].

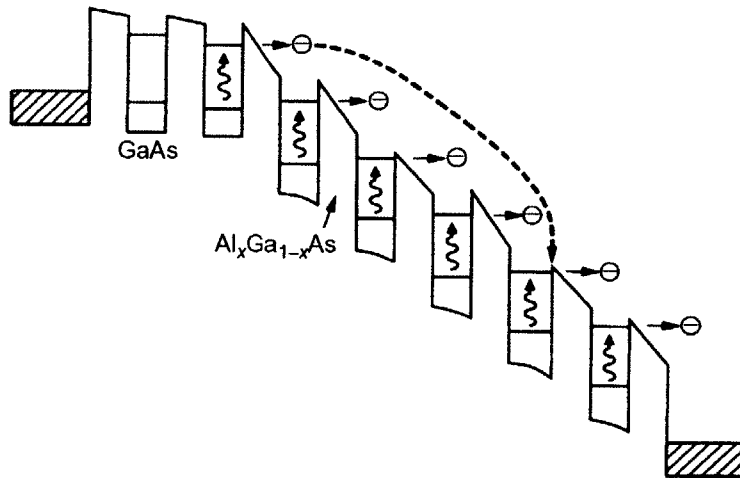


Figure 1-4: GaAs/ $\text{Al}_x\text{Ga}_{1-x}\text{As}$ MQW in a QWP. Upon THz radiation, electrons in the GaAs ground states are excited to the excited subbands in the quantum wells (GaAs regions) which then transport to the contact under voltage bias, forming the photoconductive current [23].

$k_B T \ll \hbar\omega$, where k_B is the Boltzmann constant, T is the temperature, and ω is the circular frequency of the incident light. The QWP in this project aims at 4THz detection, so a cooling down to liquid Helium-4 (LHE) temperature (4.2K under one atmosphere pressure) is appropriate.

1.3.2 Optimization Method of THz QWP Design

In the design of QWP MQW, several parameters are taken into consideration: Aluminum fraction, doping concentration, well and barrier width. Aluminum fraction controls the conduction band offset (barrier height) and thus contributing to the positions of the electron subbands. Doping concentration alters the light absorption efficiency and the intensity of the photoconductive current. Barrier and well widths can also change the energy subbands positions. An ideal QWP operation requires high light absorption efficiency, low capture probability (the probability that the electrons are captured from barrier conduction band back into the well region), high escape probability (the probability that an electron is escaped from the excited state in the well region into the conduction band in the barrier region), low dark current, high responsivity and low noise. Therefore, a careful selection of these parameters is necessary in designing a fast and sensitive THz QWP.

Increasing Absorption Efficiency

Due to the selection rule of intersubband transition, in n-type QWP, electrons have no response if the polarization of the incoming light is perpendicular to the MQW growth direction. Therefore, two methods can be utilized: 45° incidence (or other tilted angle) and grating coupler (GC).

The method of 45° incidence (or other tilted angle) was used in the early stages of THz QWPs [24, 25], shown in Fig. 1-5. The QWP MQW is MBE grown on the Semi-Insulating (SI) GaAs substrate. One facet of the substrate is lapped 45° for the tilted angle THz incidence. QWP mesa is etched on the GaAs substrate. The top of the mesa and the top plane of the substrate are deposited with metal, forming the

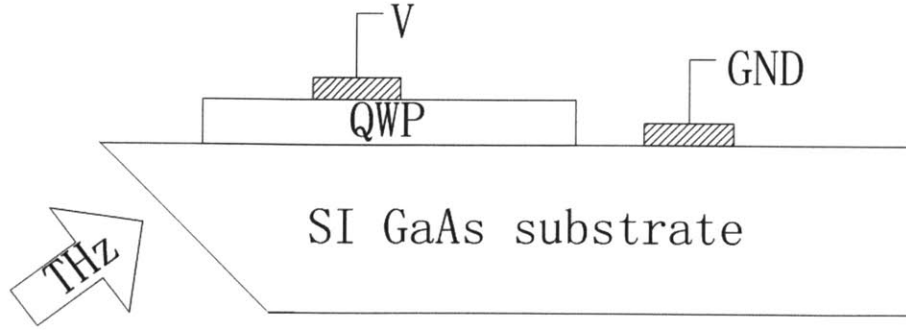


Figure 1-5: QWP structure with 45° incident radiation.

electrodes. These electrodes are shown in shaded area in Fig. 1-5. Since the substrate of THz QWP is lapped 45° on the facet and THz radiation is incident normal to the facet, the polarization of the incident light is 45° with the growth direction, avoiding the vanishing of absorption efficiency due to selection rule. However, this method is still ineffective since only half of the incident power can attribute to the total absorption of THz radiation.

The grating coupler (GC) method has been used recently [26] to increase the absorption efficiency of QWP. The absorption efficiency is defined in Chapter 2. Essentially, it is the ratio of the power absorbed in the active QWP region and the power incident on the QWP. The scheme of the grating coupler structure is shown in Fig. 1-6. In Fig. 1-6a, the schematic of THz QWP with 1D metal grating on top of the device to increase absorption is shown. The QWP MQW is MBE grown on the n+ doped GaAs substrate. QWP mesa is etched on the GaAs substrate. The top of the mesa is deposited with metal grating, which can simultaneously serve as the electrode as well. The other electrode is formed by depositing metal on the bottom of the n+ doped GaAs substrate. The metal grating on top of the mesa is shown in shaded area in the figure. Fig. 1-6b shows the THz QWP with grating coupler developed in [26]. The diffracted modes are shown in the figure, and they can be absorbed by the quantum-well. In this work, 1D metal grating has been deposited on top of THz QWP, see Fig. 1-6a. Additionally, the highly doped contact layer can be used as the plasma reflector region as well to facilitate the absorption because the 0^{th} diffraction mode can be further reflected in the highly doped contact layer and

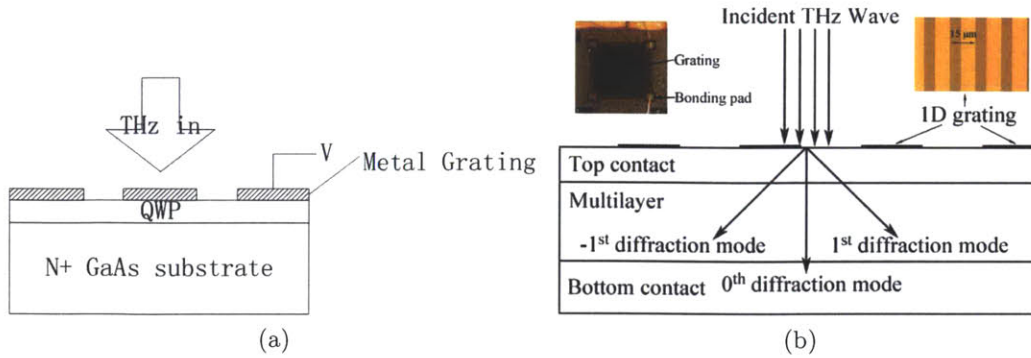


Figure 1-6: (a) Schematic of THz QWP with 1D metal grating on top of the device to increase absorption. (b) THz QWP with grating coupler developed by Zhang et al [26]. The diffracted modes are shown in the figure, and they can be absorbed by the quantum-well.

reach the grating again to be diffracted by metal grating. The simulation using Finite Element Method (FEM) in this thesis project shows that an absorption efficiency of over 80% near 4THz can be achieved by properly selecting the grating parameters, as can be seen in Fig. 1-7. A peak absorption of over 80% at the vicinity of 4 THz can be achieved with grating period p of 16 m, duty cycle DC of 0.4 0.5, top and bottom contact layer doping concentrations of 10^{17} cm^{-3} and $5 \times 10^{18} \text{ cm}^{-3}$. Fig. 1-7 will be revisited and discussed in more detail in Chapter 3.2.

Decreasing Noise

The THz QWP is good candidate for THz array imaging and detection in security applications, because it can provide fast and sensitive THz photodetection. The Noise Equivalent Power (NEP) of THz QWP is estimated to be $\sim 0.01 \text{ pW}/\sqrt{\text{Hz}}$ [25]. In this thesis project, an NEP level of less than $0.01 \text{ pW}/\sqrt{\text{Hz}}$ is estimated based on the proposed structure of QWP and operating environment. Currently, a microbolometer array camera can achieve an NEP as low as $1 \text{ pW}/\sqrt{\text{Hz}}$ (developed by NEC/NICT). A Ge:Ga photodetector can reach the NEP of $0.1 \text{ pW}/\sqrt{\text{Hz}}$, but no arrays have been developed. Therefore, THz QWP with an ultra low NEP is promising to achieve fast THz detection because the integration time is proportional to $(\text{NEP})^2$.

The major noise sources of THz QWP are shot noise, dark current noise, and

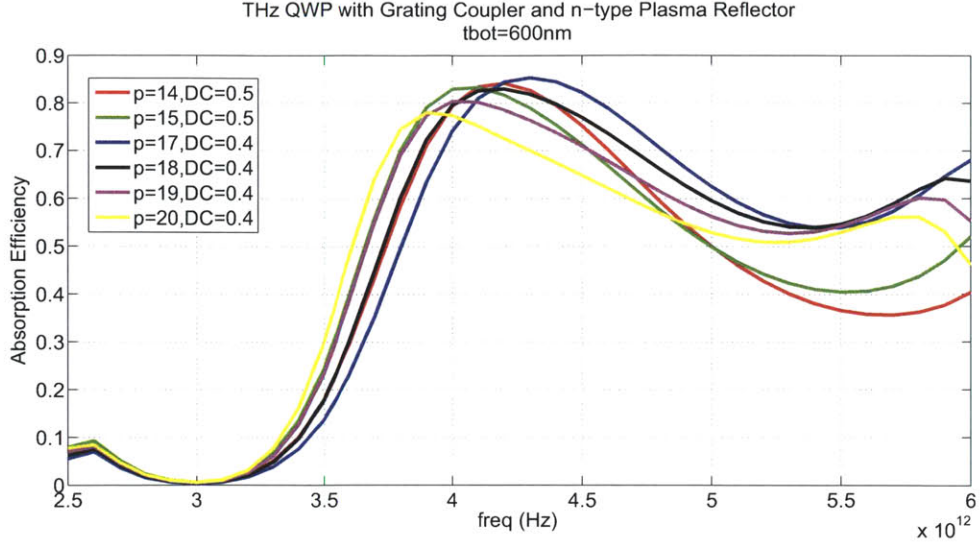


Figure 1-7: Simulated absorption efficiency (defined in Chapter 2) of THz QWP with different 1D metal grating couplers on the top. In the legend, p means grating coupler period and the unit is μm , and DC is the duty cycle of the metal grating. This figure will be revisited and discussed in more detail in Chapter 3.2.

photocurrent noise. Johnson noise (thermal noise) is not important here because THz QWP works in cryogenic temperature. To achieve high responsivity and high detectivity while decreasing NEP, a low dark current level is crucial. There are two models for dark current: 3D drift model and 2D emission-capture model. These two models will be discussed in detail in Chapter 2. Here, we just present a brief overview of both models.

In 3D drift model, the dark current density is thought to be contributed by the electrons in the continuum above the barrier conduction band, therefore it is 3D electron density N_{3D} . The current is evaluated using

$$j_{dark} = eN_{3D}v(F) \quad (1.1)$$

Where $v(F)$ is the carrier drift velocity as a parameter of electric field F . The 2D quantum well effect takes into part in the evaluation of Fermi level which is thought to be the same in both well region and barrier region. The donors in well region are thought to be fully ionized so that a Fermi level can be calculated. By carefully tuning

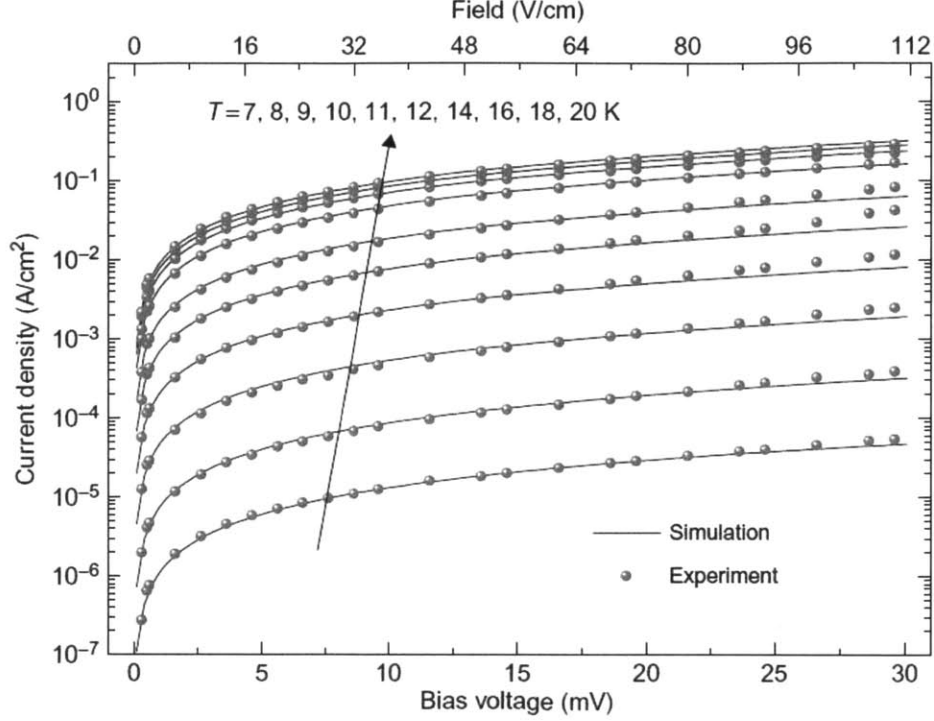


Figure 1-8: Dark current vs. bias voltage in different temperatures [27]. In the simulation, mobility value is carefully selected under different temperatures and good match between simulation and experiment is obtained.

the mobility with temperature, a good match of simulation result and experimental data can be achieved [27], which is also illustrated in Fig. 1-8.

In 2D emission-capture model, attention is focused on the scattering-assisted escape process of the electrons sitting in the ground state of the well region and escaping into the 3D conduction band of the barrier region under photo-excitation [28]. This model becomes relevant when the electric field is low, which is usually the case in the QWP operation. In this model, the dark current is evaluated by

$$j_{dark} = \frac{j_e}{p_c} = \frac{eN_{2D}}{\tau_{scatt}} \frac{1}{p_c} = \frac{eN_{2D}}{\tau_{scatt}} \frac{\tau_c}{\tau_{trans}} = \frac{eN_{2D}}{\tau_{scatt}} \frac{\tau_c v}{L_p} \quad (1.2)$$

In this formula, j_e is the escape current. p_c is the capture probability. τ_{scatt} , τ_{trans} , τ_c are scattering time, transport time in one period, and capture time. L_p is the length of one period. v is the transport velocity. An accurate estimation of N_{2D} is important in achieving an accurate estimation of dark current in this model.

Good match of theoretical model and experimental results can be obtained by taking into consideration the electrons with energies larger than barrier height, and electrons slightly below barrier height because they also contribute through scattering-assisted tunneling [29].

It can be noted that the 3D Drift Model and the 2D Capture-Emission Model of the dark current are consistent when scattering time is independent of barrier width. This is satisfied when barrier width is large and thus capture time is proportional to barrier width.

1.4 Introduction of THz QWP-LED

Except for THz QWP, another extended version of QWP is proposed as a THz detecting and imaging device. It is called THz QWP-LED. As the name suggested, in QWP-LED, an LED is epitaxially grown on top of QWP. Therefore, when electrons generated from QWP part due to THz radiation transport into LED region, light is generated from LED by spontaneous emission. In the QWP-LED structure, LED region is still composed of GaAs and $\text{Al}_x\text{Ga}_{1-x}\text{As}$, as in conventional GaAs/ $\text{Al}_x\text{Ga}_{1-x}\text{As}$ LED, so the generated light is in near-infrared, with the free-space wavelength of approximately 870nm. Fig. 1-9 shows its band structure [30]. In this sense, the QWP-LED is a frequency up-conversion device, converting THz incident radiation into near-infrared emitted radiation. It will be extremely useful for THz FPA (Focal-Plane Array) imaging with the feature of pixelless imaging device [30].

Same as THz QWP, there are basically two ways to couple the THz incident light into the THz QWP-LED, i.e. 45° incidence (or other tilted angle) and grating coupler (GC), as shown in Fig. 1-10. Fig. 1-10a shows the THz QWP-LED with 45° incidence (or other tilted angle). THz incident light is coupled into the QWP part through the SI GaAs substrate, and NIR radiation is generated in the LED part. Fig. 1-10b shows the THz QWP-LED with 1D metal grating on top of the device to increase absorption. THz radiation is coupled into QWP part through the top metal grating and NIR light is generated in the LED part. In order to couple out the NIR

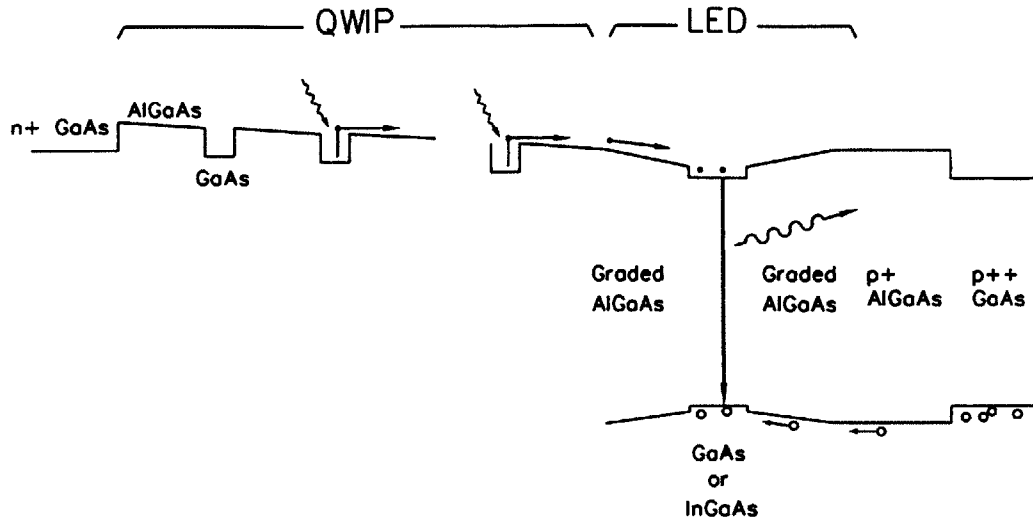


Figure 1-9: Energy band structure of QWP-LED [30].

radiation, NIR-transparent sapphire substrate is used, and benzocyclobutene (BCB) is used for bonding sapphire and GaAs device.

Because LED is generally a p-i-n diode, a p-type doping is required. However, due to the limitation of MBE growth with p-type GaAs layers, the THz QWP-LED was not implemented experimentally during the period that this thesis work is pursued. Therefore, this QWP-LED scheme is only designed and simulated, including the fabrication processes. Detailed design and calculation of THz QWP-LED's grating coupler and the accompanying plasma reflector will be discussed in Chapter 3, and its fabrication will be discussed in Chapter 4.

1.5 Thesis Overview

In this project, a sensitive THz QWP aimed at the peak detection of 4THz is desired. A low NEP is aimed for fast detection of THz radiation. Such a THz QWP is very promising for array integration and fast THz imaging. Moreover, THz QWP-LED will be explored in theory, design, simulation, and fabrication techniques.

In this thesis project, the theory, design, simulation and calculation, fabrication, and characterization of THz QWP and QWP-LED are pursued. Moreover, a special

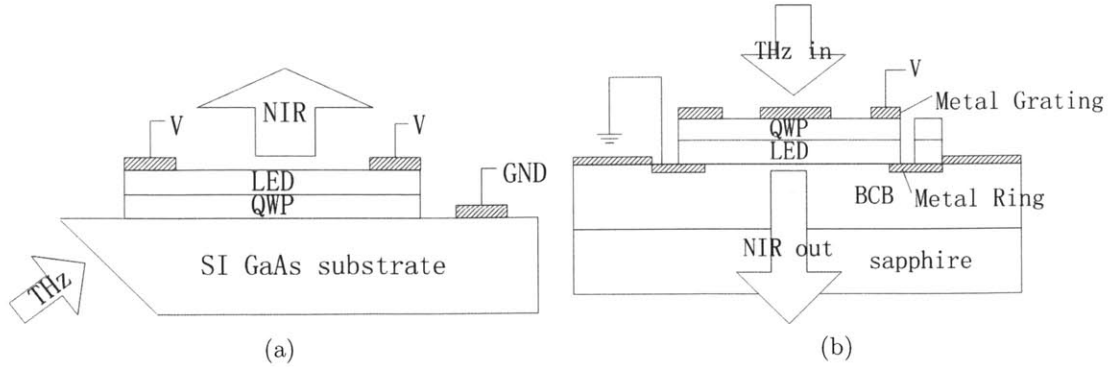


Figure 1-10: Schematics of THz QWP-LED. (a) THz QWP-LED with 45° incidence (or other tilted angle). (b) THz QWP-LED with 1D metal grating on top of the device to increase absorption. The metal grating and other metal electrodes are shown in shaded area in the figure.

device measurement system (cryogenic and low-noise) is built for the measurement and characterization of the device.

The facilities and equipments involved in this thesis project are listed as below. QWP simulation is taken using the computer clusters and relevant software in the Millimeter-Wave and THz Devices Group in MIT RLE (Research Lab of Electronics). QWP MBE growth is carried on by our collaborator Dr. John Reno in Sandia National Lab. QWP fabrication is taken in MIT MTL (Microsystem Technology Lab). Facilities include photolithography instruments, eBeam deposition, CVD, plasma etching, wet etching, etc. QWP measurement is taken in Prof. Qing Hu's lab. The facilities include cryogenic dewar, FTIR, HP DC supply and meters, computer and relevant software.

The rest of the thesis is organized as below. In Chapter 2, the theory of intersubband transition and carrier transport in QWP are discussed. This theory offers the guidelines for the design of THz QWP and THz QWP-LED. In Chapter 3, detailed calculation and simulation are presented. This includes the calculation of MQW structure using mode solver and $k \cdot p$ method, and the simulation of electromagnetic properties of the device grating coupler and plasma reflector using FEM method with the commercial software COMSOL Multiphysics. This calculation verifies the design of the QWP structure. In Chapter 4, the device fabrication techniques, processes,

and results are shown. The main fabrication processes include CVD (chemical-vapor deposition), metal deposition, dry-etch, photolithography, lift-off, etc. Besides, the special processing of THz QWP-LED is presented, which includes the testing and use of BCB and sapphire substrate as well as the bonding skills of sapphire and GaAs device using BCB. In Chapter 5, the device measurement is considered. This includes the cryogenic and low-noise measurement system build-up, and the actual device characterization using the home-made measurement system. Finally, Chapter 6 concludes the thesis.

Chapter 2

Theory of Intersubband Transitions and Carrier Transport in QWP

2.1 Theory of Intersubband Transition

Intersubband transition means the transition of electrons between the subbands formed from the MQW quantum wells.

In the case of QWP, due to the energy band difference of GaAs and $\text{Al}_x\text{Ga}_{1-x}\text{As}$, the $\text{Al}_x\text{Ga}_{1-x}\text{As}/\text{GaAs}/\text{Al}_x\text{Ga}_{1-x}\text{As}$ heterostructure forms a quantum well structure, in which GaAs layer is the potential well region and $\text{Al}_x\text{Ga}_{1-x}\text{As}$ layers are the potential barriers on both sides of the potential well. Due to quantum confinement, the original continuous energy bands in GaAs layer will be discretized into energy subbands, and their energy separations depend on the barrier height and well width. According the Fermi's Golden Rule, if there is perturbation, electrons in the system are subject to transitions from one state to another under the influence of the external perturbation. This is the basis for our theory of intersubband transition in the QWP MQW system.

Now consider the system of $\text{GaAs}/\text{Al}_x\text{Ga}_{1-x}\text{As}$ MQW structure with incoming

light. According to Fermi's Golden Rule, the transition rate of electron from the initial state $|i, n_{\vec{q}, \sigma}\rangle$ to the final state $|f, m_{\vec{q}, \sigma}\rangle$ is

$$W_{i \rightarrow f} = \frac{2\pi}{\hbar} |\langle f, m_{\vec{q}, \sigma} | H' | i, n_{\vec{q}, \sigma} \rangle|^2 \delta(E_f(\vec{k}_f) - E_i(\vec{k}_i) \pm \hbar\omega_{\vec{q}}) \quad (2.1)$$

in which

\vec{q} is the photon momentum,

σ is the photon polarization,

n, m are the number of photons in the initial and final states, respectively,

H' is the perturbation operator,

\vec{k}_f, \vec{k}_i are the electron momentum in the initial and final states, respectively,

$E_f(\vec{k}_f), E_i(\vec{k}_i)$ are the electron energies corresponding to the initial and final momenta, respectively,

$\omega_{\vec{q}}$ is the circular frequency of the photon with momentum \vec{q} .

According to quantum mechanics, the perturbation operator is expressed as

$$H' = -\frac{e}{2m^*} (\vec{A} \cdot \vec{p} + \vec{p} \cdot \vec{A}) \quad (2.2)$$

in which \vec{A} is the vector potential and expressed as

$$\vec{A} = \sqrt{\frac{\hbar}{2\epsilon\omega_{\vec{q}}V}} \hat{e}_{\vec{q}, \sigma} [\hat{a}_{\vec{q}, \sigma} e^{i\vec{q} \cdot \vec{r}} + \hat{a}_{\vec{q}, \sigma}^\dagger e^{-i\vec{q} \cdot \vec{r}}] \quad (2.3)$$

in Eqn. (2.3),

$\hat{e}_{\vec{q}, \sigma}$ is the unit vector of photon polarization direction, i.e. the direction of the electric field,

$\hat{a}_{\vec{q}, \sigma}, \hat{a}_{\vec{q}, \sigma}^\dagger$ are the annihilation and creation operators,

V is the volume of the material considered.

Therefore, combining Eqn. (2.2) and Eqn. (2.3), we have

$$\begin{aligned} \langle f, m_{\vec{q},\sigma} | H' | i, n_{\vec{q},\sigma} \rangle &= -\frac{e}{2m^*} \sqrt{\frac{\hbar}{2\epsilon\omega_{\vec{q}}V}} \\ &\{ \sqrt{n_{\vec{q},\sigma}} \delta_{m_{\vec{q},\sigma}, n_{\vec{q},\sigma}-1} \langle f | \hat{e}_{\vec{q},\sigma} e^{i\vec{q}\cdot\vec{r}} \cdot \vec{p} + \vec{p} \cdot \hat{e}_{\vec{q},\sigma} e^{i\vec{q}\cdot\vec{r}} | i \rangle \\ &+ \sqrt{n_{\vec{q},\sigma} + 1} \delta_{m_{\vec{q},\sigma}, n_{\vec{q},\sigma}+1} \langle f | \hat{e}_{\vec{q},\sigma} e^{-i\vec{q}\cdot\vec{r}} \cdot \vec{p} + \vec{p} \cdot \hat{e}_{\vec{q},\sigma} e^{-i\vec{q}\cdot\vec{r}} | i \rangle \} \end{aligned} \quad (2.4)$$

in Eqn. (2.4),

$$|i\rangle = \frac{1}{\sqrt{S_{xy}}} e^{i\vec{k}_{xy,i}\cdot\vec{r}_{xy}} \varphi_{z,i} \quad (2.5)$$

$$|f\rangle = \frac{1}{\sqrt{S_{xy}}} e^{i\vec{k}_{xy,f}\cdot\vec{r}_{xy}} \varphi_{z,f} \quad (2.6)$$

Therefore, we have

$$\begin{aligned} |H'_{i\rightarrow f}|^2 &= \langle f, m_{\vec{q},\sigma} | H' | i, n_{\vec{q},\sigma} \rangle^2 \\ &= \left(\frac{e}{2m^*}\right)^2 \frac{\hbar}{2\epsilon\omega_{\vec{q}}V} \\ &\{ n_{\vec{q},\sigma} \delta_{m_{\vec{q},\sigma}, n_{\vec{q},\sigma}-1} |\langle f | 2\vec{p} \cdot \hat{e}_{\vec{q},\sigma} e^{i\vec{q}\cdot\vec{r}} | i \rangle|^2 \\ &+ (n_{\vec{q},\sigma} + 1) \delta_{m_{\vec{q},\sigma}, n_{\vec{q},\sigma}+1} |\langle f | 2\vec{p} \cdot \hat{e}_{\vec{q},\sigma} e^{-i\vec{q}\cdot\vec{r}} | i \rangle|^2 \} \end{aligned} \quad (2.7)$$

in Eqn. (2.7),

$$\begin{aligned} \langle f | \vec{p} \cdot \hat{e}_{\vec{q},\sigma} e^{i\vec{q}\cdot\vec{r}} | i \rangle &= \frac{1}{S_{xy}} \langle e^{i\vec{k}_{xy,i}\cdot\vec{r}_{xy}} \varphi_{z,i} | (\vec{p}_{xy} + \vec{p}_z) \cdot \hat{e}_{\vec{q},\sigma} e^{i(\vec{q}_{xy} + \vec{q}_z)\cdot(\vec{r}_{xy} + \vec{r}_z)} | e^{i\vec{k}_{xy,f}\cdot\vec{r}_{xy}} \varphi_{z,f} \rangle \\ &= \frac{1}{S_{xy}} \langle e^{i\vec{k}_{xy,i}\cdot\vec{r}_{xy}} \varphi_{z,i} | \vec{p}_{xy} \cdot \hat{e}_{\vec{q},\sigma} e^{i(\vec{q}_{xy} + \vec{q}_z)\cdot(\vec{r}_{xy} + \vec{r}_z)} | e^{i\vec{k}_{xy,f}\cdot\vec{r}_{xy}} \varphi_{z,f} \rangle \\ &+ \frac{1}{S_{xy}} \langle e^{i\vec{k}_{xy,i}\cdot\vec{r}_{xy}} \varphi_{z,i} | \vec{p}_z \cdot \hat{e}_{\vec{q},\sigma} e^{i(\vec{q}_{xy} + \vec{q}_z)\cdot(\vec{r}_{xy} + \vec{r}_z)} | e^{i\vec{k}_{xy,f}\cdot\vec{r}_{xy}} \varphi_{z,f} \rangle \\ &= \frac{1}{S_{xy}} \langle e^{i\vec{k}_{xy,i}\cdot\vec{r}_{xy}} | \vec{p}_{xy} \cdot \hat{e}_{\vec{q},\sigma} e^{i\vec{q}_{xy}\cdot\vec{r}_{xy}} | e^{i\vec{k}_{xy,f}\cdot\vec{r}_{xy}} \rangle \langle \varphi_{z,i} | e^{i\vec{q}_z\cdot\vec{r}_z} | \varphi_{z,f} \rangle \\ &+ \frac{1}{S_{xy}} \langle e^{i\vec{k}_{xy,i}\cdot\vec{r}_{xy}} | e^{i\vec{q}_{xy}\cdot\vec{r}_{xy}} | e^{i\vec{k}_{xy,f}\cdot\vec{r}_{xy}} \rangle \langle \varphi_{z,i} | \vec{p}_z \cdot \hat{e}_{\vec{q},\sigma} e^{i\vec{q}_z\cdot\vec{r}_z} | \varphi_{z,f} \rangle \end{aligned} \quad (2.8)$$

In the last equal sign of Eqn. (2.8),

the first term vanishes to 0, because photons cannot excite direct transition between free carrier states,

and $e^{i\vec{q}\cdot\vec{r}} \approx e^{i0} = 1 (|r| \ll \lambda)$.

Therefore,

$$\langle f | \vec{p} \cdot \hat{e}_{\vec{q},\sigma} e^{i\vec{q}\cdot\vec{r}} | i \rangle = \delta_{\vec{k}_{xy,i}, \vec{q}_{xy} + \vec{k}_{xy,f}} (\hat{z} \cdot \hat{e}_{\vec{q},\sigma}) \langle \varphi_{z,i} | \vec{p}_z | \varphi_{z,f} \rangle \quad (2.9)$$

since $|\vec{q}_{xy}|$ is very small compared to $|\vec{k}_{xy}|$, so

$$\langle f | \vec{p} \cdot \hat{e}_{\vec{q},\sigma} e^{i\vec{q}\cdot\vec{r}} | i \rangle = \delta_{\vec{k}_{xy,i}, \vec{k}_{xy,f}} (\hat{z} \cdot \hat{e}_{\vec{q},\sigma}) \langle \varphi_{z,i} | \vec{p}_z | \varphi_{z,f} \rangle \quad (2.10)$$

Similarly,

$$\langle f | \vec{p} \cdot \hat{e}_{\vec{q},\sigma} e^{-i\vec{q}\cdot\vec{r}} | i \rangle = \delta_{\vec{k}_{xy,i}, \vec{k}_{xy,f}} (\hat{z} \cdot \hat{e}_{\vec{q},\sigma}) \langle \varphi_{z,i} | \vec{p}_z | \varphi_{z,f} \rangle \quad (2.11)$$

So

$$\begin{aligned} |H'_{i \rightarrow f}|^2 &= \left(\frac{e}{2m^*} \right)^2 \frac{\hbar}{2\epsilon\omega_{\vec{q}}V} \\ &\quad (2\delta_{\vec{k}_{xy,i}, \vec{k}_{xy,f}} (\hat{z} \cdot \hat{e}_{\vec{q},\sigma}) \langle \varphi_{z,i} | \vec{p}_z | \varphi_{z,f} \rangle)^2 \\ &\quad (n_{\vec{q},\sigma} \delta_{m_{\vec{q},\sigma}, n_{\vec{q},\sigma}-1} + (n_{\vec{q},\sigma} + 1) \delta_{m_{\vec{q},\sigma}, n_{\vec{q},\sigma}+1}) \end{aligned} \quad (2.12)$$

In Eqn. (2.12),

the first term $n_{\vec{q},\sigma} \delta_{m_{\vec{q},\sigma}, n_{\vec{q},\sigma}-1}$ refers to photon absorption,

the second term $(n_{\vec{q},\sigma} + 1) \delta_{m_{\vec{q},\sigma}, n_{\vec{q},\sigma}+1}$ refers to photon emission.

Only consider photon absorption, then

$$W_{i \rightarrow f} = \frac{2\pi}{\hbar} |H'_{i \rightarrow f}|^2 \delta(E_f(\vec{k}_f) - E_i(\vec{k}_i) - \hbar\omega_{\vec{q}}) \quad (2.13)$$

The total transition rate is

$$\begin{aligned}
W &= \sum_{i,f} W_{i \rightarrow f} f_i (1 - f_f) - \sum_{i,f} W_{i \rightarrow f} f_f (1 - f_i) \\
&= \sum_{i,f} W_{i \rightarrow f} (f_i - f_f) \\
&= \frac{2\pi}{\hbar} \sum_{i,f} |H'_{i \rightarrow f}|^2 (f_i - f_f) \delta(E_f(\vec{k}_f) - E_i(\vec{k}_i) - \hbar\omega_{\vec{q}}) \\
&= 2\pi \left(\frac{e}{2m^*}\right)^2 \frac{4}{2\epsilon\omega_{\vec{q}}V} \\
&\quad \sum_i (\hat{z} \cdot \hat{e}_{\vec{q},\sigma})^2 |\langle \varphi_{z,i} | \vec{p}_z | \varphi_{z,f} \rangle|^2 n_{\vec{q},\sigma} (f_i - f_f) \delta(E_f(\vec{k}_f) - E_i(\vec{k}_i) - \hbar\omega_{\vec{q}})
\end{aligned} \tag{2.14}$$

Since $f_f \approx 0$, $\sum_i f_i = n_e$ = number density of electrons, we have

$$W = \frac{e^2\pi}{m^{*2}\epsilon\omega_{\vec{q}}V} (\hat{z} \cdot \hat{e}_{\vec{q},\sigma})^2 |\langle \varphi_2 | \vec{p}_z | \varphi_1 \rangle|^2 n_e n_{\vec{q},\sigma} \delta(E_2 - E_1 - \hbar\omega_{\vec{q}}) \tag{2.15}$$

If we assume ϕ is flux of incoming light, which is the number of photons/(area \times time). We have

$$\begin{aligned}
\phi &= \frac{n_{\vec{q},\sigma}}{t \cdot A} = \frac{n_{\vec{q},\sigma} \cdot L}{t \cdot V} \\
&= \frac{n_{\vec{q},\sigma} \cdot c}{n_r \cdot V} = \frac{n_{\vec{q},\sigma}}{t \cdot S_{xy} \cos \theta}
\end{aligned} \tag{2.16}$$

Here θ is the incident angle, as shown in Fig. 2-1. S_{xy} is the in-plane area that THz radiation is incident on. Notice that S_{xy} and θ are not independent. It seems ϕ approaches infinity when θ approaches $\pi/2$, but S_{xy} is actually approaching infinity as well, so ϕ is not infinity when θ approaches $\pi/2$. We define absorption efficiency as the ratio of the number of electrons that transport per second and the number of photons coming into the QWP per second. The number of photons coming into the QWP per second is

$$\phi S_{xy} \cos \theta = \frac{n_{\vec{q},\sigma}}{t_{tot}} = \frac{n_{\vec{q},\sigma} c}{L_{tot} n_r} \tag{2.17}$$

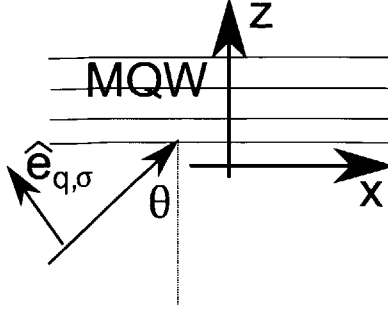


Figure 2-1: Illustration of the QWP MQW, incident THz radiation and polarization. The incident angle θ is shown.

So the absorption efficiency is

$$\begin{aligned}
 \eta &= \frac{W}{\phi S_{xy} \cos \theta} \\
 &= \frac{e^2 \pi}{m^* \epsilon \omega_{\bar{q}}} (\hat{z} \cdot \hat{e}_{\bar{q},\sigma})^2 |\langle \varphi_2 | \vec{p}_z | \varphi_1 \rangle|^2 \delta(E_2 - E_1 - \hbar \omega_{\bar{q}}) \cdot \frac{n_e n_r}{c S_{xy} \cos \theta}
 \end{aligned} \tag{2.18}$$

Notice that

$$\hat{z} \cdot \hat{e}_{\bar{q},\sigma} = \sin \theta \tag{2.19}$$

and the 2D electron density is

$$n_{2D} = \frac{n_e}{S_{xy}} \tag{2.20}$$

We define that the oscillator strength is

$$\begin{aligned}
 f &\equiv \frac{2}{m^* \hbar \omega} |\langle \varphi_2 | \vec{p}_z | \varphi_1 \rangle|^2 \\
 &= \frac{2m^* \omega}{\hbar} |\langle \varphi_2 | \vec{z} | \varphi_1 \rangle|^2
 \end{aligned} \tag{2.21}$$

Submitting Eqn. (2.21) (2.19) (2.20) into Eqn. (2.18),

$$\begin{aligned}
 \eta &= \frac{e^2 \pi}{m^* \epsilon \omega_{\bar{q}}} \frac{\sin^2 \theta}{\cos \theta} \frac{f m^* \hbar \omega}{2} \delta(E_2 - E_1 - \hbar \omega_{\bar{q}}) \cdot \frac{n_e n_r}{c S_{xy} \cos \theta} \\
 &= \frac{e^2 \pi \hbar}{2 \epsilon_0 n_r c m^*} \frac{\sin^2 \theta}{\cos \theta} f n_{2D} \delta(E_2 - E_1 - \hbar \omega_{\bar{q}})
 \end{aligned}$$

If we consider the broadening of the absorption, the δ -function is substituted by the Lorentzian lineshape function:

$$\delta(E_2 - E_1 - \hbar\omega_{\vec{q}}) \rightarrow l(\omega, E_{21}) = \frac{1}{\pi} \frac{\Delta E}{(\hbar\omega - E_{21})^2 + (\Delta E)^2} \quad (2.22)$$

Therefore we have

$$\eta \approx \frac{e^2 \pi \hbar}{2\epsilon_0 n_r c m^*} \frac{\sin^2 \theta}{\cos \theta} f n_{2D} \frac{1}{\pi} \frac{\Delta E}{(\hbar\omega - E_{21})^2 + (\Delta E)^2} \quad (2.23)$$

in which

ΔE is the half-width at half-maximum.

This is a pretty good approximation when $E_2 - E_1 - E_F \gg k_B T$ ($f_f \approx 0$).

Now we calculate the absorption coefficient $\alpha = \alpha(\omega)$, which is defined as

$$\frac{dI}{dx} = -\alpha I \quad (2.24)$$

in which I is the light intensity. Define ρ as the light energy density, and v as the velocity, we have

$$I = \rho v \quad (2.25)$$

and

$$\frac{dI}{dx} = \rho \frac{dv}{dx} = \frac{\rho}{t} \quad (2.26)$$

Therefore,

$$\begin{aligned}
\alpha(\omega) &= -\frac{\frac{dI}{dx}}{I} \\
&= \left(\frac{\hbar\omega[eV] \cdot W[sec^{-1}]}{V[m^3]} \right) / \left(\frac{n_{\vec{q},\sigma} \cdot \hbar\omega[eV]c[m/s]}{n_r V[m^3]} \right) \\
&= \frac{W n_r}{n_{\vec{q},\sigma} c} \\
&= \frac{e^2 \pi n_r}{m^* \epsilon_0 \omega_{\vec{q}} V c} (\hat{z} \cdot \hat{e}_{\vec{q},\sigma})^2 |\langle \varphi_2 | \vec{p}_z | \varphi_1 \rangle|^2 n_e \delta(E_2 - E_1 - \hbar\omega_{\vec{q}}) \\
&= \frac{e^2 \pi n_r}{m^* \epsilon_0 n_r^2 \omega_{\vec{q}} V c} (\hat{z} \cdot \hat{e}_{\vec{q},\sigma})^2 f \frac{m^* \hbar\omega}{2} n_e \frac{1}{\pi} \frac{\Delta E}{(\hbar\omega - E_{21})^2 + (\Delta E)^2} \\
&= \frac{e^2 \pi}{m^* \epsilon_0 n_r \omega_{\vec{q}} c} (\hat{z} \cdot \hat{e}_{\vec{q},\sigma})^2 f \frac{\hbar}{2} \frac{n_{2D}}{W_{well}} \frac{1}{\pi} \frac{\Delta E}{(\hbar\omega - E_{21})^2 + (\Delta E)^2} \\
&= \alpha_{coef}(E_{21}) \frac{1}{\pi} \frac{\Delta E}{(\hbar\omega - E_{21})^2 + (\Delta E)^2} \\
&= \alpha_{coef}(E_{21}) l(\omega, E_{21})
\end{aligned} \tag{2.27}$$

where

$$\alpha_{coef}(E_{21}) = \frac{e^2 \pi}{m^* \epsilon_0 n_r \omega_{\vec{q}} c} (\hat{z} \cdot \hat{e}_{\vec{q},\sigma})^2 f \frac{\hbar}{2} \frac{n_{2D}}{W_{well}} \tag{2.28}$$

If there are multiple energy levels contributing to photon absorptions in the QWP, then instead of Eqn. (2.27), we have

$$\alpha(\omega) = \sum_{E_{21}} \alpha_{coef}(E_{21}) l(\omega, E_{21}) \tag{2.29}$$

If incident light is along \hat{x} -direction, which is perpendicular to the QWP growth direction \hat{z} , then $\hat{z} \cdot \hat{e}_{\vec{q},\sigma} = 1$, so we have

$$\alpha_{tot} = \sum_{E_{21}} \alpha(\omega) \tag{2.30}$$

For some typical values of those physical parameters, we can assume the 3D doping, which maintains constant volume carrier density n_{3D} . Assume $n_{3D} = \frac{n_g}{V} = 10^{18} cm^{-3}$. We also have

$$\alpha L_{tot} = \eta \tag{2.31}$$

If we choose the value $L_{tot} = \text{Well Width} \sim 200\text{\AA}$, then $\alpha \sim 10^4\text{cm}^{-1}$, and $\eta \sim 10^4 \times 200 \times 10^{-8} = 2\%$. The linewidth depends on the interface quality. Typically, linewidth is on the order of meV.

2.2 Theory of Carrier Transport in QWP

The carrier transport in QWP consists of two parts: dark current and photo current. For the analysis of carrier transport in QWP, we use the following QWP model: an MQW structure made of GaAs/Al_xGa_{1-x}As. Usually many wells are required in order to achieve high enough light absorption. The choice of the number of wells doesn't have an explicit guideline. Generally, the least number of wells is preferred on the condition that enough light absorption is achieved. The structure is shown in Fig. 2-2 [23]. The figure shows the typical conduction band structure of the QWP. The quantum well regions are composed of GaAs and the quantum barrier regions are composed of Al_xGa_{1-x}As. The quantum well regions have carrier doping, which is n-type doping (Si) for our case. The figure shows the QWP under bias. The vertical arrows in the figure indicate the excitation of electrons from the ground state in the quantum well into the conduction band in the barrier, due to the incoming Terahertz photon.

GaAs serves as the quantum well regions due to its smaller conduction band energy, and Al_xGa_{1-x}As serves as the quantum barrier regions, because of its larger conduction band energy compared to that of GaAs. The exact conduction band energy value of Al_xGa_{1-x}As depends on the Aluminum fraction x : the larger the x , the larger the conduction band energy of Al_xGa_{1-x}As, thus the larger the conduction band offset (CBO) between the barrier and well regions. Part of the GaAs regions are n-doped in order to provide enough carriers to respond to the incoming terahertz radiation and generate photocurrent. Two n-type contacts are made at both terminals of the QWP device, thus let the carriers to flow under bias.

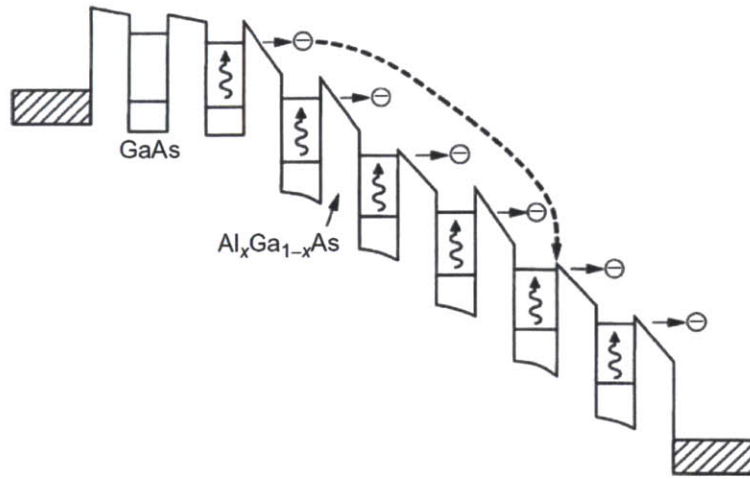


Figure 2-2: GaAs/ $\text{Al}_x\text{Ga}_{1-x}\text{As}$ MQW in a QWP. Upon THz radiation, electrons in the GaAs ground states are excited to the excited subbands in the quantum wells (GaAs regions) which then transport to the contact under voltage bias, forming the photoconductive current [23].

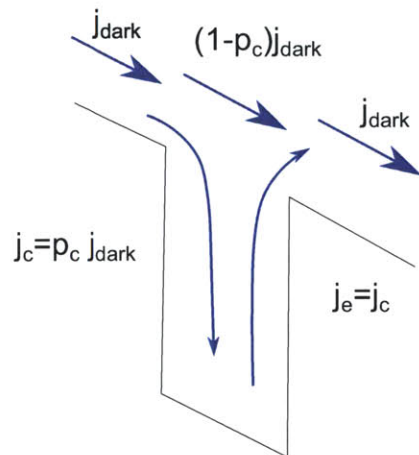


Figure 2-3: The figure shows the dark current model. Blue arrows show the flow of the current. In the figure, j_{dark} is the dark current density, p_c as the trapping or capture probability, j_c is the trapping or capture current, and j_e is the escape current. In balanced state, $j_c = j_e$.

2.2.1 Dark Current

Dark current affects the performance of a QWP, such as sensitivity, noise, etc. Therefore, a good understanding of the dark current mechanism in a QWP is important. Generally, the dark current can be modeled in the following scheme: in dark condition, under bias, carriers (electrons in our case) flow in the conduction band of the barrier regions. When electrons transport to the quantum well regions, part of them are trapped into the quantum well, leading to a loss of the current. The rest of the electrons keep flowing through the quantum well regions and reach the next quantum barrier regions. Meanwhile, some of the electrons trapped inside the quantum wells are excited into the conduction band of the barrier regions, leading to an increase of the current. These electrons, together with the electrons that are not trapped into the quantum wells, form the dark current that flows in the conduction band of the quantum barrier regions in the next module. Due to the principle of current continuity, when the current loss caused by trapping and the current increase caused by excitation reach the balance, the QWP is in balanced state and a constant dark current is formed. We define p_c as the trapping or capture probability, the ratio of the current formed by the electrons trapped into the quantum well and the electrons flowing in the QWP. p_e is defined as the escape probability, the ratio of the current formed by the electrons escaped from the quantum well and the electrons flowing in the QWP. This dark current mechanism is depicted in Fig. 2-3. In the figure, j_{dark} is the dark current density, p_c as the trapping or capture probability, j_c is the trapping or capture current, and j_e is the escape current. In balanced state, $j_c = j_e$.

There are two models to calculate the dark current j_{dark} : 3D Carrier Drift Model, and 2D Emission-Capture Model. They are discussed as below.

3D Drift Model

In the 3D Carrier Drift Model, j_{dark} is modeled as a current density j_{3D} in the quantum bulk regions, and is given

$$j_{dark} = eN_{3D}v(F) \quad (2.32)$$

in which

N_{3D} is the 3D density of electrons in the quantum barrier region,

F is the electric field,

$v(F)$ is the drift velocity as a function of electric field.

In Eqn. (2.32), N_{3D} is calculated by treating the quantum barrier region as a bulk semiconductor. The detailed calculation of N_{3D} is shown below.

We know that the Fermi-Dirac distribution is

$$f_{FD}(E) = \frac{1}{1 + e^{\frac{E-E_F}{k_B T}}} \quad (2.33)$$

in which

E is the energy of the electrons,

E_F is the Fermi energy.

In 3D case, we can calculate the Density of States (DoS) as below:

$$g(E)dE = \frac{2}{(2\pi)^3} d^3 \vec{k} = \frac{2}{(2\pi)^3} 4\pi k^2 dk \quad (2.34)$$

in which

$g(E)$ is the Density of State of electrons in energy E ,

\vec{k} is the momentum vector.

If we choose the zero-energy level as the first electron subband energy in the quantum well, we have

$$E - (V_b - E_1) = \frac{\hbar^2 k^2}{2m} \quad (2.35)$$

In which V_b is the barrier height of the quantum well, and E_1 is the energy separation between the ground state energy in the quantum well and the bottom of quantum well. Fig. 2-4 shows the band structure of one quantum well in QWP. The electron subbands in the quantum well and in the conduction band continuum are shown. The corresponding wavefunctions are shown as well. The zero-energy level is defined as the first electron subband energy in the quantum well, which is of energy E_1 above the bottom of quantum well. V_b is the barrier height of the quantum well.

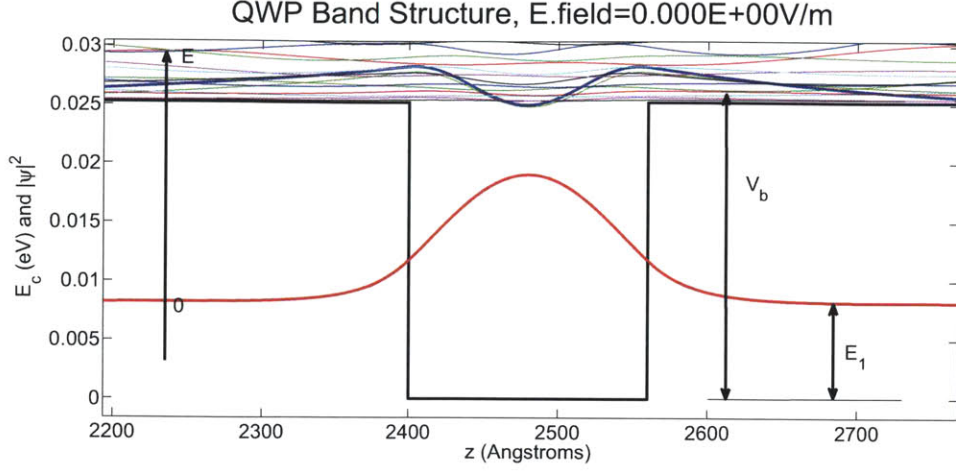


Figure 2-4: The band structure of one quantum well in QWP. The electron subbands and the corresponding wavefunctions in the quantum well and in the conduction band continuum are shown. The zero-energy level is defined as the first electron subband energy in the quantum well, which is of energy E_1 above the bottom of quantum well. V_b is the barrier height of the quantum well.

Therefore, the conduction band minimum is of energy $V_b - E_1$. Eqn. (2.35) is the E-k relation for the 3D bulk material (barrier material), so it obeys the square law.

From Eqn. (2.35), we have

$$k = \frac{\sqrt{2mE}}{\hbar} \quad (2.36)$$

Thus

$$\frac{dk}{dE} = \frac{\sqrt{2m}}{\hbar} \frac{1}{2\sqrt{E}} = \frac{1}{\hbar} \sqrt{\frac{m}{2E}} \quad (2.37)$$

Substitute Eqn. (2.37) into Eqn. (2.34), we have

$$\begin{aligned} g(E) &= \frac{2mE}{\pi^2 \hbar^2} \frac{dk}{dE} \\ &= \frac{\sqrt{2(E - (V_b - E_1))}}{\pi^2 \hbar^3} m^{3/2} \end{aligned} \quad (2.38)$$

Therefore, the 3D electron density in the conduction band (bulk barrier material)

is

$$\begin{aligned}
n_{3D}(E) &= \int_{E=V_b-E_1}^{\infty} g(E) f_{FD}(E) dE \\
&= \frac{m^{3/2}}{\pi^2 \hbar^3} \int_{E=V_b-E_1}^{\infty} \sqrt{2(E - (V_b - E_1))} \frac{1}{1 + e^{\frac{E-E_F}{k_B T}}} dE \\
&\approx \frac{m^{3/2}}{\pi^2 \hbar^3} \int_{E=V_b-E_1}^{\infty} \sqrt{2(E - (V_b - E_1))} \exp\left(-\frac{E - E_F}{k_B T}\right) dE \\
&= \frac{\sqrt{2} m^{3/2}}{\pi^2 \hbar^3} \int_{E=V_b-E_1}^{\infty} \sqrt{(E - (V_b - E_1))} \\
&\quad \exp\left(-\frac{E - (V_b - E_1)}{k_B T} - \frac{(V_b - E_1) - E_F}{k_B T}\right) dE \\
&= \frac{\sqrt{2} m^{3/2} (k_B T)^{3/2}}{\pi^2 \hbar^3} \exp\left(-\frac{(V_b - E_1) - E_F}{k_B T}\right) \frac{\sqrt{\pi}}{2} \\
&= 2 \left(\frac{m k_B T}{2\pi \hbar^2}\right)^{3/2} \exp\left(-\frac{(V_b - E_1) - E_F}{k_B T}\right) \tag{2.39}
\end{aligned}$$

In Eqn. (2.39), we used the Boltzmann Approximation in the evaluation of the 3D electron density.

In Eqn. (2.32), $v(F)$ is calculated by

$$v(F) = \frac{\mu F}{\sqrt{1 + \left(\frac{\mu F}{v_{sat}}\right)^2}} \tag{2.40}$$

In which

μ is the mobility of electrons,

v_{sat} is the saturation velocity of electrons in the bulk material.

2D Emission-Capture Model

Unlike the 3D Drift model of dark current, in the 2D Emission-Capture Model, dark current density j_{dark} is calculated by

$$j_{dark} = \frac{j_e}{p_c} \tag{2.41}$$

As mentioned before, in Eqn. (2.41),

j_e is the current density that contributed by the electrons escaping from the quantum wells,

p_c is the trapping or capture probability.

These trapping and escaping processes are depicted in Fig. 2-3.

We first consider how to calculate j_e , the escape current.

Scattering-assisted process is the dominant factor that contributes to the escape current [31]. In the scattering-assisted process, electrons in the quantum well will undergo a scattering process, and then transfer from the confined 2D state to the unconfined 3D state in the barrier material. In this scattering process, the energy is conserved. Therefore, the scattering process can only happen to those electrons in the quantum well which has the confined state energy that is higher or equivalent to the barrier energy height. If the QWP structure is designed for the first excited state minimum in the quantum wells to be aligned with the conduction band minimum in the barrier material, only those electrons in the quantum well ground state can go through the scattering process on the condition that their energy is at least the conduction band minimum of the barrier material. Fig. 2-5 shows this scattering process in k-space. Therefore, we have the following equation to calculate j_e ,

$$j_e = \frac{eN_{2D}}{\tau_{scatt}} \quad (2.42)$$

In which

N_{2D} is the 2D electron density in the quantum wells that contributes to the scattering event. These electrons only include those in the quantum well ground state with the energy higher than the barrier energy height.

τ_{scatt} is the scattering time constant for the electrons in the quantum wells mentioned above to transfer from the 2D confined state to the 3D continuum state (unconfined state).

In the 2D electron system, density of state is given by

$$g_{2D}(E_{||})dE_{||} = 2\frac{1}{(2\pi)^2}2\pi k_{||}dk_{||} = \frac{1}{\pi}k_{||}dk_{||} \quad (2.43)$$

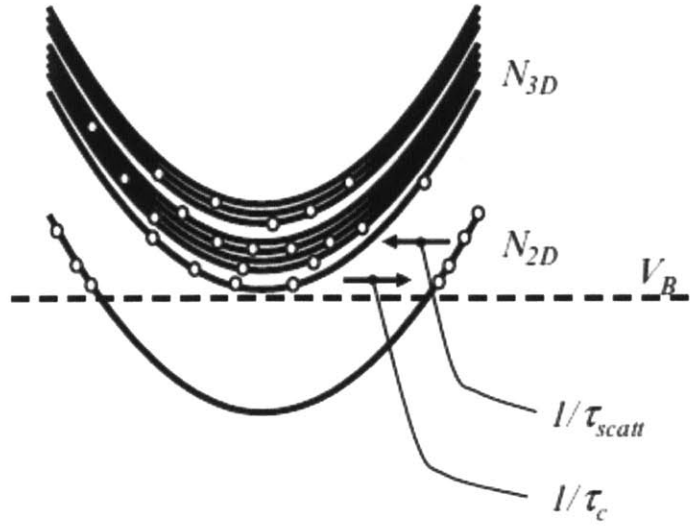


Figure 2-5: The scattering-assisted process in k-space. The lower singular parabola shows the ground state E-k curve in the quantum well. The higher parabolas show the E-k curves in the barrier material, which are unconfined 3D states. The scattering process time constant is τ_{scatt} . The reverse process is the capture or trapping process and the time constant is τ_c . This figure is from [28].

In Eqn. (2.43),

k_{\parallel} is the in-plane momentum of the 2D system

E_{\parallel} is the in-plane energy of the 2D system.

So we have

$$E_{\parallel} = \frac{\hbar^2 k_{\parallel}^2}{2m} \quad (2.44)$$

and the total energy is

$$E = E_z + E_{\parallel} \quad (2.45)$$

In which

E_z is the out-of-plane energy of the 2D system,

E is the total energy.

Therefore,

$$\begin{aligned}
g_{2D}(E) &= \frac{1}{\pi} k \frac{dk}{dE} = \frac{1}{\pi} \sqrt{\frac{2mE}{\hbar^2}} \frac{1}{\hbar} \sqrt{\frac{m}{2E}} \\
&= \frac{m}{\pi \hbar^2}
\end{aligned} \tag{2.46}$$

So the 2D electron density N_{2D} defined in (2.41) (the part that contributes to scattering-assisted process) is

$$\begin{aligned}
n_{2D}(E) &= \int_{E=V_b-E_1}^{\infty} g(E) f_{FD}(E) dE \\
&= \frac{m}{\pi \hbar^2} \int_{E=V_b-E_1}^{\infty} \frac{1}{1 + e^{\frac{E-E_F}{k_B T}}} dE \\
&\approx \frac{m}{\pi \hbar^2} \int_{E=V_b-E_1}^{\infty} e^{-\frac{E-E_F}{k_B T}} dE \\
&= \frac{m}{\pi \hbar^2} k_B T e^{-\frac{V_b-E_1-E_F}{k_B T}}
\end{aligned} \tag{2.47}$$

We can calculate the Fermi-energy E_F by considering that in the quantum well, the total electron density is the doping density. On the condition that the temperature is very low, the Fermi-Dirac distribution is 1 when energy is below Fermi-energy, and 0 when energy is above Fermi-energy. Thus, we have

$$\begin{aligned}
N_D &= \int_{E=0}^{\infty} g(E) f_{FD}(E) dE \\
&= \int_{E=0}^{E_F} g(E) 1 dE \\
&= \frac{m}{\pi \hbar^2} E_F
\end{aligned} \tag{2.48}$$

In which

N_D is the doping density in the quantum well.

Therefore, from Eqn. (2.48),

$$E_F = N_D \frac{\pi \hbar^2}{m} \quad (2.49)$$

In Eqn. (2.41), the capture probability p_c is calculated as

$$p_c = \frac{\tau_{trans}}{\tau_{trans} + \tau_c} \quad (2.50)$$

In which

τ_{trans} is the transition time for an electron to transport from one quantum well to the next one. This time includes the transition time in one barrier.

τ_c is capture time, which has been explained already.

The transition time τ_{trans} thus can be calculated as

$$\tau_{trans} = \frac{L_p}{v} = \frac{L_w + L_b}{v} \quad (2.51)$$

In which

L_p is the length of one period of the QWP structure, including one barrier width L_b and one quantum well width L_w .

v is the transition velocity of the electrons.

In the actual QWP devices, the capture probability is much smaller than 1,

$$p_c \ll 1 \quad (2.52)$$

From Eqn. (2.50), this is to say

$$\tau_c \gg \tau_{trans} \quad (2.53)$$

Therefore, Eqn. (2.50) can be approximated as

$$p_c \approx \frac{\tau_{trans}}{\tau_c} \quad (2.54)$$

Now combining Eqn. (2.41), (2.47), (2.54), we have the dark current in the 2D

Emission-Capture Model to be written as

$$\begin{aligned}
 j_{dark} &= \frac{j_e}{p_c} = \frac{eN_{2D}}{\tau_{scatt}} \frac{\tau_c}{\tau_{trans}} \\
 &= \frac{eN_{2D}v}{L_p} \frac{\tau_c}{\tau_{scatt}} \tag{2.55}
 \end{aligned}$$

$$= \frac{ev}{L_p} \frac{\tau_c}{\tau_{scatt}} \frac{m}{\pi\hbar^2} k_B T e^{-\frac{V_b - E_1 - E_F}{k_B T}} \tag{2.56}$$

The 3D Drift Model and the 2D Capture-Emission Model of the dark current are consistent when scattering time is independent of barrier width. This is satisfied when barrier width is large and thus capture time is proportional to barrier width.

2.2.2 Photocurrent

As discussed in Chapter 2.1, the absorption of THz radiation in the QWP leads to current flow in the conduction band of the barrier material under external voltage bias, forming photocurrent. In this section, a detailed analysis of photocurrent in QWP is conducted.

Fig. 2-6 describes the mechanism of the carrier transport across a quantum well under illumination. The blue lines, arrows and words represent the dark current, and the red ones represent the photocurrent. From the figure, we can see the photocurrent trapping and emission is similar as those of the dark current. The latter is depicted in Fig. 2-3.

The rate equation for the excited electrons in the quantum well can be written as

$$\frac{dn_{ex}}{dt} = \Phi\eta^{(1)} - \frac{n_{ex}}{\tau_{esc}} - \frac{n_{ex}}{\tau_{relax}} \tag{2.57}$$

In Eqn. (2.57),

n_{ex} is the number of excited electrons under THz illumination,

Φ is the incident photon number per unit time,

τ_{esc} is the escape time, i.e. the time for one electron to escape from the quantum well to the conduction band of the barrier material under illumination,

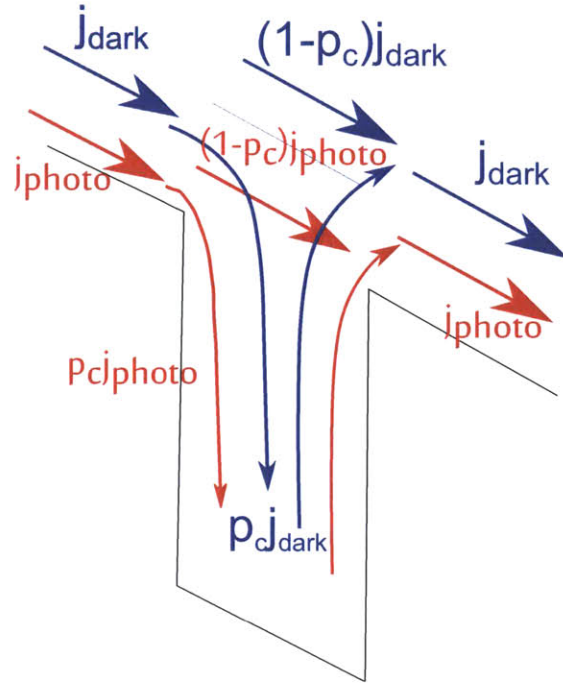


Figure 2-6: The mechanism of the carrier transport across a quantum well under illumination. The blue lines, arrows and words represent the dark current, and the red ones represent the photocurrent. The trapping or capture probability, p_c , is the same for both dark current and photocurrent.

τ_{relax} is the intersubband relax time,

$\eta^{(1)}$ is the absorption quantum efficiency in one quantum well, i.e. the ratio of number of photons absorbed in one quantum well and the total number of incident photons. The superscript (1) means one quantum well. Let η be the absorption quantum efficiency in the whole QWP, and assume the absorption efficiencies in all the quantum wells are the same, so we have $N\eta^{(1)} = \eta$, and N is the total number of quantum wells.

In the steady state,

$$\frac{dn_{ex}}{dt} = 0 \quad (2.58)$$

Therefore, we can solve for n_{ex} from Eqn. (2.57). This gives

$$n_{ex} = \frac{\tau_{esc}\tau_{relax}}{\tau_{esc} + \tau_{relax}} \Phi \eta^{(1)} \quad (2.59)$$

The photoemission current from one well, i.e. the current formed by electrons directly emitted from the ground state of one quantum well to the conduction band of the barrier material, is given by

$$i_{photo}^{(1)} = \frac{en_{ex}}{\tau_{esc}} \quad (2.60)$$

Again, here $i_{photo}^{(1)}$ means the photoemission current from one quantum well, and the superscript (1) means one quantum well.

Combining Eqn. (2.60) and Eqn. (2.59), we have the photoemission current from one well as

$$\begin{aligned} i_{photo}^{(1)} &= \frac{e}{\tau_{esc}} \frac{\tau_{esc}\tau_{relax}}{\tau_{esc} + \tau_{relax}} \Phi\eta^{(1)} = e\Phi\eta^{(1)} \frac{\tau_{relax}}{\tau_{esc} + \tau_{relax}} \\ &= \frac{e\Phi\eta}{N} \frac{\tau_{relax}}{\tau_{esc} + \tau_{relax}} \end{aligned} \quad (2.61)$$

$$= e\Phi\eta \frac{p_e}{N} \quad (2.62)$$

In the above Equation, p_e is the escape probability for an excited electron to escape from the quantum well. It is defined as

$$p_e \equiv \frac{\tau_{relax}}{\tau_{esc} + \tau_{relax}} \quad (2.63)$$

This has been used in Eqn. (2.62).

The escape probability, defined in Eqn. (2.63), can be understood as the ratio of two electron transit rates: the escape rate (which is proportional to $1/\tau_{esc}$), and the sum of the escape rate and the other non-emission rates (which is proportional to $1/\tau_{relax}$). Here, all other non-emission rates are interpreted as relax rate, meaning the rate of electron transitions which do not contribute to the photoemission current. This includes a lot of processes, such as electron-phonon scattering, etc. Typically, τ_{relax} is longer than 100ps in a GaAs THz QWP due to acoustic phonon scattering [32, 33], while other time constants are usually on the order of ps [28].

The photoemission current $i_{photo}^{(1)}$ in Eqn. (2.61), represents the "vertical" line in

Fig. 2-6. In the actual device, what can be measured is the photocurrent I_{photo} , or the photocurrent density j_{photo} shown as the "horizontal" line in Fig. 2-6. From this figure, we can relate I_{photo} and $i_{photo}^{(1)}$ as

$$I_{photo} = \frac{i_{photo}^{(1)}}{p_c} \quad (2.64)$$

This is to say, the ratio of the photoemission current from one well and the photocurrent equals the capture probability. Therefore, given Eqn. (2.62), we have

$$I_{photo} = e\Phi\eta \frac{p_e}{Np_c} \equiv e\Phi\eta g_{photo} \quad (2.65)$$

Here, g_{photo} is called the photoconductive gain. From Eqn. (2.65), we can see the photoconductive gain is defined as

$$g_{photo} \equiv \frac{p_e}{Np_c} \quad (2.66)$$

Again, from Eqn. (2.65), we have

$$g_{photo} = \frac{I_{photo}}{e\Phi\eta} \quad (2.67)$$

This is to say, the photoconductive gain is the ratio of the photocurrent measured from the QWP device, and the electron flux that are absorbed in the whole QWP device. In other words, the photoconductive gain is the ratio of the number of electrons collected in the external circuit, over the number of photons absorbed in QWP. It is dimensionless.

Recall that in Chapter 2.2.1, Eqn. (2.50), the capture probability in Eqn. (2.66) is defined as

$$p_c = \frac{\tau_{trans}}{\tau_{trans} + \tau_c}$$

For a bound-to-continuum QWP structure, i.e. the first-excited state of the quantum well is aligned with the conduction band edge of the barrier material, the photoemission escape rate is very fast, because once an electron from the ground state

in the quantum well is photo-excited, it transits into the excited state and can become the electrons in the 3D barrier material and it is hard for it to relax back to the quantum well. Therefore, the escape time τ_{esc} (usually much smaller than 1ps in bound-to-continuum MQW under the bias of 1 *kV/cm*) is much smaller compared to the relax time τ_{relax} (on the order of 100ps), giving an escape probability almost 1,

$$p_e \approx 1 \quad (2.68)$$

For similar reason, the capture time, or trapping time is quite large, and the capture probability is much smaller than 1,

$$p_c \approx \frac{\tau_{trans}}{\tau_c} \ll 1$$

This has already been stated in Eqn. (2.52) and Eqn. (2.54). Therefore, the photoconductive gain can be approximated as

$$g_{photo} \approx \frac{1}{Np_c} \approx \frac{\tau_c}{N\tau_{trans}} = \frac{\tau_c v}{NL_p} \quad (2.69)$$

Another important parameter to evaluate the performance of QWP, or general photodetector, is the responsivity *Res*, defined as the ratio of the photocurrent and the incoming light power. In the case of QWP,

$$Res = \frac{I_{photo}}{\hbar\omega\Phi} = \frac{e\eta g_{photo}}{\hbar\omega} \quad (2.70)$$

In which ω is the frequency of the incoming light.

Notice that from Eqn. (2.66),

$$g_{photo} \equiv \frac{p_e}{Np_c} = \frac{\tau_{relax}}{\tau_{esc} + \tau_{relax}} \frac{\tau_{trans} + \tau_c}{\tau_{trans}} \frac{1}{N} \quad (2.71)$$

Therefore, $g_{photo} \propto 1/N$ and $\eta \propto N$, so the number of wells N does not contribute to the responsivity *Res*. However, the number of wells still matters in the design of QWP, because it changes the QWP noise. This will be discussed in detail in Chapter 2.3.1.

There are other ways to improve the responsivity of a QWP.

First, try to make the escape probability p_e large, approaching 1. This can be done by implementing a very fast escape rate for the electrons in the quantum well, much faster than the relax rate. As discussed above, this can be done by designing the QWP structure to be bound-to-continuum structure.

Second, try to make the capture probability p_c small. Again, as discussed before, a bound-to-continuum structure can help. However, notice that the transition time τ_{trans} is also dependent on the bias voltage because the transition velocity is a function of the bias electric field. A large electric field gives a small τ_{trans} , and meanwhile decreases the capture rate (increases τ_c). However, if the electric field is too large, the energy separation between the ground state and first excited state is shifted, resulting in light absorption error. So an appropriate bias voltage has to be selected in order to achieve optimal responsivity.

Moreover, a large absorption efficiency η is preferred to increase responsivity. Recall that intersubband transition requires the polarization of the incoming light field not in the quantum well plane, a tilted incidence is the usual practice, typically 45° or Brewster angle incidence. In this case, the absorption is subject to the light reflection in the air-semiconductor interface. Therefore, usually a 45° or Brewster angle facet is made on the real QWP device, so that the incident light can be shone normal to the facet and forming an angle with the quantum well plane. The normal incidence can couple as much light as possible into the device. Another solution to improve intersubband light coupling is to use grating coupler to diffract the normal incident light into the QWP. In this case, a grating coupler structure needs to be designed carefully to achieve high absorption efficiency η . Detailed discussion of the grating coupler are shown in Chapter 3.

2.3 Performance Analysis of QWP

In the previous section, two QWP performance parameters, the responsivity and photoconductive gain have already been discussed. In this section, the noise of the

QWP will be analyzed and the detectivity as well as the specific detectivity will be introduced. All these parameters will be analyzed together to merit the performance of QWP.

2.3.1 QWP Noise

There are several types of noise in a QWP.

$1/f$ noise is basically a low-frequency noise and its spectral intensity is generally inverse proportional to the frequency, thus the name $1/f$ noise. The mechanism of this type of noise is still unclear yet. $1/f$ noise is usually very small in GaAs QWP and does not appear to be the limiting factor of the detector performance.

Johnson noise, also known as thermal noise, is caused by the heat in a resistive-like device. Its noise current is

$$i_{n,J}^2 = \frac{4k_B T \Delta f}{R} \quad (2.72)$$

In which

Δf is the measurement bandwidth of the detector,

R is device resistance.

Similar to $1/f$ noise, Johnson noise usually appears to be small in GaAs QWP [34]. Especially for THz QWP which needs to operate in cryogenic temperature in order to suppress thermal smearing of electron subbands, Johnson noise in THz QWP turns out to be unimportant in most of the cases.

The main components of noise of QWP are the dark current shot noise and photon noise, which are usually the limiting factors of the QWP. They will be discussed in detail in the rest of this section.

It is well known that in a photodetector, due to the discreteness of photons arriving at the photodetector and the assumed Poisson distribution, a shot noise is generated and is expressed as

$$i_{n,s}^2 = 2e\bar{I}_{photo}\Delta f \quad (2.73)$$

In which \bar{I}_{photo} is the time-averaged photocurrent.

The shot noise is the minimum noise level that a photodetector can achieve, because it assumes that one incoming photon gives rise to one electron to form the photocurrent, and the noise is only the statistical variance of the incoming photons.

However, a more complicated statistical process occurs in a photoconductor [35]. A finite lifetime of the photoexcited electrons, τ_p , exists, and is Poisson-distributed. If the signal integration time τ_{int} is much longer than τ_p , then the observed signal is a sequence of short pulses. Each short pulse obeys Poisson distribution in time, and the overall amplitudes of all the short pulses obey Poisson distribution as well. This process gives a generation-recombination noise, and its noise current is expressed as [35]

$$i_{n,gr}^2 = 4eg_{photo}\bar{I}_{photo}\Delta f \quad (2.74)$$

In which g_{photo} is the photoconductive gain described before in Eqn. (2.67). This noise is called generation-recombination noise, because we can interpret Eqn. (2.74) by the statement that the noise is caused by generation and recombination processes, both of which obey Poisson distribution and can be described in the form of Eqn. (2.73). Notice the addition of g_{photo} in Eqn. (2.74) compared to Eqn. (2.73) is because, in the simple model, the assumption is made that once an electron is excited, it will be collected in the external circuit. While considering the more complicated photon lifetime and generation-recombination process, a photoexcited electron has the probability to be recombined before it reaches the terminals of the photoconductor, giving rise to a photoconductive factor. The generation-recombination noise expressed in Eqn. (2.74) is called photon noise.

The dark current noise is similar to photon noise, except for the fact that the contributing current is not the photocurrent \bar{I}_{photo} , but the dark current I_{dark} , and the corresponding photoconductive gain changes to noise gain. Therefore, we can write the dark current noise current as [35]

$$i_{n,dark}^2 = 4eg_{noise}I_{dark}\Delta f \quad (2.75)$$

And the noise gain is

$$g_{noise} = \frac{1}{Np_c} \quad (2.76)$$

This is different from photoconductive gain. But in the limit that $p_e \approx 1$, noise gain is almost the same as photoconductive gain, i.e., $g_{noise} \approx g_{photo}$.

2.3.2 QWP Detectivity and Noise Equivalent Power

Generally, for a photodetector, the Noise Equivalent Power (*NEP*) is defined as the power of the noise when the Signal-to-Noise Ratio (*SNR*) equals 1. It is usually characterized with one second integration time. Because of this, $NEP/\sqrt{\Delta f}$ is the usual parameter to describe the noise characteristic of a detector, and has the unit of W/\sqrt{Hz} , or A/\sqrt{Hz} , V/\sqrt{Hz} depends on whether noise power, noise current or noise voltage is being discussed. From the definition above, we have

$$i_n^2 = Res^2 P_s^2 \quad (2.77)$$

In which

i_n is the noise current,

Res is the responsivity,

P_s is the signal power.

This is just the definition of responsivity. Therefore, the *NEP* can be calculated as

$$NEP = \frac{i_n}{Res} \quad (2.78)$$

In the cases of Johnson noise, shot noise, dark-current noise and photon noise, the normalized noise current are

$$\frac{i_{n,J}}{\sqrt{\Delta f}} = \sqrt{\frac{4k_B T}{R}} \quad (2.79)$$

$$\frac{i_{n,s}}{\sqrt{\Delta f}} = \sqrt{2e\bar{I}} \quad (2.80)$$

$$\frac{i_{n,dark}}{\sqrt{\Delta f}} = \sqrt{4eg_{noise}\bar{I}_{noise}} \quad (2.81)$$

$$\frac{i_{n,photo}}{\sqrt{\Delta f}} = \sqrt{4eg_{photo}\bar{I}_{photo}} \quad (2.82)$$

The detectivity D of a detector is defined as the inverse of NEP ,

$$D = \frac{1}{NEP} \quad (2.83)$$

Detectivity characterizes the detection performance of a photodetector. Specific detectivity, D^* , is the detectivity normalized with the square root of detector area and bandwidth. It characterizes the performance of a detector regardless of both spatial and temporal averaging effects. The definition of the specific detectivity is

$$D^* = D\sqrt{A\Delta f} = \frac{\sqrt{A\Delta f}}{NEP} = \frac{Res\sqrt{A\Delta f}}{i_n} \quad (2.84)$$

In which A is the area of the detector.

The lower the D^* , the larger the measurement bandwidth can be, thus the faster speed the detector can achieve, or the higher the resolution of a detector array given the fixed measurement time. Moreover, since the D^* scales with the square root of bandwidth, if the D^* is increased 10 times, the bandwidth can be increased 100 times, which means the integration of the detector can be 100 times faster. Due to the usual weak signal power of THz radiation and the long integration time of conventional THz detector, increasing the detectivity, or lower the NEP , is important in achieving high-performance THz QWP.

Now, we can consider the specific detectivity when the performance of the QWP is

limited by dark current noise and assuming a 3D dark current drift model. Combining Eqn. (2.69) (2.70) (2.81) (2.32), we have the specific detectivity in this case as

$$\begin{aligned}
D^* &= \frac{Res\sqrt{A\Delta f}}{i_n} \\
&= \frac{e\eta g_{noise}}{\hbar\omega} \frac{\sqrt{A}}{\sqrt{4e g_{noise} I_{dark,3D}}} \\
&= \frac{e\eta\sqrt{g_{noise}}}{\hbar\omega} \frac{1}{\sqrt{4e^2 N_{3D}v}} \\
&= \frac{\eta\sqrt{\tau_c}}{2\hbar\omega\sqrt{N}L_p} \frac{1}{\sqrt{N_{3D}}} \tag{2.85}
\end{aligned}$$

If we consider another 2D Emission-Capture model for dark current and the QWP is still dark-current noise limited, similarly, we have the specific detectivity as

$$\begin{aligned}
D^* &= \frac{Res\sqrt{A\Delta f}}{i_n} \\
&= \frac{e\eta g_{noise}}{\hbar\omega} \frac{\sqrt{A}}{\sqrt{4e g_{noise} I_{dark,2D}}} \\
&= \frac{e\eta\sqrt{g_{noise}}}{\hbar\omega} \frac{\sqrt{L_p\tau_{scatt}}}{\sqrt{4e^2 N_{2D}\tau_c v}} \\
&= \frac{\eta}{2\hbar\omega\sqrt{N}} \frac{\sqrt{\tau_{scatt}}}{\sqrt{N_{2D}}} \tag{2.86}
\end{aligned}$$

From the above Equations, Eqn. (2.85) (2.86), we can see the difference of the two models more clearly: the 3D drift model emphasizes on the 3D carrier density and the capture process in the carrier transport, while the 2D Emission-Capture model emphasizes on the equivalent 2D carrier density and the scattering process during carrier transport. Despite this, the numerical values derived from both models in specific THz QWP designs are approximately the same.

From Eqn. (2.85) (2.86), we can see the device parameters that influences the QWP detectivity, or the ways to improve detectivity: to increase absorption efficiency η , to increase the capture time τ_c (or to decrease the capture rate, or to decrease the

capture probability).

In terms of the effect of quantum well doping density N_D to specific detectivity, notice that η is proportional to doping density thus the fermi energy E_F (Eqn. (2.48)). Also, from Eqn. (2.20) and Eqn. (2.39), the carrier density is proportional to $e^{\frac{E_F}{k_B T}}$. Therefore,

$$D^* \propto E_F e^{-\frac{E_F}{2k_B T}} \quad (2.87)$$

Thus, in order to achieve maximum D^* by varying doping density N_D , we can calculate this by equating the derivative of D^* with respect to E_F to 0,

$$\begin{aligned} 0 &= \frac{dD^*}{dE_F} = \frac{d}{dE_F} E_F e^{-\frac{E_F}{2k_B T}} \\ &= \left(1 - \frac{E_F}{2k_B T}\right) e^{-\frac{E_F}{2k_B T}} \end{aligned} \quad (2.88)$$

This gives the solution

$$E_F = 2k_B T \quad (2.89)$$

This is the condition that the maximum D^* is achieved. The doping value satisfying this condition is usually quite small in cryogenic temperature. For higher temperature, the smearing of the energy subbands increases due to thermal perturbation, it can be imagined that larger doping is needed in order to achieve good detectivity. However, generally, the detectivity decreases with higher temperature.

An additional note to Eqn. (2.87) is that the specific detectivity does not necessarily decreases as temperature drops, because the capture time and scattering time appeared in Eqn. (2.85) and Eqn. (2.86) increase as temperature drops.

Another factor that may influence D^* is the number of wells N . According to Eqn. (2.85) and Eqn. (2.86), it seems as N decreases, D^* increases. In fact, N also influence the absorption efficiency η : too few wells cannot maintain a considerable value of η . However, ideally, if the absorption efficiency η can be made very high

within one quantum well, close to 100%, the least number of quantum wells N should be used. The limit of this case is one well ($N = 1$) with an absorption efficiency $\eta = 100\%$. In this limiting case, a QWP can have comparable performance as an MCT detector. This is not totally impractical in infrared range. For example, in [36] and [37], QWP structures having their modes coupled with high quality-factor waveguides yield micro-cavity polaritons. The structures with low doping density, low dark current yet high absorption efficiency can be achieved. Overall, for the selection of number of wells N in the design of THz QWP, one can only follow a general guideline that to improve the absorption efficiency with a least number of quantum wells.

Chapter 3

Design of QWP

In this chapter, the design and simulation results of THz QWP are presented. Due to the application purpose, the THz QWP is aimed at 4 THz peak response. This corresponds to the photon energy of 16 meV. The electron excitation mechanism is chosen to be bound-to-continuum because of its higher performance than the other structure, such as bound-to-bound. This requires that the energy of the first excited state of electrons in the quantum well aligns with the conduction band minimum of the barrier material.

First, the MQW (Multiple Quantum-Well) structure serves the fundamental role for the performance of QWP. A number of performance parameters of QWP are subject to the MQW structure, such as cut-off frequency, absorption quantum efficiency, responsivity, NEP , specific detectivity, etc. Thus, the design of the MQW structure is presented first in Section 3.1.

Besides the MQW structure, another component of the QWP, the grating coupler, is important in achieving a high absorption efficiency as well, as discussed in Chapter 1.1. In the second section of this chapter, the design of grating coupler will be shown.

3.1 Design of MQW Structure

For the design of MQW structure, several structural parameters need to be determined: the quantum well width, the barrier width, Aluminum fraction x in barrier

material $\text{Al}_x\text{Ga}_{1-x}\text{As}$, the doping density in the quantum well material GaAs, the doping location in the quantum well material, the number of wells. Due to the fact that there are several structure parameters that need to be optimized, we first made a rough estimation.

We approximate one quantum well structure in the QWP as an infinite quantum well. We can estimate the energy separation between the first lowest states, which is a function of well width w . This energy separation needs to equal THz radiation photon energy 16meV . Therefore, we can estimate the quantum well width w . Given the well width w , the absolute ground state energy (energy zero point is chosen to be the well bottom) can be calculated. Since the energy of the first excited state is aligned with the barrier material conduction band minimum, the well depth (in energy) is known, which can determine the Aluminum fraction in the barrier material, due to the fact that the conduction band offset energy CBO is simply $0.898x\text{ eV}$ [38].

Given the above guideline, with the real material parameters of GaAs and $\text{Al}_x\text{Ga}_{1-x}\text{As}$, the estimated well width is roughly between 120 \AA and 210 \AA , and the Aluminum fraction is between 0.02 and 0.03. Other numbers out of these ranges do not satisfy the requirement of THz QWP with peak absorption at 4 THz.

For each of the Aluminum fraction x chosen, there is an optimum well width that satisfy the requirements that the energy separation between the lowest two quantum well states is 16meV and that the first excited state aligns with the conduction band minimum of the barrier. Therefore, the oscillation strength and the absorption efficiency can be obtained. By comparing all these results for several different x , the results that give the highest absorption efficiency are chosen. Considering the real device has wider linewidth, the relation between absorption efficiency and absorption frequency at certain Aluminum fraction and well width values is found. Moreover, due to the real case when MBE growth is performed, the 3D carrier density is fixed to be 10^{17} cm^{-3} in the simulation, and this is a decent value according to the discussion in Chapter 2.3.2 [25].

Based on the above analysis and estimation, a more accurate calculation is performed. The calculation model is based on the Envelope Function Approximation

(EFA) and $k \cdot p$ method for MQW [39]. Detailed analysis of the simulation model and calculation are beyond the scope of this thesis.

Fig. 3-1 shows the absorption spectra of different Aluminum fractions and well widths using Eqn. (2.27). Aluminum fractions of 1.5%, 1.8%, 2.2%, 3.0% are sampled here. From lower curve to higher curve, the well widths change from 80\AA to 230\AA , with a step of 30\AA . Doping concentration is $n_{e,3D} = 10^{16}\text{cm}^{-3}$ in the well. The notes on the graph shows the highest absorption coefficient at 4THz and the corresponding well width for this absorption coefficient to achieve.

Fig. 3-2 shows the simulated absorption coefficient at 4THz vs. well width, for different Aluminum fractions. The dots with the same color as the curves show the well width for this Aluminum fraction when the first excited state is aligned with the conduction band minimum. The position of the dots show the well width and the corresponding maximum absorption efficiency. The numbers beside the dots show the frequency values when peak absorption coefficients are achieved. From the simulation work, several conclusions can be drawn.

First, for a fixed Aluminum fraction, increasing well width induces the increase of oscillation strengths because the overall out-of-plane dimension increases. This causes the peak absorption coefficient to increase at first, and gradually level off when the well width is large enough because the photon energy it can support drops. Meanwhile, as the well width increases, the peak absorption frequency is increased at first, and drops as the well further widens. Therefore, the well width should not be too large or too small so that a right peak absorption frequency can be achieved. For the target absorption frequency of 4 THz, the well width is somewhere between 120\AA and 210\AA , as stated above.

Second, it is difficult to achieve peak absorption at low frequency with high Aluminum fraction. This is easy to understand, because high Aluminum fraction gives large energy barrier height, increasing the subband energy separation. For the same reason, it is also difficult to achieve peak absorption at high frequency with low Aluminum fraction. Therefore, an appropriate Aluminum fraction is required for peak absorption at 4THz. From Fig. 3-1 and Fig. 3-2, it can be concluded that Aluminum

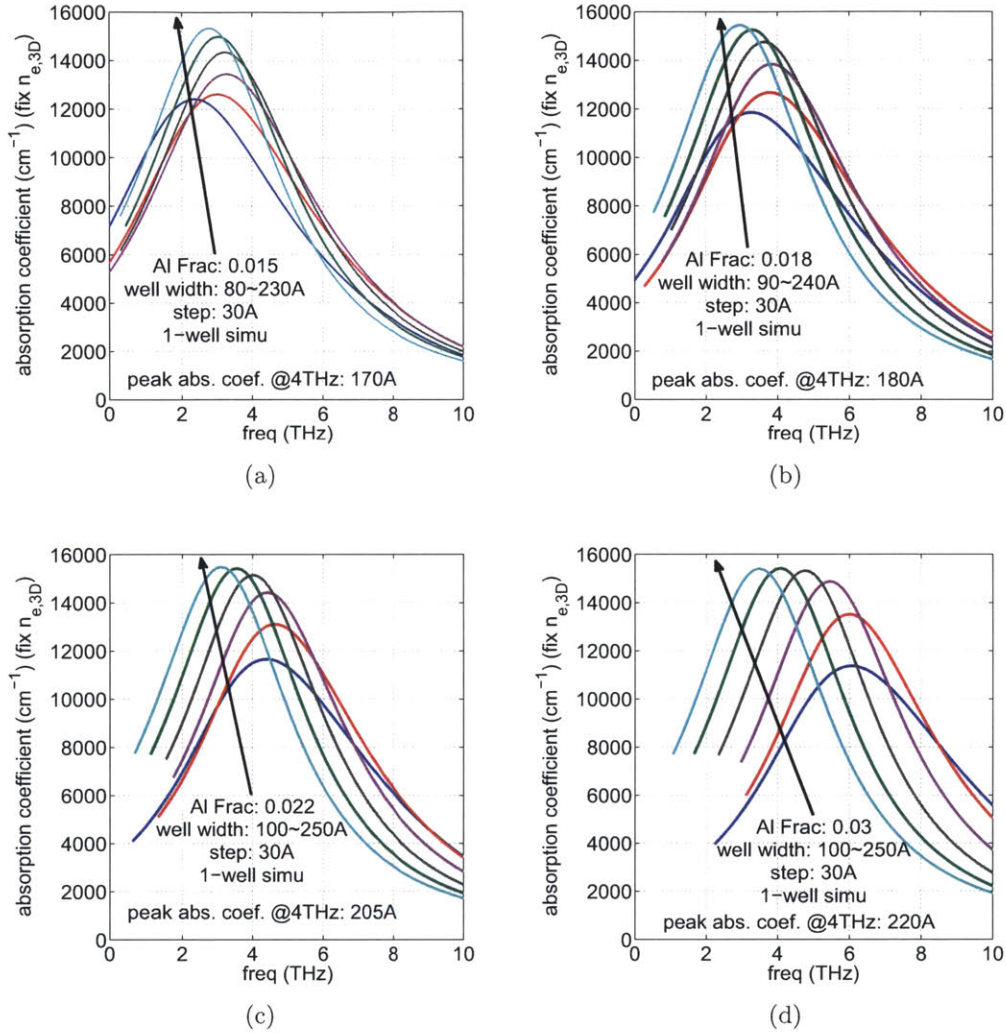


Figure 3-1: Simulation results of absorption coefficient vs. frequency. Different curves show the relation in different quantum well widths. The simulation model is one-well model. The four plots show different Aluminum fractions x . (a) $x = 1.5\%$. The highest absorption at 4 THz is 13220 cm^{-1} with 170\AA well width. (b) $x = 1.8\%$. The highest absorption at 4 THz is 14550 cm^{-1} with 180\AA well width. (c) $x = 2.2\%$. The highest absorption at 4 THz is 15230 cm^{-1} with 205\AA well width. (d) $x = 3\%$. The highest absorption at 4 THz is 15280 cm^{-1} with 220\AA well width.

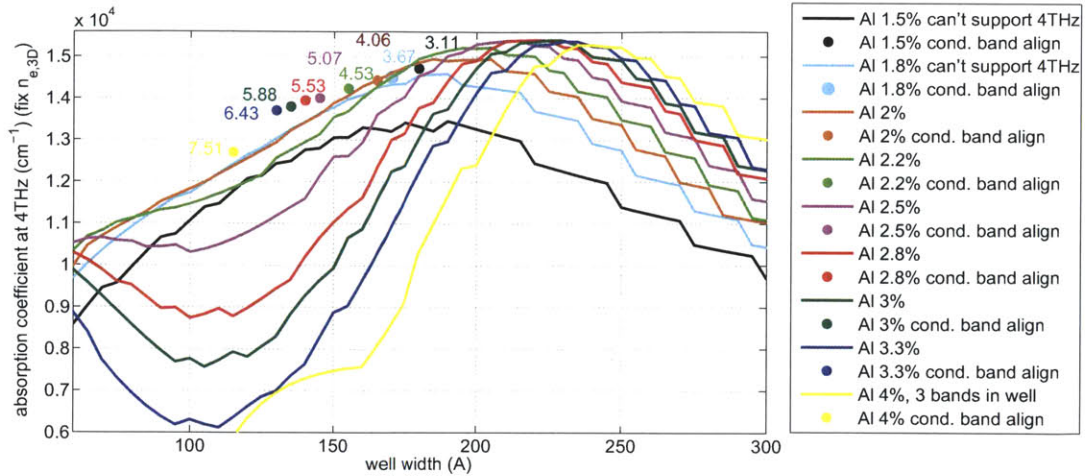


Figure 3-2: The curves show the absorption coefficient at 4THz vs. well width, for different Aluminum fractions. The dots with the same color as the curves show the well width for this Aluminum fraction when the first excited state is aligned with the conduction band minimum. The position of the dots show the well width and the corresponding maximum absorption efficiency. The numbers beside the dots show the frequency values when peak absorption coefficients are achieved.

fraction should be chosen between 2% and 3%. In fact, when the Aluminum fraction is below 2%, the structure cannot support a 4THz photon absorption, and when the Aluminum fraction is above 4%, three, instead of two electron subbands will appear in the quantum well, causing the absorption at 4THz to drop.

For a fixed Aluminum fraction, the well width for the 1st excited state to align with the conduction band is slightly smaller than the well width for largest peak absorption frequency. The peak absorption frequency when aligned is slightly smaller than the largest peak absorption frequency that can be achieved.

When comparing the optimal performance of a structure with the 4THz absorption, it can be found that the well width for the largest 4THz absorption is slightly larger than the well width for alignment given a fixed Aluminum fraction. Meanwhile, the peak absorption of the former is also slightly larger than the latter.

Furthermore, if the well is wide and Aluminum fraction is high, it is possible that the 1st excited state stays inside the quantum well. This will cause the absorption coefficient to drop, as mentioned above. If the well is narrow and Aluminum fraction

Al Frac. (%)	Well Width (Å) for 1 st excited state to align with Cond. Band	Peak Abs. Freq. (THz)	Peak Abs. Coef. (cm ⁻¹)
1.5	185	3.108	14720
1.8	170	3.671	14500
2.2	155	4.531	14230
2.5	145	5.071	14000
2.8	140	5.526	13940
3.0	135	5.882	13800
3.3	130	6.430	13700

Table 3.1: For different Aluminum fractions, the well widths for 1st excited state to align with conduction band, the peak absorption frequencies at alignment, and the corresponding peak absorption coefficients are shown in the table.

is small, it is possible that the 1st excited state is higher than the conduction band edge of the barrier material. This may increase the absorption coefficient, but the structure may be unable to support 4THz absorption.

From Fig. 3-1, Fig. 3-2, the data shown in Table 3.1, and the above discussion, we can see that a QWP structure of an Aluminum fraction of 2.2% and well width of around 160Å appears to be the optimum choice for 4THz absorption, because at 4THz, the peak absorption is the highest among all the Aluminum fractions that have been calculated. The peak absorption at alignment 4.53THz is not far from the required 4THz as well. For the other Aluminum fraction values such as 2.5%, 2.8%, 3.0%, 3.3%, as can be seen in Fig. 3-2, although the peak absorption values are quite comparable with the case of 2.2%, they suffer from two drawbacks. First, their peak absorption coefficients when alignment is satisfied (by choosing the right well widths) are lower than that of 2.2% case. Besides, the frequency at peak absorption in the alignment is far from 4 THz. In fact, Aluminum fraction of 2.0% also turns out to be a good structure, but since in the real MBE growth, a difference of 0.2% in Aluminum fraction cannot be distinguished well, and small Aluminum fraction is harder to control than large fraction, the 2.2% Aluminum fraction value is chosen here.

For the choice of barrier width, the principle is to increase the detectivity, which requires the decrease of barrier width. However, the inter-well tunneling should be

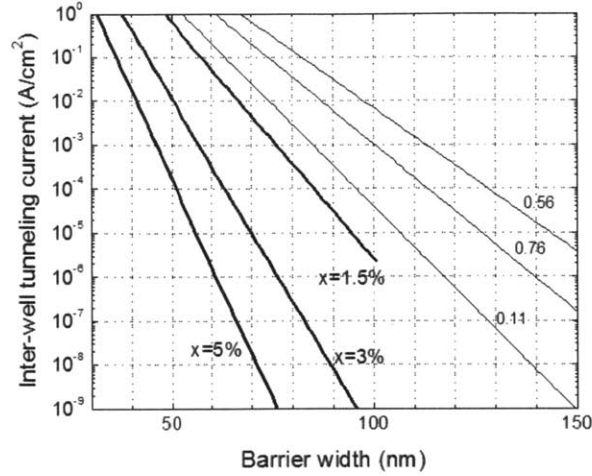


Figure 3-3: The tunneling current between each wells in MQW structure vs barrier widths. Different lines show different Aluminum fraction for the barrier material. The figure is derived from [27].

minimized, so that the barrier width should not be too thin. Based on the work of [27], a well width of 850 \AA is chosen to restrict the interwell tunneling current below 10^{-5} A/cm^2 which is comparable with the estimated background current. This is also shown in Fig. 3-3.

The number of wells is chosen to be 25, which is expected to help improving the QWP performance, as can be seen more clearly in the later section, Chapter 3.2. The doping is n-type, using Si as the dopant and in the central 50 \AA region in the quantum wells. The doping concentration is chosen to be 10^{17} cm^{-3} .

A remaining question is the width and doping density of the electrode contact layers at both terminals of the device. While the doping level needs to remain high to ensure Ohmic contact, these parameters are also related to carrier absorption, as discussed in detail in the next section, Chapter 3.2.

3.2 Design of Grating Coupler

QWP does not absorb light of which the polarization is parallel to the quantum well planes. This is determined by intersubband transition which has been discussed in Chapter 2.1. However, when the QWP is used for focal plane array (FPA) imaging,

the common incidence mode is shining light perpendicular to the QWP plane, which means the polarization of the incoming light is in the quantum well plane, or perpendicular to the MQW growth direction. In the case of FPA imaging, the 45° incidence is not applicable, and a grating coupler structure is a solution for this.

A 2D grating coupler can be made for 2D focal plane array. In our study, a 1D grating coupler [26] is made in order to test its performance in coupling light. Finite Element Method (FEM) in Electromagnetic (EM) simulation is performed using the commercial software COMSOL. Since the grating coupler is 1D, which means the metal strip is very long in one dimension and very small in the other two, a 2D EM simulation model can be used with sufficient accuracy and reliance. Based on the quantum well structures and absorption coefficient obtained from last section, Chapter 3.1, we can build the EM 2D simulation model as in Fig. 3-4.

One period of the grating coupler is built in the simulation model and periodic boundary condition is used in the left and right boundary of the model, as shown in Fig. 3-4. The left structure shows the overall view of the model, except for the trimmed air and PML (Perfectly-Matched Layer) regions. The right structure shows an enlarged portion of the boxed region in the left structure. The enlarged view shows the detailed structure of the model. From top to bottom, the layers are: metal grating, n+ top contact layer, last barrier layer, Multi-Quantum well (MQW) layer, n+ bottom contact layer (plasma reflector), substrate layer, and PML. Below the enlarged view, the material and thickness of each layer are shown. The thicknesses of the substrate and PML are not critical, as long as they can make sure to absorb all the light coming from the top, thus prevent the reflectance from the bottom due to calculation model rather than the actual case. The thicknesses of the MQW layer and the last barrier layer are based on the discussion and calculation of Chapter 3.1. The thickness of the metal grating is not important either, because it does not make much difference in diffracting incoming light.

Analytically, the field can be expressed as [26]

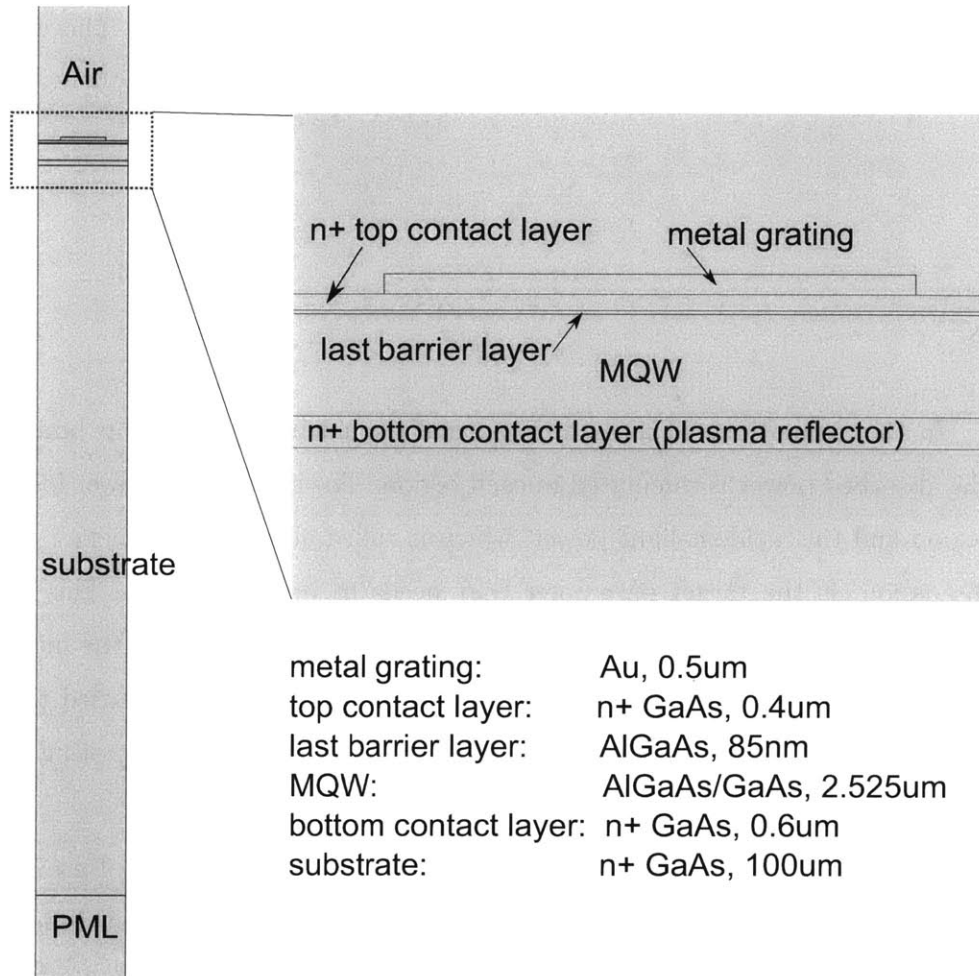


Figure 3-4: The 2D simulation model for the QWP EM simulation. The left structure shows the overall view of the model, except for the trimmed air and PML regions. The right structure shows an enlarged portion: metal grating, n+ top contact layer, last barrier layer, Multi-Quantum well (MQW) layer, n+ bottom contact layer (plasma reflector), substrate layer, and PML. Below the enlarged view, the material and thickness of each layer are shown.

$$\phi(x, y, z) = e^{-j\beta y} \sum_{n=-\infty}^{\infty} e^{-j\alpha_n x} (A_n e^{-j\gamma_n z} + B_n e^{j\gamma_n z}) \quad (3.1)$$

where z is the MQW growth direction, x is the grating coupler repetition direction, and y is the grating coupler direction (long edge direction). The wave vector components are

$$\alpha_n = \alpha + \frac{2\pi n}{p} \quad (3.2)$$

$$\gamma_n = \sqrt{\epsilon k_0^2 - \alpha_n^2 - \beta^2} \quad (3.3)$$

In the simulation, 4THz light is normally incident from the top boundary, and the absorbed power is calculated in each region. The ratio of the power loss in MQW region and the incident light power, which is called absorption efficiency in the later discussion, is the target parameter that needs to be maximized. The thicknesses and doping levels of the top and bottom contact layers, as well as the metal grating period p and duty cycle DC are the parameters that need to be varied through the EM simulation in order to optimize the absorption efficiency. The grating period p is close to the wavelength of the EM wave inside the semiconductor

The models for materials are mainly the permittivity models. Here we use the drude model for all the materials, because the light absorption in doped GaAs is observable. In fact, it is through the doping-induced light absorption and reflection that more THz radiation can be absorbed in the MQW region. In the drude model, the permittivity is complex and is a function of doping level in semiconductors and light frequency. Particularly, in GaAs, for certain doping level, the material appears reflective for 4THz radiation, because the real part of the permittivity is negative and very large, and the imaginary part is very small. This induces an almost purely imaginary refractive index, which causes the light to reflect at its surface, thus the name plasma reflector. In order to improve light absorption in MQW region, we can take advantage of this plasma reflector and put a layer of appropriately doped GaAs

at the bottom of the MQW. Thus the light that is not absorbed by MQW at the first pass can be reflected by the plasma reflector and have MQW to absorb the light for the second time. Most possibly, the reflected light can be partially absorbed in MQW and partially reflected again in metal grating, causing another cycle of light absorption and reflection.

Fig. 3-5 shows the simulated color plot of the 1D grating coupler QWP. The color in the structure shows the magnitude of the electric field and the color legend is shown. The left figure is when incident light is 2.5THz and the right one is when incident light is 3THz. Each layer of the structure is annotated. From the figure, it can be seen the incident light coming from the top to the bottom is diffracted in the metal grating-MQW-plasma reflector region, and attenuated dramatically when it reaches the substrate. The light is almost damped into zero in the substrate region. The PML further ensures no reflected light is from the substrate or the boundary.

Fig. 3-6 shows five simulated color plots of the 1D grating coupler QWP in different frequencies: (a) 2.5THz, (b) 3THz, (c) 4THz, (d) 5THz, (e) 6THz. From the plots, the light diffraction by the metal grating-MQW-plasma reflector region can be clearly observed. Different frequencies also show different diffraction and absorption properties for the same structure. 2.5THz and 3THz shows strong diffraction in the metal grating and plasma reflector layer. When frequency increases, MQW absorption is more effective and light diffraction is not very observable. Little amount of light leak into the plasma reflector and substrate layers. From the figure, it can be seen that the diffracted beam is no longer evanescent above 4THz because the higher frequency renders real value of the wave vector in z direction.

Given the physics picture described above, several factors need to be taken into consideration in the design.

First, the top contact layer is doped to ensure ohmic contact for semiconductor and metal. In order to decrease light absorption in this region, it should not be too heavily doped or too thick. A thickness of $0.4 \mu m$ and n-type doping level of $10^{17} cm^{-3}$ is chosen.

Second, based on the above discussion, the bottom contact layer doping level is

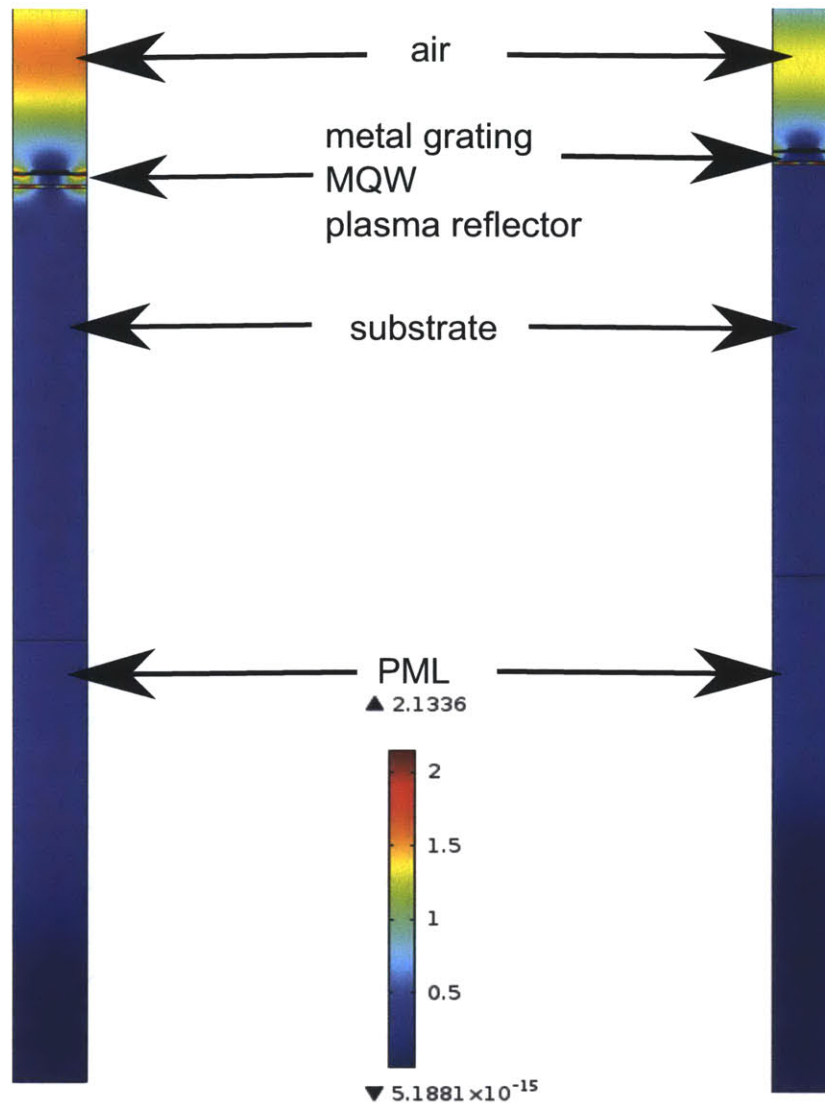


Figure 3-5: A simulated figure of the 1D grating coupler QWP. The color in the structure shows the magnitude of the electric field and the color legend is shown. The left figure is when incident light is 2.5THz and the right one is when incident light is 3THz. The incident light coming from the top to the bottom is diffracted in the metal grating-MQW-plasma reflector region, and attenuated dramatically when it reaches the substrate. The light is almost damped into zero in the substrate region.

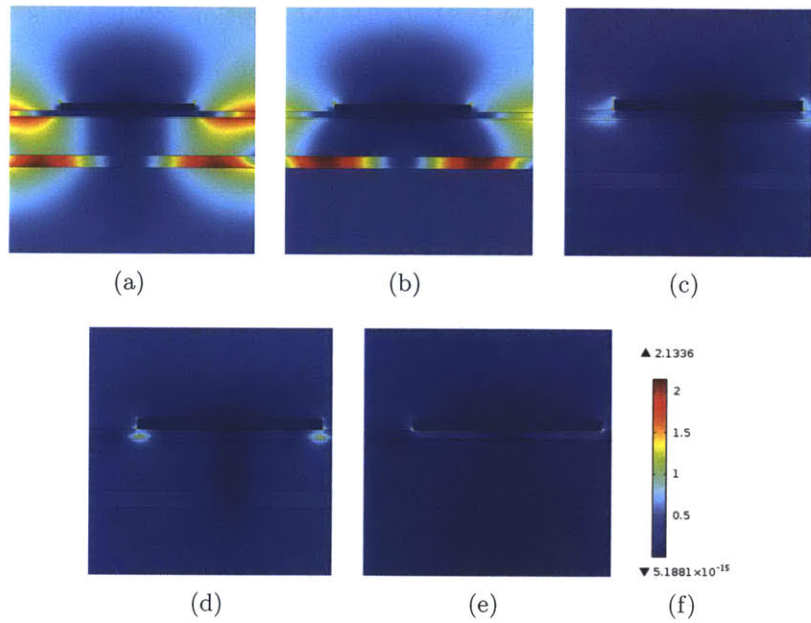


Figure 3-6: Simulated color figures of the 1D grating coupler QWP. The colors in the enlarged structures show the magnitude of the electric field and the color legend is shown in (f). The frequencies in these plots are (a) 2.5THz, (b) 3THz, (c) 4THz, (d) 5THz, (e) 6THz. From the plots, the light diffraction by the metal grating-MQW-plasma reflector region can be clearly observed. Different frequencies also show different diffraction and absorption properties for the same structure.

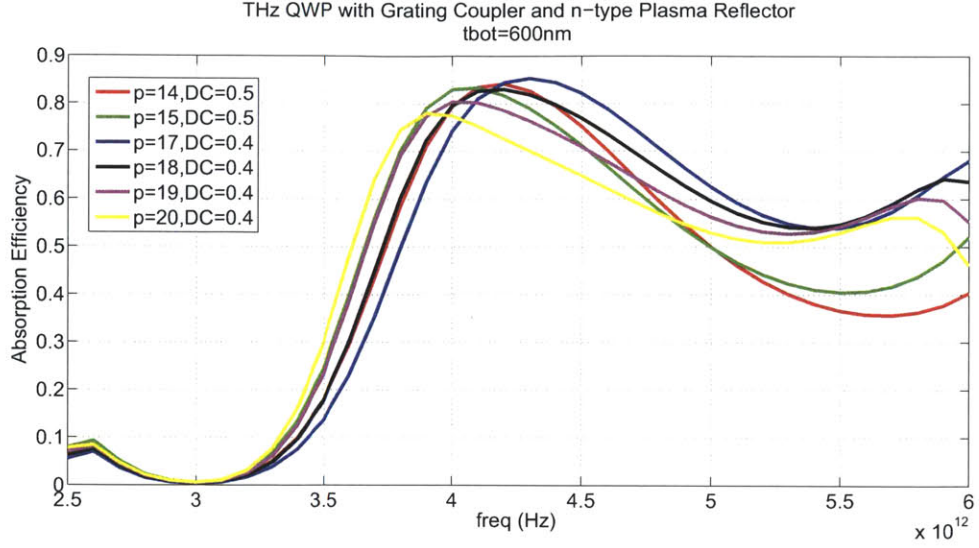
chosen to be $5 \times 10^{18} \text{ cm}^{-3}$. At this doping level, GaAs serves as a reflector for 4THz light. Through COMSOL simulation, the 4THz absorption in MQW is not sensitive to the thickness of this plasma reflector layer, which is shown in Fig. 3-7 and discussed later. Therefore, an appropriate thickness value of 600nm is chosen and a number of grating coupler period values and duty cycle values are chosen in order to pick up the best structure.

Fig. 3-7 plots the absorption efficiency in the active region, i.e. the multi-quantum well (MQW) region of the QWP. Here, the absorption efficiency is the ratio of the THz power absorbed in the MQW and the incident THz power:

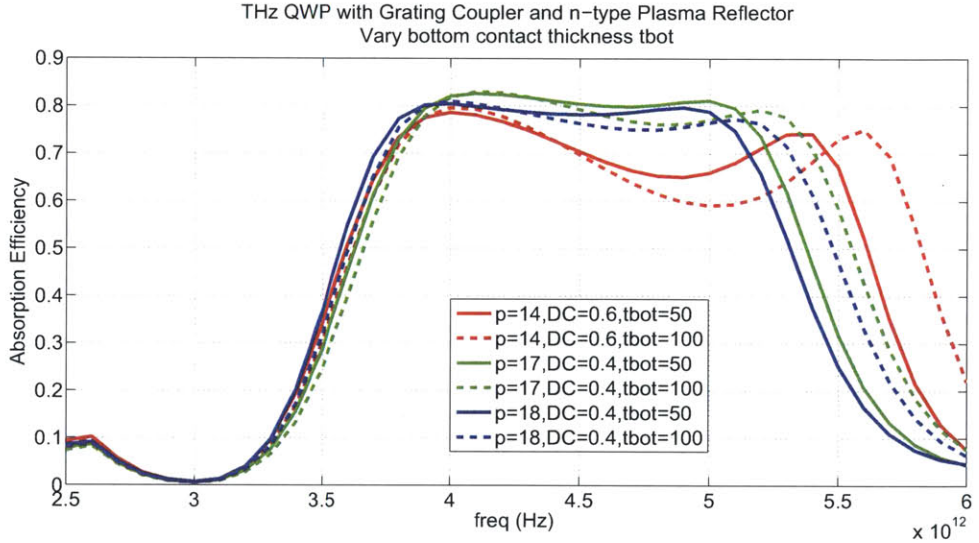
$$\eta_{abs} = \frac{\int_{MQW} \text{Re}\{j\omega\epsilon^* \vec{E} \cdot \vec{E}^*\} dV}{\int_{Incident\ Plane} \frac{1}{2} \text{Re}\{\vec{E} \times \vec{H}^*\} \cdot d\vec{S}} \quad (3.4)$$

In the structure, grating coupler and n-type plasma reflector are used. The simulation model is in Fig. 3-4. The simulation parameters are: MQW absorption coefficient is a function of frequency and is from Fig. 3-1c. The top n-type contact layer doping level is $n_{top} = 10^{17} \text{ cm}^{-3}$. The bottom n-type contact layer serves as a plasma reflector as well. Its doping level is $n_{bot} = 5 \times 10^{18} \text{ cm}^{-3}$. The n-type substrate doping level is $n_{sub} = 10^{18} \text{ cm}^{-3}$. The curves show the absorption efficiency with different grating period p and Duty Cycle DC , which are shown in the legend. The unit of p is μm . This figure shows the structures with relatively high absorption efficiency at 4THz by choosing appropriate values of grating period and duty cycle. Generally, the absorption efficiencies at 4THz are approximately 80%. Fig. 3-7a uses fixed bottom n-type contact thickness $t_{bot} = 600 \text{ nm}$. Fig. 3-7b changes bottom n-type contact thickness t_{bot} to 50 nm and 100 nm, as shown in the legend. The unit for t_{bot} is nm.

From Fig. 3-7, it can be found that by choosing the right grating coupler period and duty cycle, the absorption efficiency of the grating coupler THz QWP can exceed 80% at 4THz, and the absorption spectra are flat at the vicinity of 4THz, which means the absorption efficiency does not change much when the frequency changes a small amount from 4THz. This is advantageous. Furthermore, comparing Fig. 3-



(a)



(b)

Figure 3-7: The simulated absorption efficiency vs. frequency of a THz microcavity-coupled QWP. In the structure, grating coupler and n-type plasma reflector are used. The simulation model is in Fig. 3-4. The simulation parameters are: MQW absorption coefficient is a function of frequency and is from Fig. 3-1c. The top n-type contact layer doping level is $n_{top} = 10^{17} \text{ cm}^{-3}$. The bottom n-type contact layer serves as a plasma reflector as well. Its doping level is $n_{bot} = 5 \times 10^{18} \text{ cm}^{-3}$. The n-type substrate doping level is $n_{sub} = 10^{18} \text{ cm}^{-3}$. Grating period p and Duty Cycle DC are shown in the legend. The unit of p is μm . The absorption efficiencies at 4THz can achieve 80%. (a) Use fixed bottom n-type contact thickness $t_{bot} = 600 \text{ nm}$. (b) Change bottom n-type contact thickness t_{bot} to 50 nm and 100 nm, as shown in the legend. The unit for t_{bot} is nm.

7a and Fig. 3-7b, it can be seen that even when the bottom contact layer (plasma reflector layer) thickness is as thin as 50nm or 100nm, the absorption efficiency is not degraded compared to a thick plasma reflector layer. This means the n-type plasma reflector at the doping level of $5 \times 10^{18} \text{ cm}^{-3}$ is very effective in reflecting off the THz radiation. The thinner plasma reflector layers even show a slight improvement in absorption efficiency at the frequency range of 4.5THz to 5.5THz. This is due to the fact that the plasma reflector also absorbs some light. The thicker the layer is, the more light it absorbs.

Next, the design and simulation of THz QWP-LED is shown.

The design of LED layers include the Aluminum fraction, doping level and thickness of each layer. Based on the existing work on GaAs/ $\text{Al}_x\text{Ga}_{1-x}\text{As}$ LED and mid-infrared QWP-LED, a widely-used structure is adopted here in the THz QWP-LED structure, as seen in Fig. 3-8. It is similar to the THz QWP structure as shown in Fig. 3-4. The difference is that below MQW layer, an LED layer, a p+ plasma reflector layer and a p+ bottom contact layer are used. Below these semiconductor layers, BCB and sapphire substrate are used, and BCB serves as the bonding layer between GaAs semiconductor and sapphire substrate. From top to bottom, the LED layer consists of 130nm undoped $\text{Al}_{0.022}\text{Ga}_{0.978}\text{As}$, 40nm undoped GaAs, 40nm undoped $\text{Al}_{0.022}\text{Ga}_{0.978}\text{As}$, and 40nm undoped $\text{Al}_{0.1}\text{Ga}_{0.9}\text{As}$. The active region is the 40nm GaAs layer which is sandwiched in two barrier layers $\text{Al}_{0.022}\text{Ga}_{0.978}\text{As}$. While the barrier layer does not have very high energy barrier height, the 40nm undoped $\text{Al}_{0.1}\text{Ga}_{0.9}\text{As}$ is further attached here with higher barrier energy to ensure sufficient confinement for carriers. On top of the undoped $\text{Al}_{0.1}\text{Ga}_{0.9}\text{As}$ layer, heavily p-doped $\text{Al}_{0.1}\text{Ga}_{0.9}\text{As}$ is used as a plasma reflector, finalized with a heavily p-doped GaAs bottom contact layer. The thicknesses and doping levels of the last two layers (heavily p-doped $\text{Al}_{0.1}\text{Ga}_{0.9}\text{As}$ and GaAs) are to be optimized through EM simulation, which is shown later. In order to couple out the emitted near-infrared radiation from LED layers, a near-infrared transparent material sapphire is used as a substrate. BCB, which is transparent in near-infrared range and strong enough, is used as the bonding layer to bond together the QWP-LED semiconductor device and sapphire substrate.

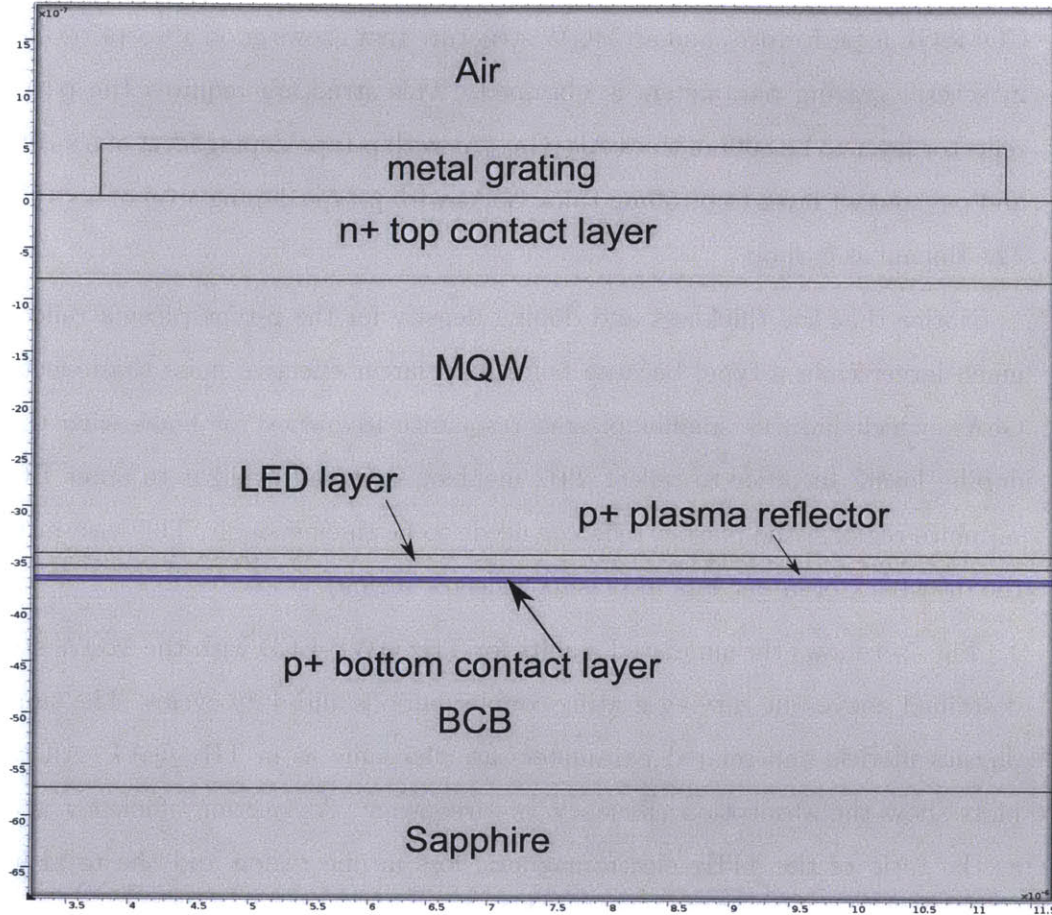


Figure 3-8: The figure shows the layered structure of THz QWP-LED. Below MQW layer, an LED layer, a p+ plasma reflector layer, a p+ bottom contact layer, BCB and sapphire substrate are used. From top to bottom, the LED layer consists of 130nm undoped $\text{Al}_{0.022}\text{Ga}_{0.978}\text{As}$, 40nm undoped GaAs, 40nm undoped $\text{Al}_{0.022}\text{Ga}_{0.978}\text{As}$, and 40nm undoped $\text{Al}_{0.1}\text{Ga}_{0.9}\text{As}$. The active region is the 40nm GaAs layer which is sandwiched in two barrier layers $\text{Al}_{0.022}\text{Ga}_{0.978}\text{As}$. Heavily p-doped $\text{Al}_{0.1}\text{Ga}_{0.9}\text{As}$ is used as a plasma reflector, finalized with a heavily p-doped GaAs bottom contact layer.

Next, as in the practice in designing THz QWP, the plasma reflector and p-type contact layer needs to be optimized by varying their thicknesses and doping levels. The goal is to maximize the THz absorption in MQW region, the same with THz QWP. Together with the grating period and duty cycle, FEM simulation using COMSOL is performed, and an MQW structure that shows good absorption efficiency in several grating parameters is obtained. This structure requires the p+ plasma reflector layer to be 800nm thick $\text{Al}_{0.1}\text{Ga}_{0.9}\text{As}$ with p-type doping level of $5 \times 10^{19} \text{cm}^{-3}$, and p+ contact layer to be 50nm thick GaAs with p-type doping level of $8 \times 10^{18} \text{cm}^{-3}$. The dopant is carbon.

Notice that the thickness and doping density for the p-type plasma reflector are much larger than n-type, because holes have larger effective mass than electrons in GaAs, which induces smaller plasma resonance frequency for holes with the same doping level. In order to reflect THz incident light and avoid it to enter BCB and sapphire regions, the plasma reflector needs to be thick enough. This also introduces the drawback of larger loss in plasma reflector region.

Fig. 3-9 shows the simulated results for THz QWP-LED with the MQW structure described above but varying grating coupler periods and duty cycles. The simulation physics models and related parameters are the same as in THz QWP. All the four plots show the absorption efficiency vs. frequency. Absorption efficiency is defined as the ratio of the 4THz electromagnetic loss in one region and the total incident power flux, the same as in THz QWP, as in Eqn. (3.4). In each of the four plots, absorption efficiency spectra in MQW (QWP region), n+ top contact layer, LED region, p+ $\text{Al}_{0.1}\text{Ga}_{0.9}\text{As}$ plasma reflector layer, and p+ bottom contact layer are shown in different colors: blue, green, red, cyan, and purple, respectively. The absorption efficiency in MQW (blue curve) at 4THz is the value we would like to maximize. The metal grating period p and duty cycle DC are annotated in each of the plots. The unit for p is μm . The grating periods and duty cycles in all the four plots (a)-(d) are: (a) $p = 15\mu\text{m}, DC = 0.5$. (b) $p = 16\mu\text{m}, DC = 0.5$. (c) $p = 17\mu\text{m}, DC = 0.5$. (d) $p = 18\mu\text{m}, DC = 0.5$. Except for these grating coupler structures, another four grating coupler structures also show similar performance in absorption efficiency.

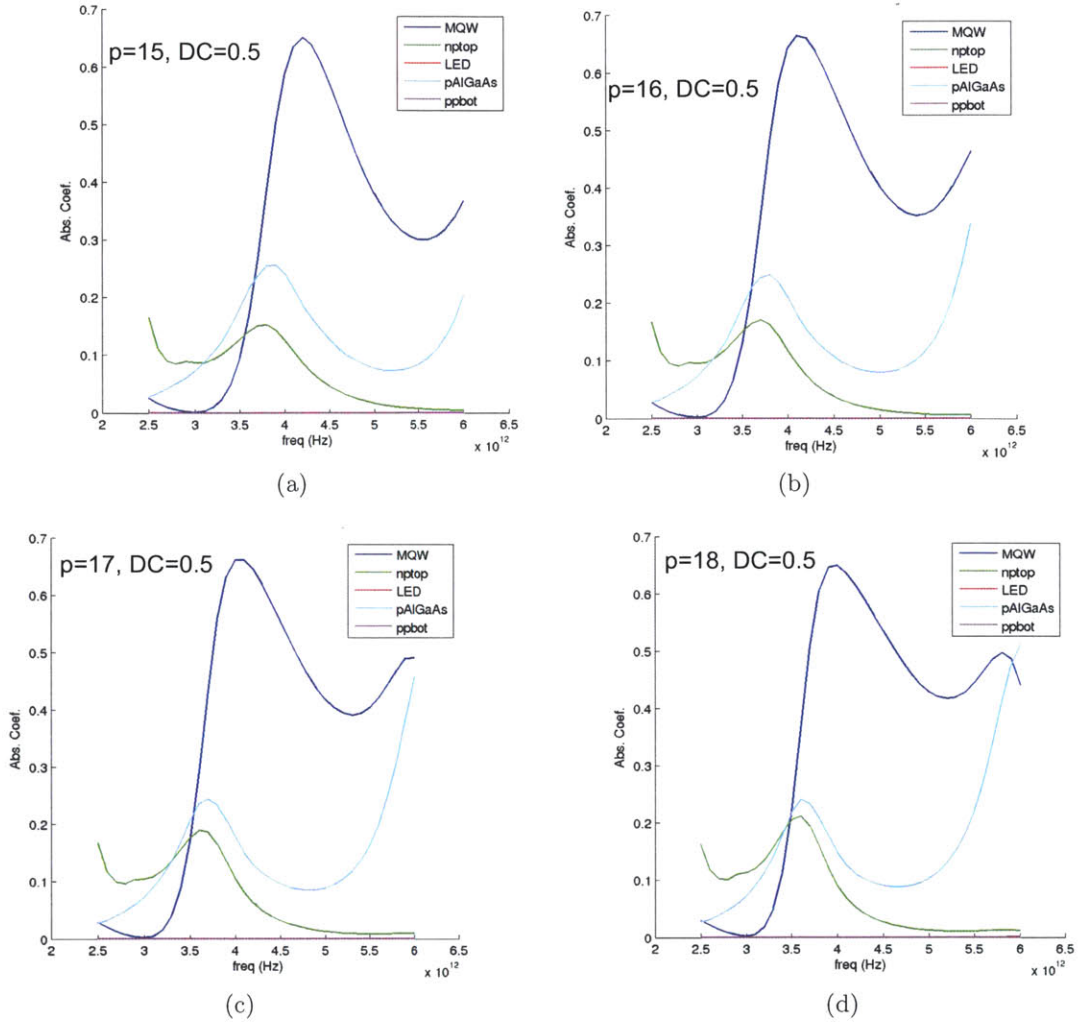


Figure 3-9: The figure shows the simulated results for THz QWP-LED with the MQW structure described above but varying grating coupler periods and duty cycles. The simulation physics models and related parameters are the same as in THz QWP. All the four plots show the absorption efficiency vs. frequency. Absorption efficiency is defined as the ratio of the 4THz electromagnetic loss in one region and the total incident power flux, the same as in THz QWP. In each of the four plots, absorption efficiency spectra in MQW (QWP region), n+ top contact layer, LED region, p+ Al_{0.1}Ga_{0.9}As plasma reflector layer, and p+ bottom contact layer are shown in different colors: blue, green, red, cyan, and purple, respectively. The absorption efficiency in MQW (blue curve) at 4THz is the value to be maximized. The metal grating period p and duty cycle DC are annotated in each of the plots. The unit for p is μm . (a) $p = 15\mu m, DC = 0.5$. (b) $p = 16\mu m, DC = 0.5$. (c) $p = 17\mu m, DC = 0.5$. (d) $p = 18\mu m, DC = 0.5$.

They are: $p = 18\mu m, DC = 0.4$; $p = 19\mu m, DC = 0.4$; $p = 20\mu m, DC = 0.4$; $p = 21\mu m, DC = 0.4$.

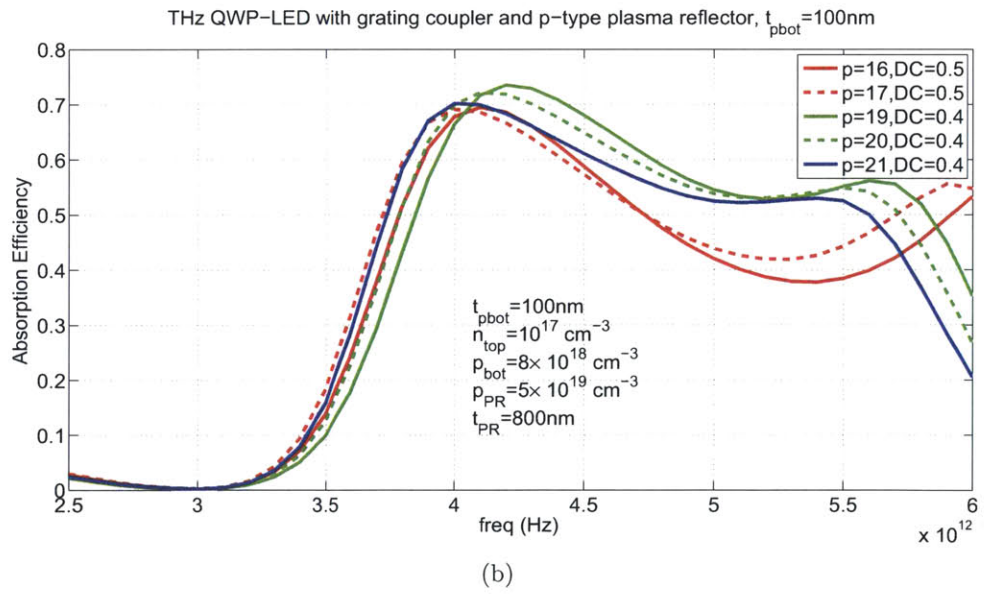
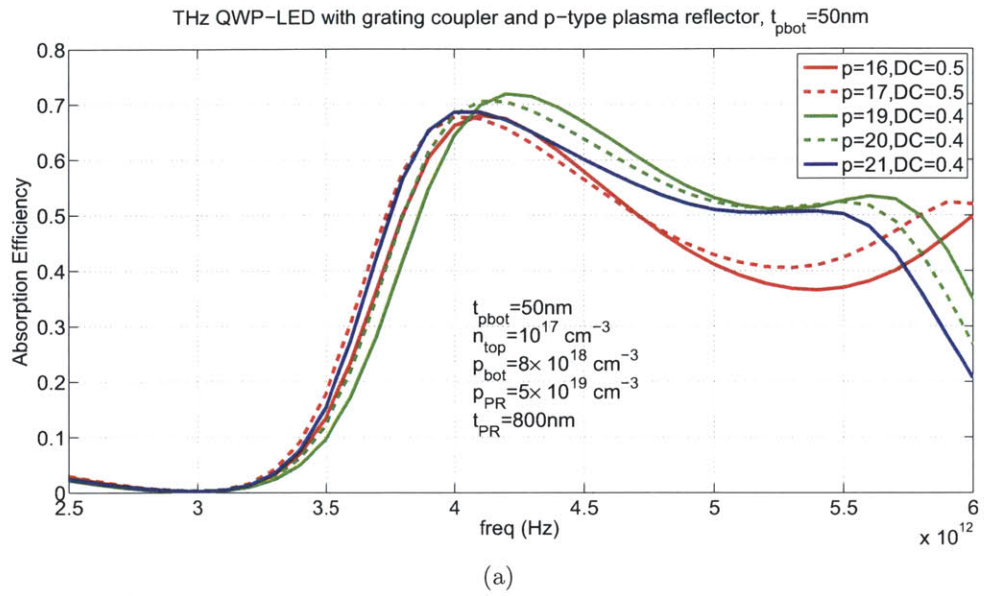
In Fig. 3-9, among all the four plots, LED absorption is very small and negligible, because LED region is undoped semiconductors. Absorption in p-type bottom contact layer is also very small, because it is thin and relatively lightly doped. The n+ top contact layer and p+ plasma reflector layer show somewhat higher absorption, because of their higher doping and the larger thickness of plasma reflector. Nevertheless, their absorption efficiency is generally below 30%. The absorption efficiency in MQW remarkably exceeds the other regions, and peak at the vicinity of 4THz with a peak value approaching 70%. This number, although smaller than that in THz QWP which uses n-type plasma reflector, is still satisfactory for real application.

The following parts verify that the MQW structure shown above is the optimal structure. The MQW layers in our optimization process include the p-type $Al_{0.1}Ga_{0.9}As$ plasma reflector layer and the p-type GaAs bottom contact layer. They are the main parameters in the optimization shown here, because they are unique to QWP-LED. Other MQW structures are either in THz QWP, or in conventional LED structure. The parameters to be optimized are their thicknesses and doping concentrations, mainly p-type bottom contact layer thicknesses t_{pbot} , p-type plasma reflector doping concentration p_{PR} , and p-type plasma reflector thickness t_{PR} .

First, the effect of p-type bottom contact layer thicknesses t_{pbot} is analyzed. Fig. 3-10 shows the simulated absorption efficiency spectrum in THz QWP-LED with different p-type bottom contact layer thicknesses t_{pbot} . (a) $t_{pbot} = 50nm$. (b) $t_{pbot} = 100nm$. (c) $t_{pbot} = 150nm$. The other parameters are chosen as below. N-type contact layer doping concentration $n_{top} = 10^{17}cm^{-3}$. P-type bottom contact layer doping concentration $p_{bot} = 8 \times 10^{18}cm^{-3}$. P-type plasma reflector doping concentration $p_{PR} = 5 \times 10^{19}cm^{-3}$, thickness $t_{PR} = 800nm$. These parameters are shown in the plots. Each plot shows several curves with different grating coupler periods p and duty cycles DC . They are shown in the legends. The unit of p is μm . From the figure, it can be seen that the absorption efficiency peaks at approximately 4THz with a value exceeding 70%. The MQW and grating coupler structures are chosen to

have optimal performance. Comparing Figs. 3-10a, 3-10b and 3-10c, it can be found that the absorption efficiency is not sensitive to the thickness of the p-type bottom contact layer t_{pbot} when it is varied from 50nm to 150nm. Therefore, a thickness of 50nm is chosen in the real structural growth.

Next, p-type plasma reflector doping concentration p_{PR} is varied to show its effect on absorption efficiency in MQW region. Fig. 3-11 shows the simulated absorption efficiency spectrum in THz QWP-LED with the p-type plasma reflector doping concentrations p_{PR} different from the optimized value $5 \times 10^{19} cm^{-3}$. The doping values chosen to be shown here are $5 \times 10^{18} cm^{-3}$ (in (a) and (b)) and $2.6 \times 10^{19} cm^{-3}$ (in (c) and (d)). The other parameters are chosen to be the optimized values and are shown as below. N-type contact layer doping concentration $n_{top} = 10^{17} cm^{-3}$. P-type bottom contact layer doping concentration $p_{bot} = 8 \times 10^{18} cm^{-3}$. P-type bottom contact layer thicknesses $t_{pbot} = 50nm$. P-type plasma reflector thickness $t_{PR} = 800nm$. Each plot shows several curves with absorption efficiencies in different regions of the THz QWP-LED structure and these notations are the same as in Fig. 3-9. Devices with different grating coupler periods p and duty cycles DC are also shown: (a) and (c) show $p = 16\mu m, DC = 0.5$, (b) and (d) show $p = 17\mu m, DC = 0.5$. The unit of p is μm . From the figure, it can be seen that when p_{PR} is reduced by one order of magnitude from the optimized value, the absorption in MQW region is extremely small, even less than 10%, while the absorption in p-type plasma reflector is dominant. This is because that the decrease of plasma doping concentration induces a poor reflector and better absorber for THz light. When p_{PR} is increased to $2.6 \times 10^{19} cm^{-3}$, the absorption in MQW region increases, with the absorption efficiency peak at approximately 4.5THz and with a value slightly larger than 50%. This is improved but still not good enough. Meanwhile, the absorption in other regions are suppressed, but the p-type plasma reflector still maintains the absorption efficiency of around 40% as a peak value. Therefore, further increased plasma reflector doping is required. As shown in Fig. 3-9, the doping concentration of $5 \times 10^{19} cm^{-3}$ can give satisfactory absorption efficiency in MQW (approaching 70% near 4THz) and very small absorption in other regions (lower than 25% in the whole frequency range considered).



(Continue to next page)

(Continued from last page)

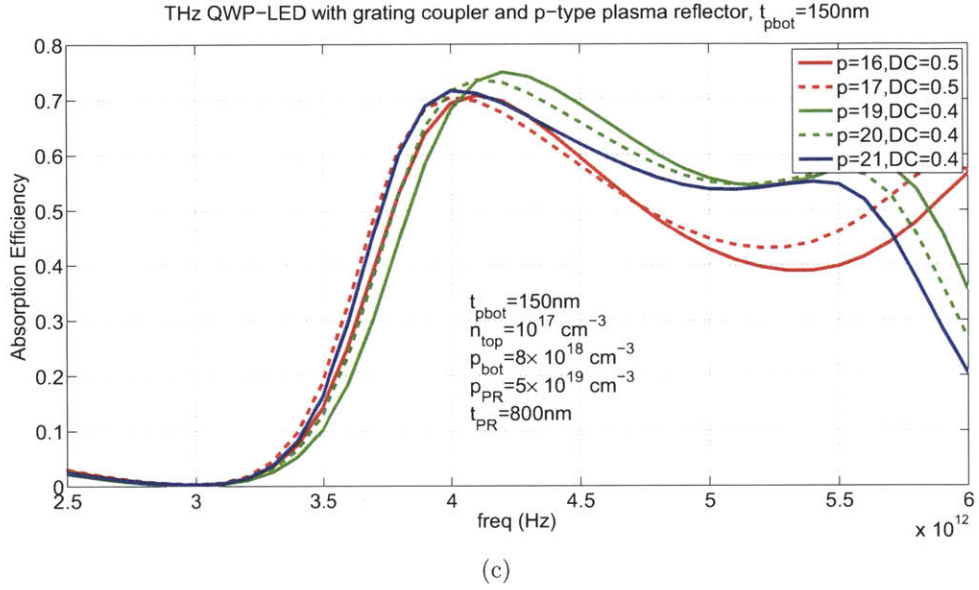


Figure 3-10: This figure shows the simulated absorption efficiency spectrum in THz QWP-LED with different p-type bottom contact layer thicknesses t_{pbot} . (a) $t_{pbot} = 50nm$. (b) $t_{pbot} = 100nm$. (c) $t_{pbot} = 150nm$. The other parameters are chosen as below. N-type contact layer doping concentration $n_{top} = 10^{17}cm^{-3}$. P-type bottom contact layer doping concentration $p_{bot} = 8 \times 10^{18}cm^{-3}$. P-type plasma reflector doping concentration $p_{PR} = 5 \times 10^{19}cm^{-3}$, thickness $t_{PR} = 800nm$. These parameters are shown in the plots. Each plot shows several curves with different grating coupler periods p and duty cycles DC and are in the legends. The unit of p is μm . The absorption efficiency peaks at approximately 4THz with a value exceeding 70%. Comparing (a),(b) and (c), it can be found that the absorption efficiency is not sensitive to the thickness of the p-type bottom contact layer t_{pbot} when it is varied from 50nm to 150nm.

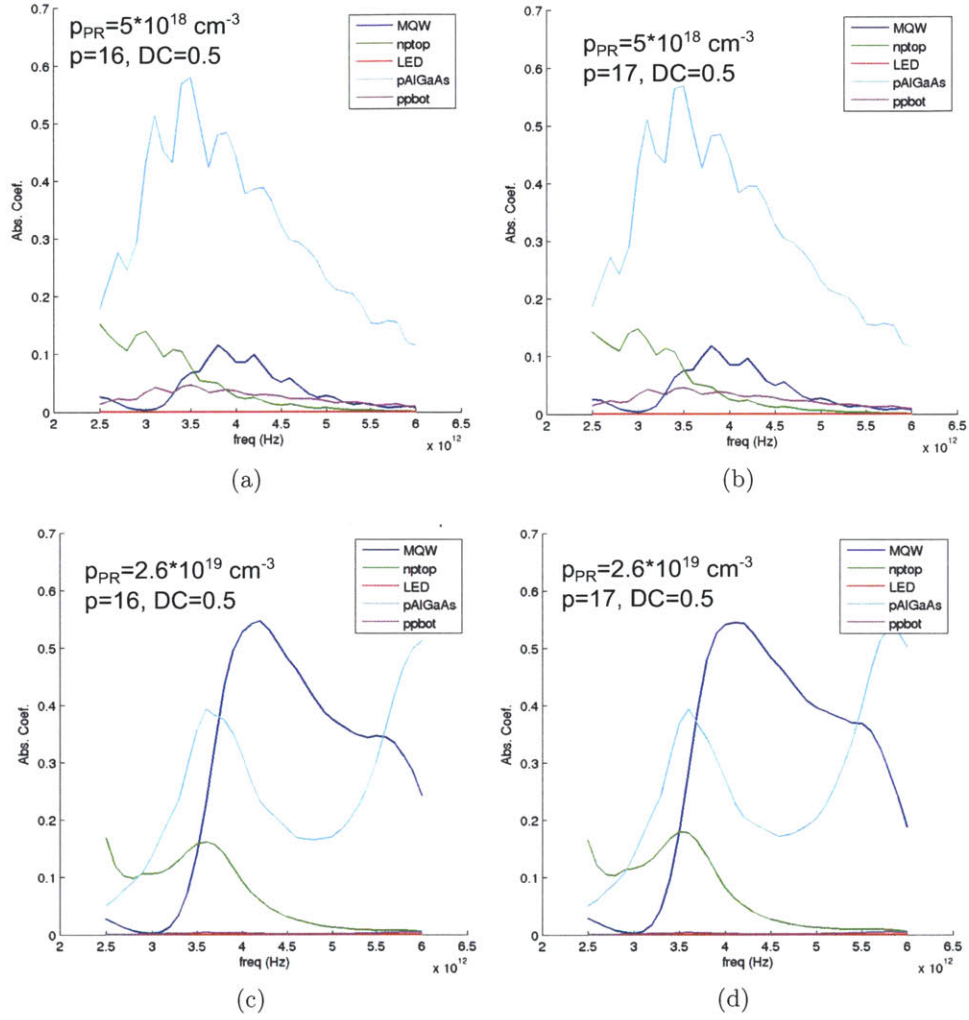


Figure 3-11: This figure shows the simulated absorption efficiency spectrum in THz QWP-LED with the p-type plasma reflector doping concentrations p_{PR} different from the optimized value $5 \times 10^{19} \text{ cm}^{-3}$. The doping values chosen to be shown here are $5 \times 10^{18} \text{ cm}^{-3}$ (in (a) and (b)) and $2.6 \times 10^{19} \text{ cm}^{-3}$ (in (c) and (d)). The other parameters are chosen to be the optimized values: n-type contact layer doping concentration $n_{\text{top}} = 10^{17} \text{ cm}^{-3}$; p-type bottom contact layer doping concentration $p_{\text{bot}} = 8 \times 10^{18} \text{ cm}^{-3}$; p-type bottom contact layer thicknesses $t_{p_{\text{bot}}} = 50 \text{ nm}$; p-type plasma reflector thickness $t_{PR} = 800 \text{ nm}$. Each plot shows several curves with absorption efficiencies in different regions of the THz QWP-LED structure and these notations are the same as in Fig. 3-9. Devices with different grating coupler periods p and duty cycles DC are also shown: (a) and (c) show $p = 16 \mu\text{m}$, $DC = 0.5$, (b) and (d) show $p = 17 \mu\text{m}$, $DC = 0.5$. The unit of p is μm .

Finally, the effect of the p-type plasma reflector thickness t_{PR} is discussed. Fig. 3-12 shows the simulated absorption efficiency spectrum in THz QWP-LED with the p-type plasma reflector thickness $t_{PR} = 400nm$, which is different from the optimized value $800nm$. The other parameters are chosen to be the optimized values. Each plot shows several curves with absorption efficiencies in different regions of the THz QWP-LED structure and these notations are the same as in Fig. 3-9. Devices with different grating coupler periods p and duty cycles DC are also shown: (a) shows $p = 16\mu m, DC = 0.5$, and (b) shows $p = 17\mu m, DC = 0.5$. The unit of p is μm . From the figure and comparing to Fig. 3-9, it can be seen that when t_{PR} is reduced from $800nm$ to $400nm$, absorption in MQW region is reduced, the peak absorption efficiency value reduced from 70% to 60%, while absorption in other regions are increased. The main competing absorption region with MQW is the p-type plasma reflector region. The THz absorption efficiency in plasma reflector is increased from approximately 20% to 40% as its thickness is reduced from $800nm$ to $400nm$. This is because a plasma reflector, essentially a heavily doped semiconductor, is also an absorbing layer due to its complex permittivity and complex refractive index. If the plasma reflector is not thick enough, the reflection property cannot perform very well. Therefore, rather than a light reflector, it serves as an absorber instead. Moreover, when the plasma reflector is very thin, the EM wave absorption in the plasma reflector layer may not be very high, but the reflectance from it is also small. In this condition, the reflectance of EM wave incident onto plasma reflector layer is more subjective to the layers below the plasma reflector. Thus, a plasma reflector should be thick enough to achieve good QWP-LED performance.

Another important issue in designing THz QWP-LED is how to couple out the LED emitted light from the high-refractive index GaAs material to low-index BCB, sapphire, and air. If the LED emitting surface is flat, the fraction of the light that can be emitted out from GaAs into air is at most [40]

$$\frac{1}{4n_{GaAs}^2} \approx \frac{1}{4(3.2)^2} = 2.5\% \quad (3.5)$$

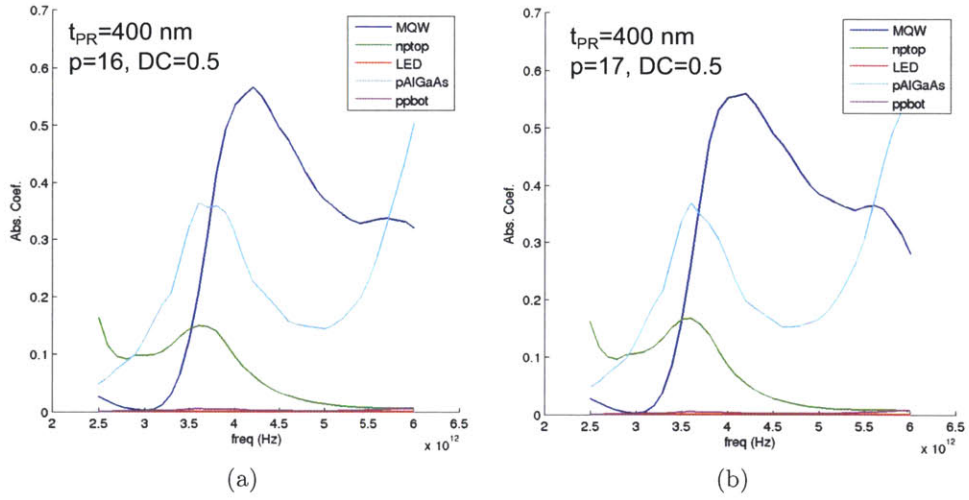


Figure 3-12: This figure shows the simulated absorption efficiency spectrum in THz QWP-LED with the p-type plasma reflector thickness $t_{PR} = 400nm$, which is different from the optimized value $800nm$. The other parameters are chosen to be the optimized values. Each plot shows several curves with absorption efficiencies in different regions of the THz QWP-LED structure and these notations are the same as in Fig. 3-9. Devices with different grating coupler periods p and duty cycles DC are also shown: (a) shows $p = 16\mu m$, $DC = 0.5$, and (b) shows $p = 17\mu m$, $DC = 0.5$. The unit of p is μm .

Thus, most of the light generated from LED cannot be emitted out, giving very small external quantum efficiency. To increase the external quantum efficiency, which is the product of internal quantum efficiency and extraction efficiency, either the internal quantum efficiency or the extraction efficiency should be increased. Since the THz QWP-LED operates at cryogenic temperature, little can be done to increase the internal quantum efficiency which is already very high. Therefore, several techniques are performed on the LED structure to increase the extraction efficiency of the THz QWP-LED, essentially GaAs LED. These techniques include photon recycling [41], resonant cavity LED [42, 43], microlensed LED [44], textured surface LED [41, 45], and 2D photonic crystal [40, 46, 47].

While the other techniques appear only up to 30% extraction efficiency, 2D photonic crystal shows considerable enhancement of light extraction for LED. A record high 73% has been achieved with III-Nitride LED using photonic crystal technique [48]. In GaAs-based LED, 2D photonic crystal claims to have at least 6 times enhancement in light extraction [40].

In this project, an initial exploration was performed to use 2D photonic crystal structure to increase the light extraction efficiency for the LED light generated from QWP-LED structure. The calculation tools that were used are FEM simulation with commercial software COMSOL, and FDTD (Finite Different Time Domain) [49] calculation with the softwares mpd and meep developed in MIT [50]. Some initial trials used the simple square-lattice hole on top of the LED surface. Without parameter optimization, the simple 2D photonic structure already shows more than two folds enhancement of light extraction efficiency. Due to the limitation of actual implementation of this THz QWP-LED, this work is to be done by the time the p-type MBE growth is available.

As a concluding remark for the design of THz QWP and THz QWP-LED grating coupler and plasma reflector, thorough and detailed electromagnetic FEM simulation is performed to achieve highest absorption in MQW region (QWP active region) in the vicinity of 4THz radiation. Several metal grating periods and duty cycles can obtain good performance. To further improve light absorption in MQW, a plasma

reflector layer is introduced in the structure. While it is easy to implement n-type plasma reflector in THz QWP, the design of p-type plasma reflector in THz QWP-LED needs more careful consideration. The choice of our good n-type plasma reflector is a $400nm$ thick GaAs with Si doping at $10^{17}cm^{-3}$. It serves as the n-type contact layer of the THz QWP as well. The good p-type plasma reflector in our structure requires an $800nm$ thick $Al_{0.1}Ga_{0.9}As$ with C doping at $5 \times 10^{19}cm^{-3}$ and a $50nm$ thick GaAs with C doping at $8 \times 10^{18}cm^{-3}$. The latter also serves as the p-type contact layer in the THz QWP-LED device.

Chapter 4

Fabrication of QWP

The basic fabrication steps follow the processing of GaAs materials and some are similar as the processing of THz Quantum Cascade Laser (QCL) [51]. However, due to the special structure and requirement of THz QWP, such as the 45° facet and grating coupler structure, some special steps are developed to cater the need. In the following sections, fabrication of three kinds of devices (45° QWP, Grating Coupler QWP and QWP-LED) are described in detail.

The designed MQW structure will be implemented by MBE (molecular-beam epitaxy) growth. This is performed by Dr. John Reno at Sandia National Laboratories. They are characterized by X-ray diffraction. The initial MBE wafers are composed of GaAs substrate and MQW structures on top of the substrate. The target devices should have mesas of $300\mu m \times 300\mu m$, and metal contact layers on both terminals.

4.1 Fabrication of 45° QWP

The starting MBE wafer is an SI GaAs substrate with MQW structure on top. The first step is to cleave the MBE wafer into roughly $1cm \times 1cm$ pieces. The following steps are dealing with the pieces, and Fig. 4-1 shows the flow chart of the processing steps of this 45° THz QWP.

After cleaving pieces, the deposition of the bonding pad oxide is processed. One piece will have several mesas on top, and one facet of the piece needs to be lapped

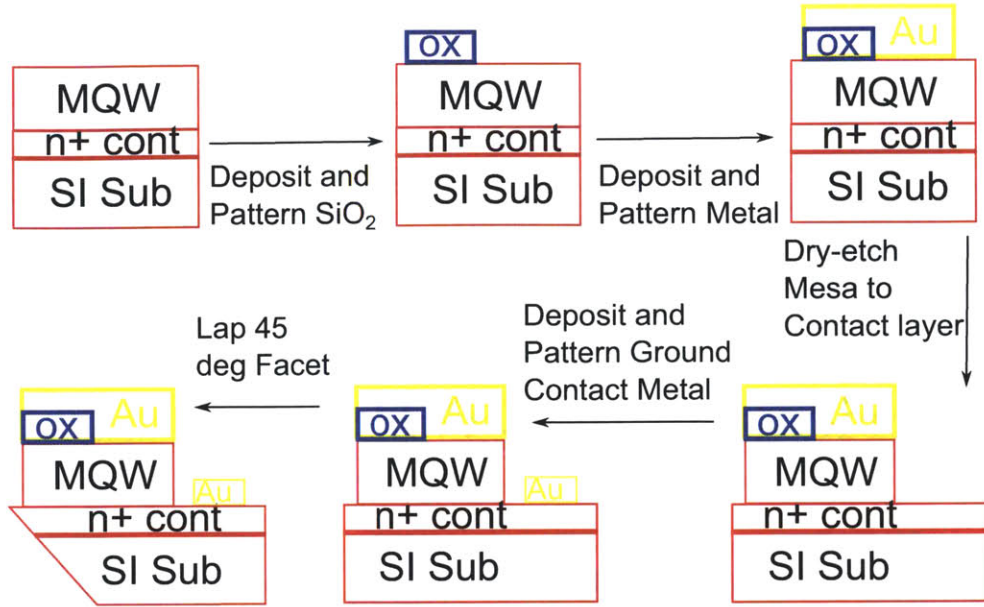


Figure 4-1: The flow chart of the processing steps of 45° THz QWP.

45°. Due to the layout of the mesa, distance for wire bonding, and difficulty in wirebonding on top of 45° facet, a gold/oxide bonding pad should be used. The bonding pad is covered with oxide and gold. In this step, STSCVD is used to deposit 2000Å thick SiO₂. The thickness of the oxide layer is chosen to make sure it does not breakdown during device operation when current is flowing from the top contact to the ground contact. Because of the low current of QWP during operation, this oxide layer does not need to be very thick. Then, photolithography is performed using positive photoresist and G-Line exposure. BOE etch is the following step to pattern the oxide layer. Then the photoresist is removed using acetone.

Next, QWP top contact layers are made. This is through lift-off process in GaAs [52]. By photolithography with image-reversal photoresist, the QWP surface part that needs to be deposited with gold metal is not covered with photoresist while the rest is. Due to the negative slope left from image-reversal photoresist, metal contact can be made through e-Beam deposition. The photoresist together with the metal on top of it, can be lifted off by soaking the piece in acetone. The metal contact is Ti/Au with the thickness of 200/3000Å. Gold is used because of its low loss and compatibility with wire bonding, and Titanium is to increase the bonding strength

between gold and GaAs. Notice that none of the contacts made in the QWPs are annealed.

After the contact layer deposition, the device mesa is made using dry-etch with inductively conductive plasma (ICP). The etchant is $\text{Cl}_2 : \text{SiCl}_4 : \text{Ar}$ plasma in this case. The dry-etch mask is the metal contact layer and the resulting mesa height is between $3.01\mu\text{m}$ to $3.81\mu\text{m}$. The mesa height is important because the heavily doped n-contact layer between the substrate and MQW active regions should be exposed in order to deposit metal contact on it. The mesa height is characterized using the non-contact profilometer. Due to the fluctuation of dry-etch rate and uncertainty of the profilometer, the mesa height does not need to be very accurate as long as it is in the acceptable range. This is also the reason that we need to use a relatively thick n+ contact layer, which is 800nm in our design.

The following step is to make ground contact on the substrate surface. This is similar to the deposition of top contact layer: use image-reversal photolithography to define the contact region, then metal deposition and lift-off. However, special attention should be made to the coating of photoresist when doing photolithography. Since the mesa can be as high as $3.81\mu\text{m}$, one needs to make sure the photoresist cover such a high step and the edge of the step is not exposed to air. Since a typical photoresist thickness is $1 - 2\mu\text{m}$ with a normal spin speed (4000 rpm), a much lower spin speed needs to be used, and multiple coatings should be performed. In order to prevent the accumulation of edge bead and backside coating of the photoresist, after one spin, the edge bead and backside photoresist needs to be cleaned before the second spin is performed. In the case of fabricating this THz QWP, a spin speed of 2000 rpm and 3 times repeating works well for the later photolithography and deposition. After the photoresist is developed, there should be photoresist fully covering the surface of the piece except for the area that should have ground contact metal deposited. Fig. 4-2 shows the photo of the device surface after this layer of photoresist is developed. The areas of mesa (covered with metal), n+ contact layer surface covered with photoresist (on the ground of the device) and n+ contact layer surface without photoresist (on the ground of the device) are annotated. By inspecting the edge of the mesa step

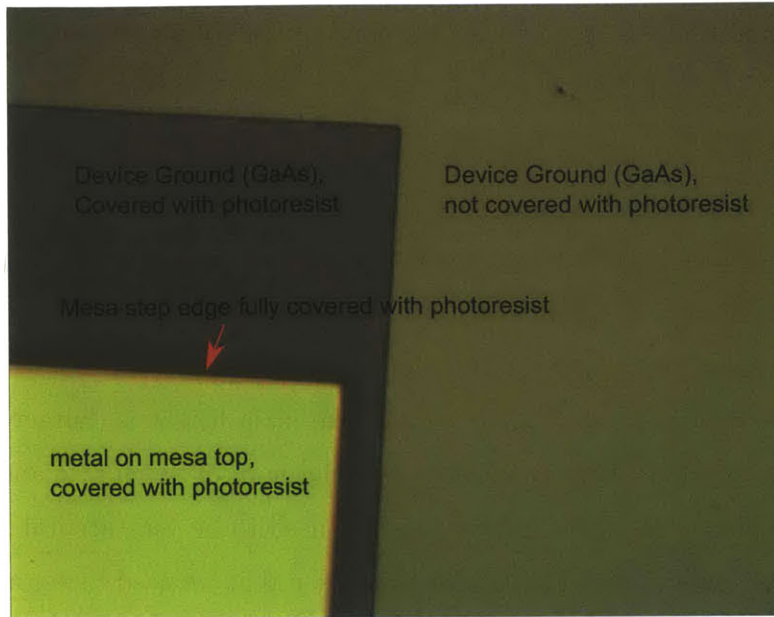


Figure 4-2: Photo of the device surface after this layer of photoresist is developed. The areas of mesa (covered with metal), n+ contact layer surface covered with photoresist (on the ground of the device) and n+ contact layer surface without photoresist (on the ground of the device) are annotated. By inspecting the edge of the mesa step edge, blurring and with some red-ish stripes occur. This means this area is covered with photoresist. The red-ish stripes can also be observed in the ground covered with photoresist on top.

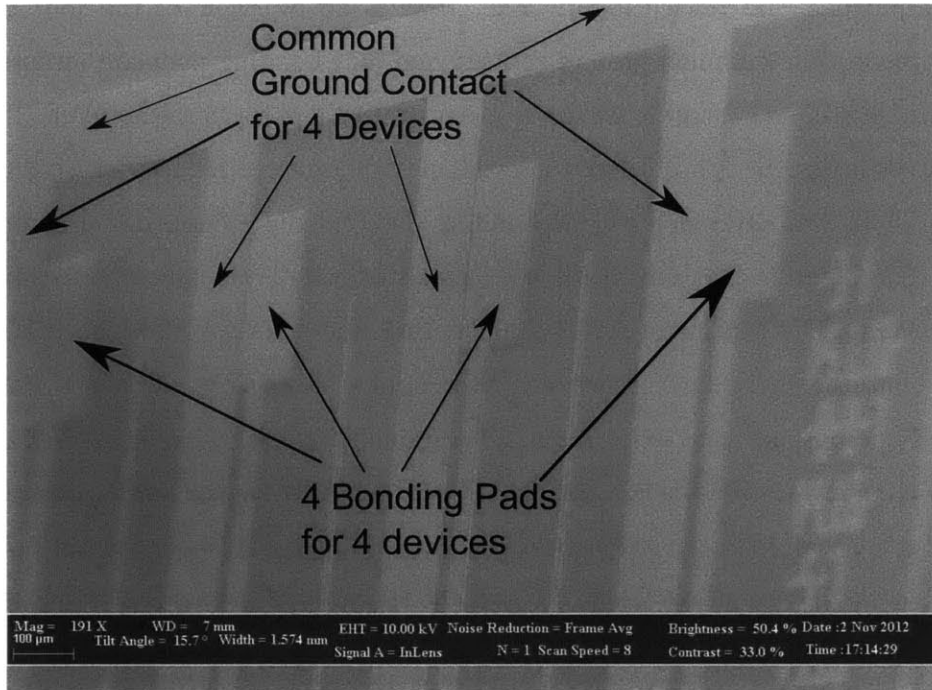
edge, blurring and some red-ish stripes occur. This means this area is covered with photoresist. More reliable proof can be performed using fluoroscope, which generates fluorescent glow of the sample. Because photoresist is organic material, it appears red under the fluoroscope, while other inorganic semiconductor part appears black. Under the fluoroscope, the whole area of the QWP sample except for ground contact region is red. Especially, on the step edge of the mesa, red photoresist can be observed. This confirms the good coverage of photoresist on the mesa step over $3\mu m$ -high. The red-ish stripes can also be observed in the ground covered with photoresist on top. This, again, confirms that the modification of the coating process is effective.

Fig. 4-3 shows the SEM image of the 45° QWP after all the fabrication steps except for the last 45° facet lapping. Four devices are fabricated on one MBE piece. Common ground contact for all four devices is used, and each device has separate

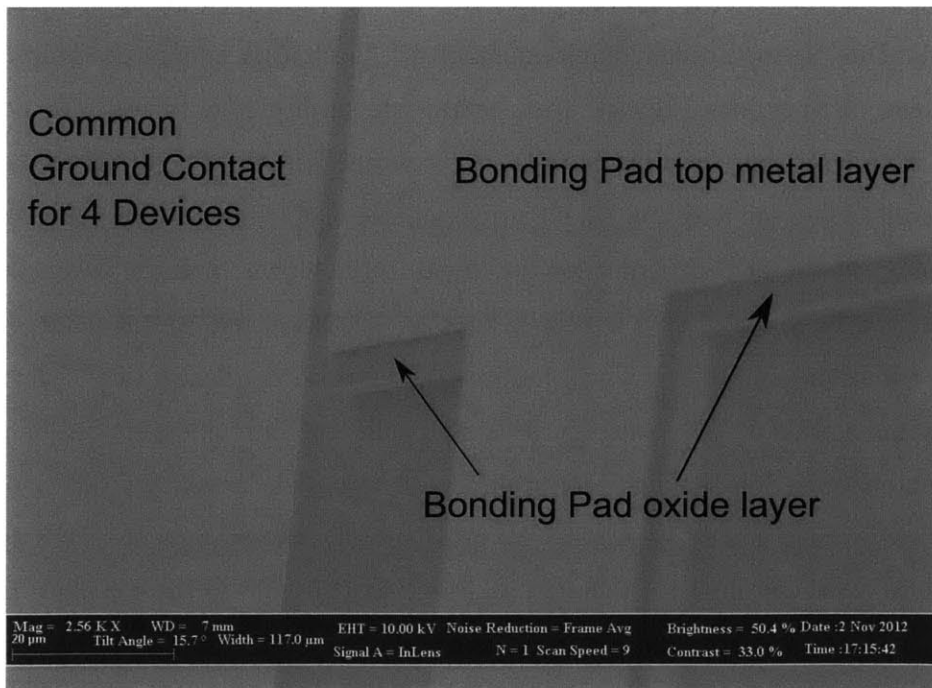
bonding pad and device mesa. Fig. 4-3a is an overview of the four devices on the piece. The common ground contact and four bonding pads are annotated. The common ground contact is for the stable operation and less noise of QWP. The ground contact is designed to be close to device mesa in order to reduce parasitic resistance. Fig. 4-3b is a close view of one bonding pad and the ground metal contact beside it. The bonding pad top metal layer and the oxide layer beneath it can also be observed. The top metal size is smaller than the oxide layer, which is desired and prevents the short current between two contact layers. Fig. 4-3c is a close look at the bonding pad and device mesa. The ground contact, bonding pad (including its top metal layer, oxide layer, and GaAs layer beneath), device mesa (including its top metal layer and GaAs layer beneath) are annotated. The step between bonding pad region and device mesa region indicates the thickness of the oxide layer of the bonding pad.

The last step is the lapping of 45° facet of the device. This is done using a lapping tool. Due to the special requirement of 45° facet, this lapping is done in a tilted surface, in very small device area, and needs surface smoothness. To address the 45° lapping rather than flat surface, a 45° wedge is used. The MBE piece is further cleaved into a smaller one which suits the size of the wedge. Two screws are used to support the piece in order for the device to be higher than the wedge so that the facet can be lapped. This bundle is bonded together using crystal bond. Because of the tilted and small area which induces the extreme fragileness of the device during lapping, a good crystal bond is critical and sufficient carefulness should be performed when handling this bundle. The lapping speed should be small, and device orientation during lapping should be taken care of. Typically, the movement of the sand paper relative to the lapped facet should go from the 135° side to the 45° side. In order to get a THz-grade smoothness, a fine sand paper is used, this also reduces the risk of device fracture.

The following procedure before having the device ready for measurement is wire bonding to the device mount. This will be discussed in Chapter 5.



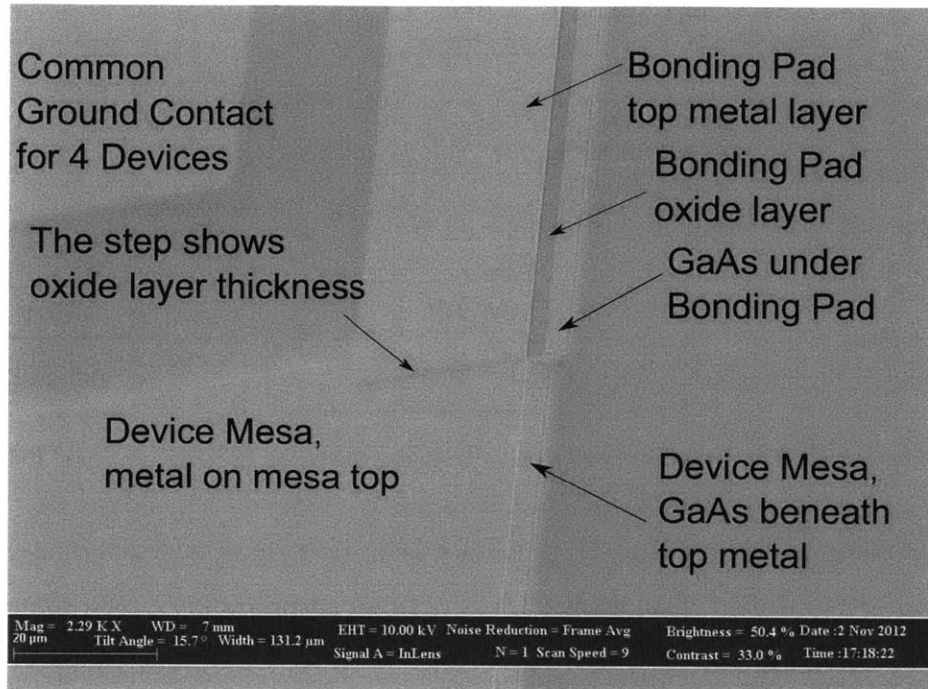
(a)



(b)

(Continue to next page)

(Continued from last page)



(c)

Figure 4-3: This figure shows the SEM image of the 45° QWP after all the fabrication steps except for the last 45° facet lapping. Four devices are fabricated on one MBE piece. Common ground contact for all four devices is used, and each device has separate bonding pad and device mesa. (a) An overview of the four devices on the piece. (b) A close view of one bonding pad and the ground metal contact beside it. (c) A close look at the bonding pad and device mesa.

4.2 Fabrication Steps of Grating Coupler QWP

Unlike the 45° QWP, the grating coupler QWP has an n^+ GaAs substrate. Despite this, the first step is still to cleave the MBE wafer into roughly $1\text{cm} \times 1\text{cm}$ pieces. The following steps are described below and the flow chart of the processing steps is shown in Fig. 4-4.

After cleaving pieces, as in 45° QWP, the deposition of the bonding pad oxide is processed. The use of bonding pad for the grating coupler QWP is that the incident THz light should not be disturbed by the wire bonding later put on the device. If

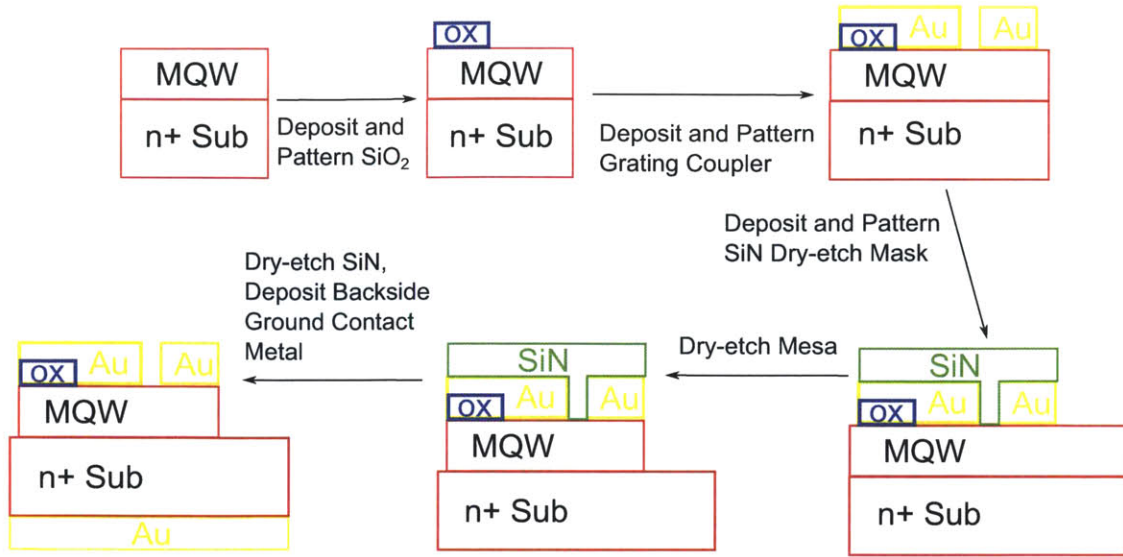


Figure 4-4: The flow chart of the processing steps of grating coupler THz QWP.

no bonding pad is used, the top contact layer must have wire bonding, which will diffract the incident THz wave. The bonding pad procedure is the same as in 45° QWP. 2000Å thick SiO₂ is deposited.

The next step is to make grating coupler on top of the device. Still, this step is similar to making top contact in 45° QWP: image-reversal photolithography, then e-beam deposition followed by acetone lift-off.

The step following defining of grating coupler is unique in the grating coupler QWP. This is to define the mesa on the front side. To etch mesa on this piece, the top metal contact can no longer be used as dry-etch mask, because it is metal strips which locate on top of the mesa. Therefore, considering the etch selection between GaAs, photoresist and other materials, SiN is selected in this case as a dry-etch mask [52]. So 3000Å SiN is deposited on top of the device through CVD. Positive photolithography is then used to define the areas of the mesa. The areas of the mesas are covered with positive photoresist, while the other parts have SiN exposed to air. Then ECR (electron-cyclotron resonance) dry-etch is used to etch away the exposed SiN layer. In this step, CF₄/H₂ plasma is the etchant and has good etch selectivity between SiN and Shipley 1813, the positive photoresist used in the fabrication. After patterning SiN mask, the photoresist on top of SiN can be removed by acetone. Fig.

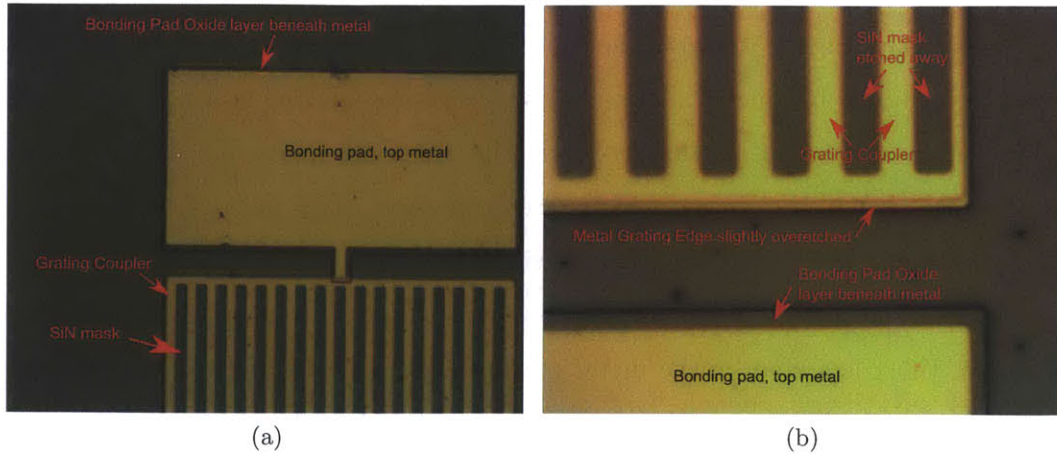


Figure 4-5: (a) shows the top view of one grating coupler THz QWP at the end of SiN mask patterning. It can be seen that SiN covers the mesa area quite well. (b) shows the top view after mesa etch and SiN mask removal. Compared with (a), the green SiN mask on top of the grating coupler and device mesa are etched away. The color in between the metal gratings and the color outside the device mesa and bonding pad are the same, which confirms the complete etch-away of SiN mask.

4-5a shows the top view of one device at the end of this step. The bonding pad (including top metal and oxide layer beneath), grating coupler on top of the mesa, and SiN mask on top of the grating coupler and device mesa are shown. The bonding pad oxide layer is slightly larger than the bonding pad metal, which prevents the short current between two terminals of the device. The SiN appears to be green, which is the property of 3000\AA thick SiN layer. It can be seen that SiN covers the mesa area quite well. The edge of the mesa lacks very narrow strips of SiN, but since this area is covered with metal, which also serves as a dry-etch mask, so this does not cause a problem during later processing.

Given the SiN dry-etch mask, the next step is to dry-etch mesa. As in 45° QWP mesa dry-etch, this step is also performed in ICP dry-etch with the same etchant. The etch height should be between $3.01\mu\text{m}$ and $3.61\mu\text{m}$ in this grating coupler QWP. The reason is the same as in 45° QWP. However, since the ground contact is made at the bottom of the device attaching the n+ GaAs substrate, the mesa height does not appear to be critical. Then, ECR dry-etch is employed again to etch away the SiN mask on top of the mesa. The recipe is the same as above. Slight overetch of

the SiN mask is not problematic, because the etchant CF_4/H_2 does not etch gold or GaAs easily. Fig. 4-5b shows the top view after this step. In the figure, The bonding pad (including top metal and oxide layer beneath) and the grating coupler on top of the mesa are shown. Compared with Fig. 4-5a, the green SiN mask on top of the grating coupler and device mesa are etched away. The color in between the metal gratings and the color outside the device mesa and bonding pad are the same, which confirms the complete etch-away of SiN mask. Notice that on the edge of the device mesa, there is a step on the metal grating. This may be due to the slight over-etch of the metal edge during the dry-etch steps. But this does not cause a problem for the QWP operation.

Fig. 4-6 shows the SEM image of the grating coupler QWP after the aforementioned processing steps. Fig. 4-6a is a close look at one edge of the device mesa and bonding pad. The grating coupler, mesa sidewall, bonding pad (including top metal, oxide, and GaAs sidewall) are shown. The line on the edge of grating coupler shows the metal grating edge slight overetch mentioned above. There also appears to be some GaAs ground grass. Fig. 4-6b is a close look at one edge of the device mesa. The device mesa, including sidewall and grating coupler, is shown. GaAs ground grass also appears. The steps on the edge of grating coupler shows the possible overetch of metal, or slight misalignment of the masks during lithography. Since this area is small and on the edge, it should not cause a problem. The GaAs ground grass may be due to the bombardment during dry-etch. Although this does not cause trouble for the device operation, it can be removed by dipping the device into 1 : 1HCl : H_2O solution for a few seconds. This is basically to use acid to etch away small amount of GaAs tips. A more effective method to remove the ground grass is to dip the piece in H_2O_2 for a few seconds first and then use 1 : 1HCl : H_2O . The employment of H_2O_2 is to slightly oxidize GaAs first, which makes it easy to etch it away using acid. This is applicable to small tips of GaAs since their surface area is large compared to bulk volume. Therefore, the method is not effective to GaAs surface on the bulk material, which is ideal in our case.

The last step is depositing metal on the bottom of the piece to form ground

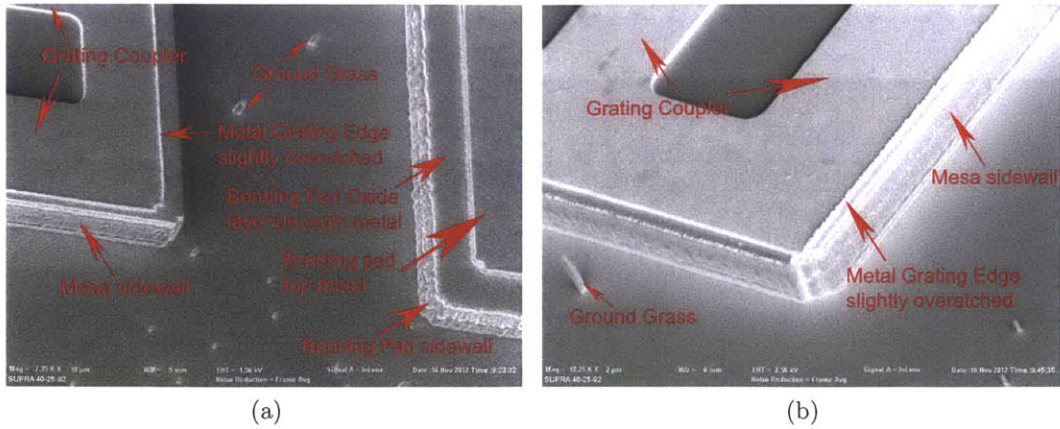


Figure 4-6: The figure shows the SEM image of the grating coupler QWP after the aforementioned processing steps. (a) A close look at one edge of the device mesa and bonding pad. The line on the edge of grating coupler shows the metal grating edge slight overetch mentioned above. There also appears to be some GaAs ground grass. (b) A close look at one edge of the device mesa.

contact. This is done through e-beam deposition and the metal composite is still $200/3000\text{\AA}$ Ti/Au. Because the deposition is on the bottom of the substrate, in order to protect the front side structures, a clean receptacle wafer covered with gold should be placed between the QWP piece front side and the e-beam machine.

4.3 Fabrication Steps of QWP-LED

The fabrication of THz QWP-LED is somewhat different from the fabrication as THz QWP. Due to the target structure shown in Fig. 1-10b, the fabrication processes for THz QWP-LED are designed as described below. Although the processes have not been implemented on actual MBE wafers, they have been well planned and tested.

The starting material is the MBE wafer which has layers of SI GaAs substrate, etch-stopper layer ($0.4\ \mu\text{m}$ thick undoped $\text{Al}_{0.55}\text{Ga}_{0.45}\text{As}$), $n+$ contact layer, QWP layers, LED layers, $p+$ contact layer, from bottom to top in order. A sapphire wafer is also needed. BCB (DOW Cyclotene 3000 [53]), the bonding material, together with its adhesion promoter AP3000 [54] is required as well. The outgassing of cured (step described below) BCB and AP3000 is small enough that they do not cause the

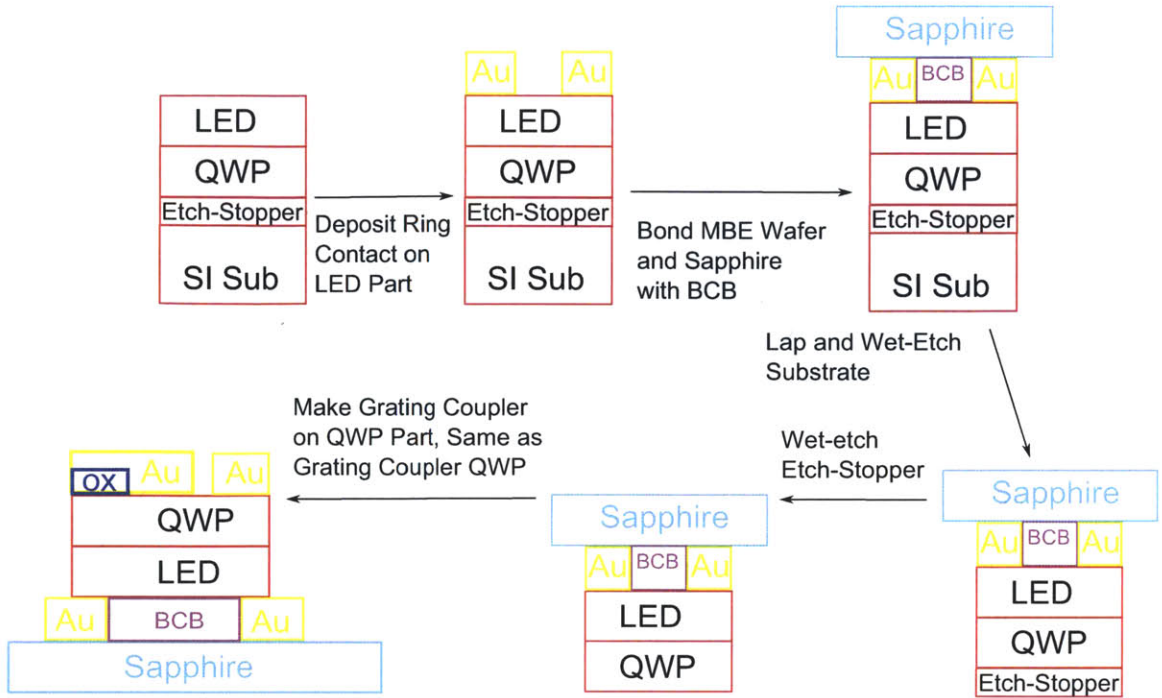


Figure 4-7: The flow chart of the processing steps of grating coupler THz QWP-LED.

malfunction of the other instruments such as CVD and dry-etch machine. Therefore the use of BCB and AP3000 is very safe and reliable.

Same as the other two devices, the initial step is also to cleave the MBE wafer into $1\text{cm} \times 1\text{cm}$ pieces and the sapphire wafer into $1.5\text{cm} \times 1.5\text{cm}$ pieces. The following steps are described below and the flow chart of the processing steps is shown in Fig. 4-7.

Then LED ring contact is made. Since LED layers are on top surface of the MBE piece, it is reasonable to make LED's contact first. The ring contact of LED is a metal contact surrounding the mesa top of the QWP-LED device. The reason of the ring contact is to allow as much NIR light as possible to emit out. Except for the metal contact shape, this step is the same as defining other contact layers in QWP devices.

After this step, MBE piece should be bonded to the NIR-transparent sapphire piece [55]. To do this, the sapphire piece and MBE piece should be surface-cleaned in asher. Then, AP3000 is spinned on sapphire and the LED side of the MBE piece, using

a coater. A typical spin rate of 3000rpm for 15 seconds results in approximately 10\AA thick AP3000 after the soft bake, which takes place on a hot plate at the temperature of 150°C for 1 minute. With the adhesion promotor on both pieces, BCB is spinned on both sides: the LED side of the MBE piece and the sapphire piece, where there is AP3000 already. 2500rpm is used, and it gives approximately $1.43\mu\text{m}$ thick BCB layer after cure, which will be described later. After coating BCB, softbake is performed on a hot plate at 115°C for 2 minutes. Then the actual bonding of the two pieces is performed. In this step, MBE piece and sapphire piece are stacked together, the sides with BCB touching each other. Bonding pressure should be approximately $2\text{kg}/\text{cm}^2$. In order to achieve such a large pressure, an Aluminum mount with screws to adjust pressure is used. The two-piece stack is put inside the narrow slit inside the mount, and screws can be tighten to apply pressure to the pieces inside the slit. In order to avoid the possible piece fracture caused by uneven surface of the slit, two pieces of graphite are used to sandwich the pieces in. Then, the graphite-MBE piece-sapphire piece-graphite four-layer stack is put inside the slit of the mount. Screws are tighten in an order that the top panel of the mount is moving horizontally, ensuring almost uniform pressure on the surface of the piece-stack. The mount is then put into a temperature-adjustable N_2 oven. Soft curing the pieces in the oven at 280°C for 2 hours purged with N_2 , to prevent the oxidation of the BCB and AP3000. Then ramp up the temperature of the oven and hard cure the piece at 330°C for 1 hour. After curing, BCB and AP3000 become physically and chemically stable and they do not outgas at the temperature below 330°C .

After this step, the MBE-sapphire piece-bundle is taken out and lapping is performed to remove most of the GaAs substrate of the MBE piece. Details are similar to that in [51].

After lapping, in order to remove the rest of the GaAs substrate and etch-stopper layer to expose the QWP layers, backside etching is performed using selective wet-etch [51]. First, ultrasonic solvent clean is performed to thoroughly clean the lapped pieces. Then, wet-etch the remaining GaAs substrate with 3 : 1 Citric Acid : H_2O_2 solution. Since this solution does not etch $\text{Al}_x\text{Ga}_{1-x}\text{As}$ when Aluminum fraction is

decent, the etch will stop at the etch stopper layer. Then, the piece is placed in HF for 30 seconds. HF etches $\text{Al}_x\text{Ga}_{1-x}\text{As}$ but not GaAs, so etch-stopper layer is removed in this step. Now the QWP layer is exposed and processing can be performed on the QWP side of the piece-bundle.

The rest of the steps are similar as in THz grating coupler QWP: pattern bonding pad oxide, make metal gratings, define mesa and deposit mesa dry-etch mask SiN, and finally dry-etch mesa.

Several differences occur compared to THz grating coupler QWP. First, during the lithography on the QWP side of the piece, double-side lithography should be used in order to match the QWP-side pattern with the LED-side pattern. Second, when dry-etching mesa, etching should be performed all the way down to the metal ring contact layer on the LED side. Also, the mesa size on the QWP side should be somewhat smaller than the size defined by the ring-contact of LED layer, because the metal contact layer should be exposed in order to wire bond to electrode and apply bias. Besides, unlike the final step of the backside metal deposition in the grating coupler QWP, in QWP-LED, no backside metal deposition is needed, because LED ring contact serves as another metal contact.

Besides the process of THz QWP-LED described above, some more steps can be added before or after the definition of LED ring contact: modifying the LED surface to increase extraction efficiency of the LED NIR radiation. If 2D photonic crystal technique is used, ebeam lithography or interference lithography can be used to pattern the 2D photonic crystal on the surface of the LED. Due to the short wavelength of NIR light in GaAs (on the order of 100nm), ebeam lithography, rather than the conventional optical lithography is used to achieve desired resolution. However, due to the slow yield of ebeam lithography, interference lithography can be used as well on the condition that the designed 2D photonic crystal is periodic all over the surface.

Chapter 5

Device Characterization

In this chapter, the characterization of the THz QWP is presented. In Chapter 5.1, a detailed discussion on measurement system build-up is shown. Because the operation of the THz QWP requires cryogenic (liquid Helium temperature) and low-noise environment, such a measurement system needs to be built up, and both features are discussed separately. The later part of this chapter presents the measurement results of THz QWPs.

5.1 Measurement System Build-up

As mentioned above, THz QWP requires cryogenic (liquid Helium temperature) and low-noise environment during its operation. A liquid-helium cryogenic dewar is used to place the device and hold cryogenic temperature for a considerable amount of time (typically 6-7 hours). Meanwhile, the wires attach to the device electrodes and terminals on the outlet of the dewar, connecting to external electronic measurement system. The wires need to be selected and the layout of them should be designed with care in order to cater the needs of cryogenic and low-noise measurement.

5.1.1 The Build-up of Cryogenic Dewar

The cryogenic LHE (liquid Helium) dewar is an open-cycle dewar from Infrared Laboratories Inc. Its inner structure is shown in Fig. 5-1. The actual size is not the same as the notation of the figure, but the rest are the same. The figure is from Infrared Laboratories Inc. In order to permit incoming THz radiation and emitted NIR light, and to make the dewar compatible for all the measurements of the 45° QWP, grating coupler QWP, 45° QWP-LED and grating coupler QWP-LED, three windows with 1.5" diameter are open on three facets of both the dewar case and radiation shield. A thin ($\sim 0.25\text{mm}$ – *thick*) PE (polyethylene) plastic piece is attached on the window of the dewar case, fixed with a flange and sealed with O-rings. A Si-diode temperature sensor is anchored on the LHE tank platform and connected to the outlet of the dewar. 8 pairs of NiCr wires were also attached between the platform and the dewar outlet. The NiCr wires are for electrical connection and each of them is approximately 30cm long. NiCr wires were used because NiCr has low thermal conductivity ($0.25\text{W}/(\text{m} \cdot \text{K})$, [56]) and good electrical conductivity. Compared to other widely-used cryogenic wires, NiCr has lower thermal conductivity at 4K (Phosphor bronze $1.6\text{W}/(\text{m} \cdot \text{K})$ and Maganin $0.5\text{W}/(\text{m} \cdot \text{K})$). The use of PE plastic is because it has good transmission for THz wave. For 2mm-thick PE sample, the transmission at wavelength of $75\mu\text{m}$ (corresponding to 4THz) is approximately 74% (data obtained from Tydex Optics), then for 0.25mm-thick PE piece, the $75\mu\text{m}$ THz wave transmission is

$$Trans = 74\% \times e^{0.25/2} \approx 84\% \quad (5.1)$$

This 84% is satisfactory for our case.

At the time this dewar is being used for this project, its cryogenic feature does not function—the liquid Helium hold time is almost none, and liquid Nitrogen hold time is only a few hours. Therefore, a repair work for the cryogenic dewar is necessary before any measurement can be performed. This section will deal with the solution to maintain long liquid Helium temperature hold time.

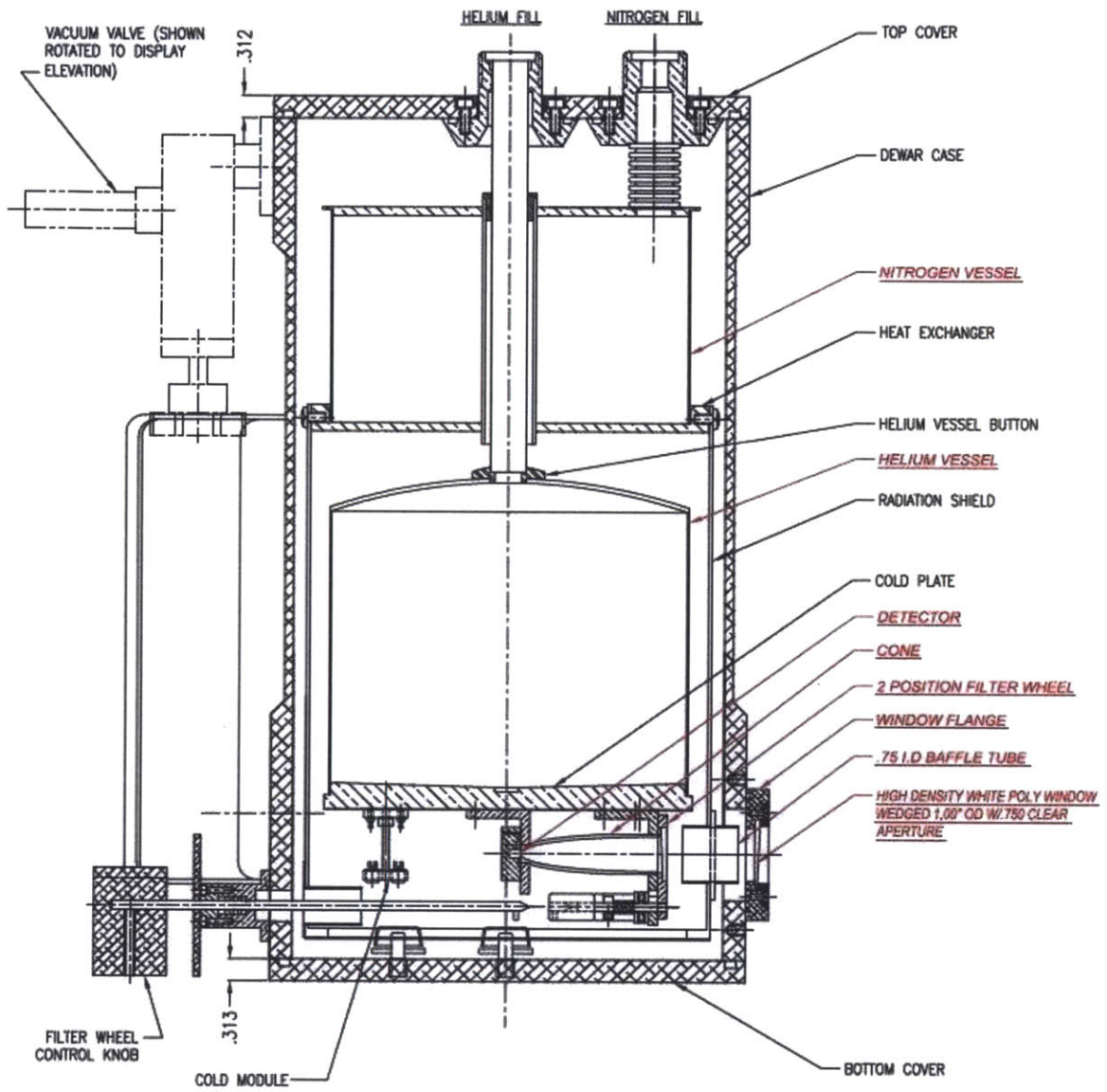


Figure 5-1: The layout of the LHE dewar used in the experiment. The actual size is not the same as the notation of the figure, but the rest are the same. The figure is from Infrared Laboratories Inc. Three windows with 1.5" diameter are open on three facets of both the dewar case and radiation shield [57].

The reason for the short hold time may be either vacuum leakage, or heat leakage, or both.

To check whether vacuum is good, we can examine the time it takes for the dewar to pump down. During the first pumping trial, the dewar could only be pumped from atmospheric pressure (about 1013.25 mbar) to 1.5×10^{-4} mbar and the pressure did not go down further. This means there may be vacuum leakage somewhere in the dewar. Further checking all the O-rings and screws as well as cleaning the inner parts of the dewar made the vacuum performance better. To pinpoint the spot where the vacuum leakage occurs, one can use IPA (isopropanol) to squeeze at any suspected position. If vapor appears when squeezing, this means the pressure inside the dewar increases and this position has vacuum leakage. The dewar pressure could be decreased to the magnitude of 10^{-5} mbar, rather than stagnating at 1.5×10^{-4} mbar.

Since it has been a long time that the dewar has not been pumped down, several cycles of pumping were performed before further examination. This is to roughly clean the inner chamber of the dewar. Through these initial trials, the pumping time for the dewar pressure to reduce from atmospheric pressure (about 1013.25 mbar) to 7×10^{-5} mbar was decreased from 7 hours to less than 1 hour. After filling in liquid N_2 (LN2), the hold time at 77K is only 10 hours (see Fig. 5-2 curve 1). However, after filling in liquid N_2 and liquid He, the dewar could not cool down to 4K, rather, the temperature started at 38K, and after only 1 hour 40 minutes, the liquid N_2 was running out and the temperature began to increase rapidly (see Fig. 5-2 curve 2).

Then in order to check whether there are some problems with the vacuum of the dewar, a test is made that fill in liquid N_2 and keep pumping the dewar during the period that the temperature is recorded. As can be seen in Fig. 5-2 curve 3, the temperature of the dewar was maintained at liquid N_2 temperature (77K) for more than 30 hours, which is comparable with the new model of LHE dewar from Infrared Laboratories Inc. The phenomenon that keeping pumping increases the cryogenic hold time dramatically suggests that there may be outgassing somewhere inside the dewar. One suspicious outgassing spot was the possible machine oil on inner side

of the dewar case and the walls on the radiation shield. These large areas were covered with the old Aluminum foil, and the machine oil may be left there during the machining of the dewar windows. Thus, the old Aluminum foil was removed. As expected, there was a considerable amount of machine oil on the walls of the dewar. The outgassing of the machine oil is dramatic, and it was one of the reasons that worsen the dewar vacuum.

Therefore, the machine oil, as well as the double-side tape on the sidewalls of the dewar case and radiation shield, were cleaned with acetone and IPA. The double-side tape was used to tape the Aluminum foil on the sidewalls. Aluminum foil was used on the inner sidewall of the dewar case, because the dewar case is in thermal balance with the outside environment and is at 300K (room temperature). It keeps radiating heat to the radiation shield, which is in contact with the LN2 tank and maintains at 77K during normal operation. In order to maintain long LN2 hold time, the radiation from the dewar case to the radiation shield should be decreased as much as possible. According to Stefan-Boltzmann Law, the irradiance of a grey body is

$$j = \epsilon\sigma T^4 \quad (5.2)$$

in which

T is the temperature of the grey body.

j is the irradiance of a grey body, which means the total energy radiated per unit surface area of a grey body across all wavelengths per unit time.

ϵ is the emissivity of the grey body. It characterizes the ability that the grey body can emit the total energy. For blackbody, $\epsilon = 1$; for greybody, $\epsilon < 1$.

σ is the Stefan-Boltzmann constant, and its value is

$$\sigma = \frac{2\pi^5 k^4}{15c^2 h^3} = 5.67 \times 10^{-8} J s^{-1} m^{-2} K^{-4} \quad (5.3)$$

For the dewar problem, the only parameter that can be changed in order to reduce the radiation heat from dewar case to radiation shield, is to reduce the emissivity ϵ by choosing a material with low emissivity. Aluminum foil has a very low emissivity

of 0.1 at the wavelength of $10\mu m$, which is the wavelength at peak radiation flux at 300K. So Aluminum foil is usually used in the inner sidewall of the case of the dewar for good hold time, the same reason goes with the use of Aluminum foil on the inner sidewall of the radiation shield, because the radiation from the 77K radiation shield to the 4.2K LHE tank should be reduced as well. Aluminum foil is also used on the outer sidewall of the radiation shield and LHE tank, because the smooth and shining surface of Aluminum foil is able to reflect the EM radiation from the dewar case and radiation shield.

After removing all the old Aluminum foil and tapes, thoroughly cleaning the inside of the dewar, an LN2 temperature test was performed again, and the temperature vs. time curve is shown in Fig. 5-2 curve 4. Compared to curve 1, not much improvement had been made – the LN2 hold time was also approximately 10 hours. A further test was made to fill in LN2 and LHE. As can be seen in Fig. 5-2 curve 5, the dewar could be cooled down to 4.2K, the liquid Helium temperature. However, the LHE hold time was still very short, only slightly more than an hour.

With the suspicion that there were still vacuum issues existing, the test was performed again to fill in LHE and LN2 with pumping. The result is shown in Fig. 5-2 curve 6. Comparing curve 6 and curve 5, it is found that the LHE temperature hold time were similar, about 1 hour, but keep pumping made the temperature rising much slower than without pumping. This result suggested that there may be still some vacuum issues, while heat leakage might also exist, and the latter might be a major problem to prevent a long LHE hold time.

So it was time to solve the heat leakage problem. Since all the Aluminum foil was removed, this might be a major reason for heat leakage. Therefore, new Aluminum foil was applied on all the surfaces: inner sidewall of dewar case, both sides of radiation shield, outer sidewalls of both LHE tank and LN2 tank, and the inner side of dewar cover. A low-outgassing double-side tape was used to attach Aluminum foil. Besides, the new Aluminum foil was also made to cover all the windows on the dewar case and the radiation shield as well, because the windows might also be a major heat leakage pathway from the outside environment into the dewar. Although uncertainty existed

whether the windows have heat leakage or vacuum leakage, covering the windows with Aluminum foil could at least tell whether window heat leakage was a major problem. Moreover, the NiCr wires, which were connecting the LHE platform and dewar outlet for electrical connection, were also removed in order to remove all the possible heat leakage pathway, although NiCr wires have very high heat resistance and should not cause much heat leakage. Furthermore, all the O-rings of the dewar were replaced with new ones, because the aging of the rubber O-rings might deteriorate its elasticity and thus the sealing ability.

After this modification of the dewar, a first test was made: only LN2 and keep pumping. The result is in Fig. 5-2 curve 7, showing very long LN2 hold time. This was a good sign to show that the dewar heat leakage was somewhat reduced, and vacuum was not worsen. With the confidence of this, both LN2 and LHE were filled into the dewar and no pumping was applied during the time the dewar temperature was recorded. As can be seen in Fig. 5-2 curve 8, the LHE hold time was dramatically improved: from the previous 1 hour to more than 24.5 hours. This result confirms that the windows, especially three windows, provided a very effective heat leakage which almost dominated the cryogenic performance of the dewar.

Therefore, since only one window was needed for the THz QWP test, two windows (which were designed for THz QWP-LED test and was temporarily unnecessary) were still sealed with Aluminum foil while the other was not, meaning one window not covered with Aluminum foil. The schematic of the dewar now was one window sealed with 2 mm-thick PE plastic on the dewar case. The change of the thickness of the PE plastic on the window was out of the consideration to further reduce the possible vacuum leakage through the window, and the THz transmission would not decrease much. LHE + LN2 test was made again without pumping, resulting in Fig. 5-2 curve 9. The LHE hold time was approximately 2 hours 15 minutes. This was improved compared to curve 5 and curve 6, however much less than the 24 hours shown in curve 8, before one window was uncovered with Aluminum foil. This result, although disappointing, was still a good sign of the major heat leakage with the windows. Even only one window may provide tremendous heat leakage from the outside environment

to the liquid Helium temperature environment.

Now, one thing that might deteriorate the LHE performance, might be the direct heat pathway from the 300K environment or dewar case, into the 4.2K LHE environment on the platform of the LHE tank. Due to the existence of the window on the radiation shield, no intermediate medium existed on the window part. However, the LHE dewar is generally designed to have an LN2 tank, so that the 300K radiation does not pass directly to the 4.2K LHE tank. Rather, 300K dewar case radiates onto the 77K radiation shield, and it was the 77K radiation shield that radiates the 4.2K inner environment of the dewar. The 77K radiation shield accepts 300K radiation, turning to heat flow on the surface of the radiation shield, and has heat balance between the accepted heat and emitted heat. Due to the fact that metal has good heat conductivity, the 300K radiation can flow and dissipate on the wall of the radiation shield very fast. The fast dissipation due to large heat conductivity, effectively prevents the temperature increase in the radiation shield and reduces the heat radiation from radiation shield to LHE tank.

With the above analysis, the window on the radiation shield should be covered with something that is THz-transparent, has low emissivity and relatively high heat conductivity. PE plastic was chosen again because it is apparently THz-transparent. Its emissivity is similar to Aluminum, about 0.1 at the wavelength of $17\mu m$. In order to increase its heat conduction from the PE window to the radiation shield attached to it, a relatively thick PE plastic piece should be used. In the experiment, a 2mm-thick PE plastic was used. As mentioned before, a good heat conduction from the PE window to the attached radiation shield prevents the heat accumulation and thus temperature rise on the PE window to a large extent. Therefore a considerable amount of heat radiation from the window can be reduced. In order to further increase the heat conduction from the PE plastic and the radiation shield, the piece of PE plastic should be in good contact with the radiation shield. In the test, it was screwed on the sidewall and vacuum heat grease was applied on the contacting surfaces. Vacuum heat grease is usually used in cryogenic experiment. It can improve the heat conductivity of the two surfaces that sandwich it, and its outgassing is low. Moreover, there should

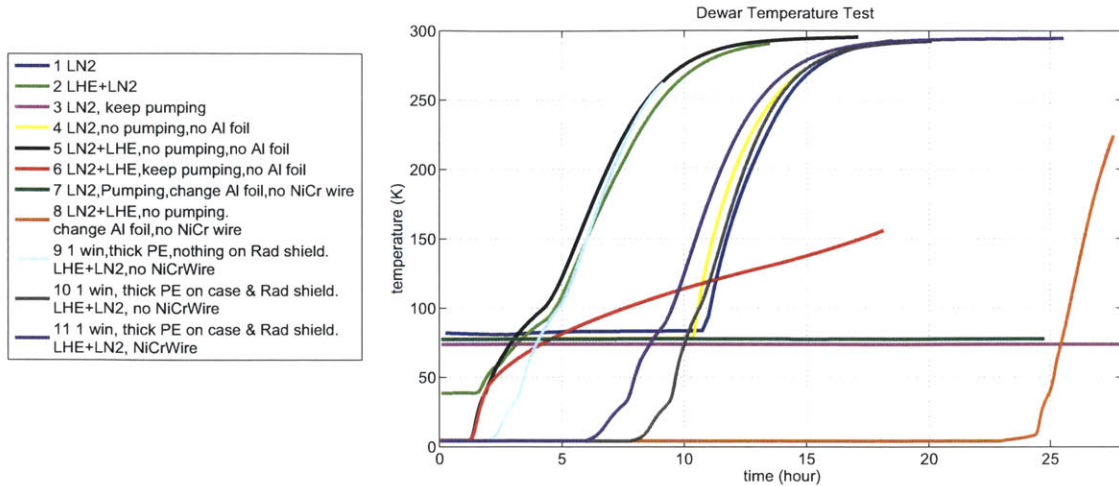


Figure 5-2: Temperature vs. time curves during the cryogenic tests of the LHE dewar. Detailed description of each curve can be referred to the test.

be appropriate sizes of overlapping areas of the PE plastic and radiation shield metal, in order to further improve the heat conduction. Meanwhile, the overlapping area should not be too large, otherwise the emissivity of the inner sidewall of the radiation shield would be increased and thus the cryogenic performance might be worse.

With the above modification, an LHE+LN2 test was performed again without pumping. As can be seen in Fig. 5-2 curve 10, the LHE hold time was 8 hours, dramatically improved due to the addition of a PE plastic on the radiation shield. This result further verifies the validity of the above analysis on radiation and heat flow.

Finally, the electrical NiCr wires were attached again as a further confirmation of the cryogenic ability of the dewar. Fig. 5-2 curve 11 shows the result of the LHE+LN2 test after the reattachment of NiCr wires. The LHE hold time was decreased to 6.5 hours, 1.5 hours shorter than without NiCr wires. However, this hold time was long enough to perform the THz QWP measurement. The actual experiment of THz QWP shows robust cryogenic capability of the LHE dewar: more than 6 hours LHE hold time is consistent through every round of measurement, even with occasional global radiation during the measurement.

5.1.2 The Build-up of Low-noise Electronic Measurement System

This section deals with the electronic measurement system of THz QWP. First, the electronic system inside the dewar is described. Then, the system outside the dewar is discussed.

Electronic Measurement System inside the Dewar

In order to mount the QWP device in the dewar, electrodes and device mounts should be made and anchored on the platform of the dewar LHE tank. A 3D view of the QWP mounted on the He tank of the dewar is shown in Fig. 5-3. The incident THz radiation and the dewar window are shown as well. The top view of the dewar inner side layout is in Fig. 5-4. Dewar case, radiation shield and THz window with PE plastic are shown in the figure. It also shows the liquid Helium tank platform. Si diode temperature sensor, device mounts, electrical wires assembly are anchored on the platform. THz QWP is fixed on the device mount and the 45° facet is facing normal to the THz window. In order to maintain good thermal contact between the He tank platform and pieces anchored on it, Indium pieces are placed between them. Cryogenic Maganin wire twisted pairs are also shown. In the real measurement of the device, cryogenic maganin wires are used instead of NiCr wires, because maganin wires have lower electrical resistivity thus help reduce electrical noise, meanwhile maintaining large thermal resistivity. Twisted pairs are used as a normal convention for low-noise low-frequency measurement. Although the thermal conductance of the Maganin wires is twice as NiCr wires at 4K, the real measurement shows an LHE hold time of about 6.5 hours, the same as NiCr wires. This is a further prove that these cryogenic wires dump negligibly small amount of heat during cryogenic operation, while window heat leakage is dominant. Vacuum tapes are used to tape wires on the platform. Vacuum tapes have very low outgassing and is good to use in vacuum cryogenic environment.

Fig. 5-5 shows a close view of the dewar inner settings with 45° THz QWP

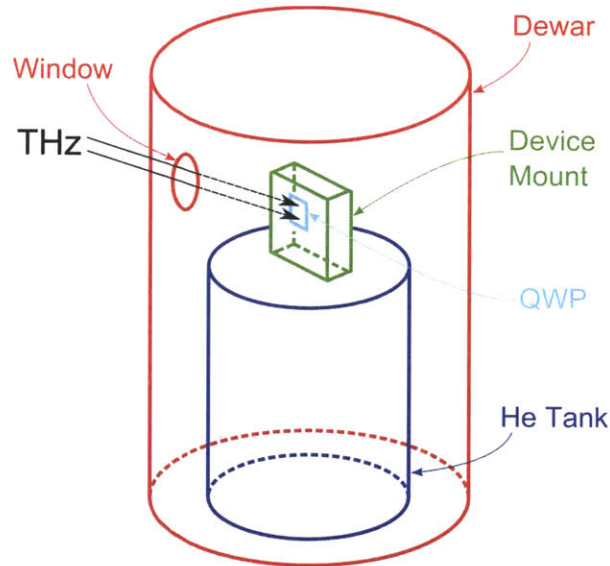


Figure 5-3: 3D plot of THz QWP mounted on the He tank inside the dewar. Incident THz radiation and dewar window are shown as well.

mounted. The figure shows the radiation shield which is covered with Aluminum foil on sidewall, top vertical device mount, chip carrier that is screwed on the top vertical mount, Indium pieces, device mount base that holds the the top vertical mount, THz QWP mounted on chip carrier, vacuum tape, cryogenic maganin wire twisted pairs, electrical wires assembly, and the liquid He tank platform that supports all the aforementioned components.

First, the THz QWP is bonded on the device mount using Indium bond, see Fig. 5-6. On the device, the 45° facet (top view), 4 QWP mesas, 4 bonding pads, common ground contacts can be observed. Gold wires are used to bond the QWP electrodes on the semiconductor piece to the electrodes soldered on the device mounts. Cryogenic maganin wires are then used to connect the electrodes on device mounts and the wire assembly screwed on the He tank platform. Another pair of cryogenic wires are then used to connect the wire assembly and the hermetic connector made on the cover of the dewar (Fig. 5-9).

Fig. 5-7 shows the side view of the 45° QWP mounted on device mounts. The figure clearly shows the 45° facet.

All the device mounts are designed using CAD software SolidWorks and machined

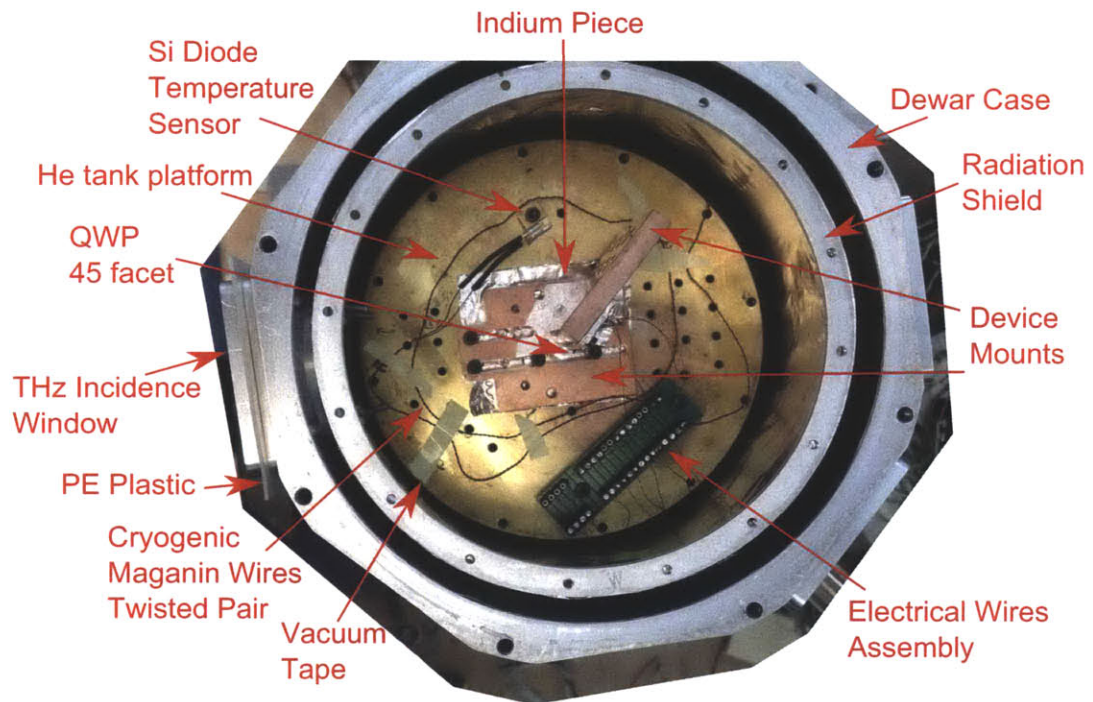


Figure 5-4: The top view of the dewar inner side layout. Dewar case, radiation shield and THz window with PE plastic are shown in the figure. The figure also shows the liquid Helium tank platform. Si diode temperature sensor, device mounts, electrical wires assembly are anchored on the platform. THz QWP is fixed on the device mount and the 45° facet is facing normal to the THz window. Indium pieces, cryogenic Maganin wire twisted pairs and vacuum tapes are shown as well.

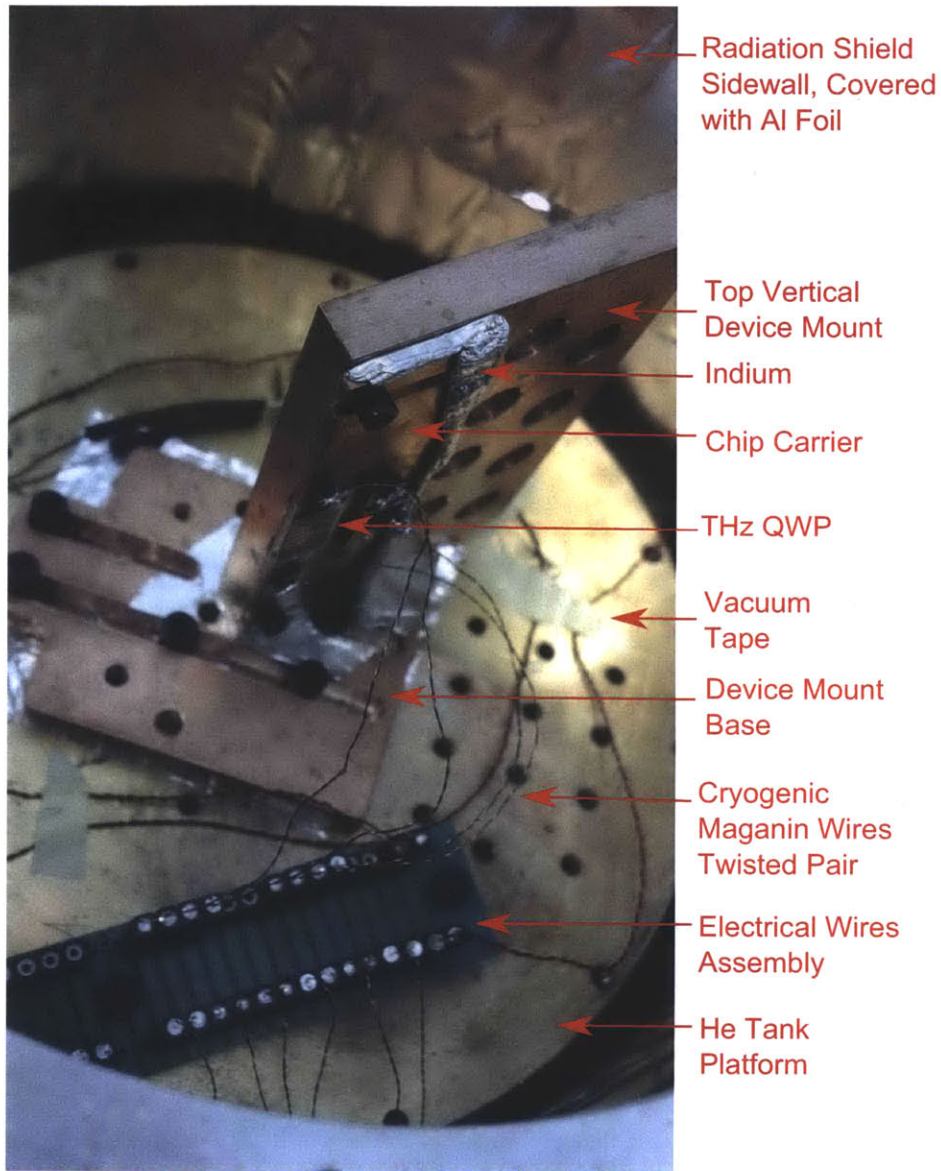


Figure 5-5: A close view of the dewar inner settings with 45° THz QWP mounted. The figure shows the radiation shield which is covered with Aluminum foil on sidewall, top vertical device mount, chip carrier that is screwed on the top vertical mount, Indium pieces, device mount base that holds the the top vertical mount, THz QWP mounted on chip carrier, vacuum tape, cryogenic maganin wire twisted pairs, electrical wires assembly, and the liquid He tank platform that supports all the aforementioned components.

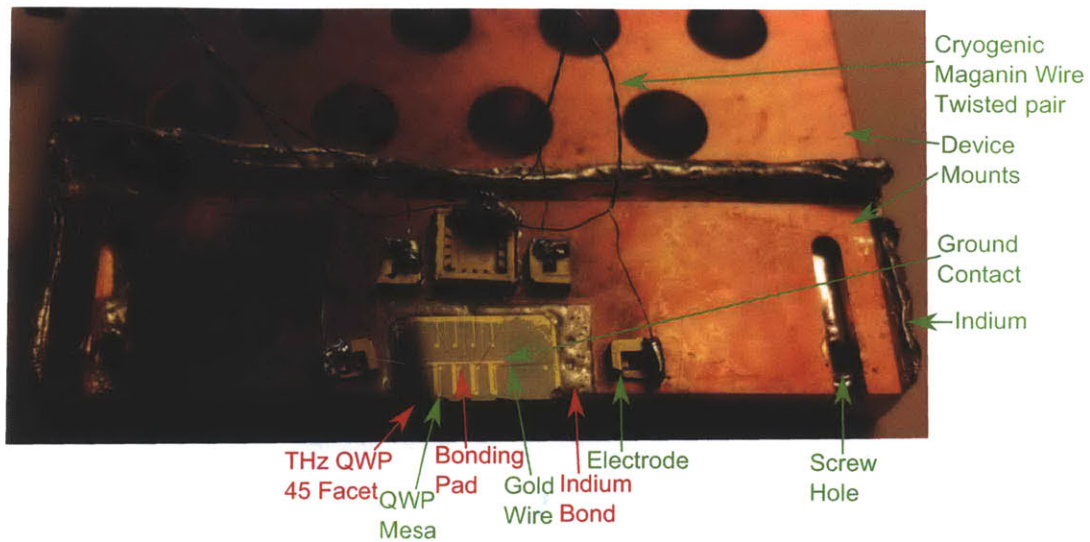


Figure 5-6: THz 45° QWP mounted on device mounts. On the device, the 45° facet (top view), 4 QWP mesas, 4 bonding pads, common ground contacts can be observed. Gold wire-bondings are made to connect electrodes on the QWP and electrodes on the device mounts. Cryogenic maganin wire twisted pairs are soldered to connect electrodes on the device mount and the wire assembly. Indium bond is used to fix the QWP and the Cu device mounts. Indium pieces are applied between device mounts . The screw holes to connect the two device mounts can also be seen.

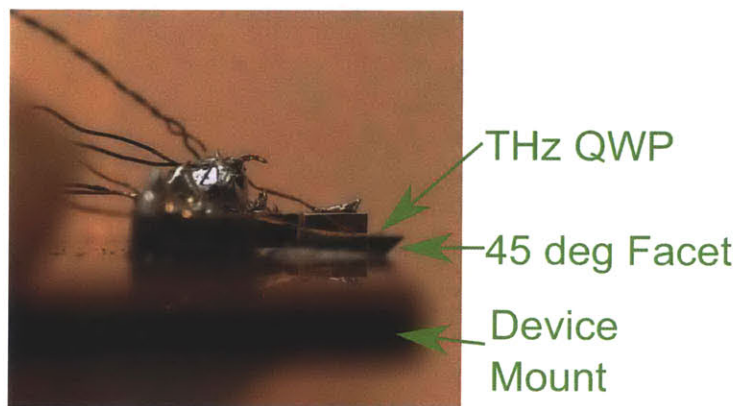


Figure 5-7: The side view of the 45° QWP mounted on device mounts. The figure clearly shows the 45° facet.

using Oxygen-free Cu. They are shown in detail in Appendix A.

Electronic Measurement System outside the Dewar

Several parameters of THz QWP need to be characterized: dark current I-V curve, responsivity, noise current, spectrum. The measurement system, including the QWP inside the dewar and other electrical circuits inside and outside the metal box, is depicted in Fig. 5-8. Dark current I-V curve can be measured directly using Keithley SMU 2400, or connect the QWP in series with a sampling resistor and measure the voltages across the sampling resistor and the QWP. Noise current can also be obtained directly with the spectrum analyzer HP3561A. The responsivity is usually obtained using a calibrated blackbody source with a THz filter and measuring the photocurrent. The ratio of the photocurrent and the incoming light power in THz gives the responsivity [58]. Due to the unavailability of a calibrated blackbody source, a new method to measure the responsivity is schemed: using a narrow-band THz QCL and measure the responsivity. The difficulty of this method is to calibrated the power incident on the QWP mesa, which is only $300\mu m \times 300\mu m$ while the QCL light beam is large in size and not uniform. To do this, a THz lens needs to be used to focus the light from the QCL, and a THz camera needs to be used to perform good alignment by observing the positions light pattern and QWP device in the THz camera. What's more, special attention has to be paid on the polarization of the THz radiation. Because of the linear polarization of THz radiation from QCL and the selection rule in QWP, as well as the orientation of the measurement setup in the lab, two mirrors have to be employed to adjust the polarization of the THz radiation before it reaches the 45° QWP. To measure the spectrum, an FTIR (Nicolet 850 and a homemade one) is used and the light source is a globar.

For testing of THz QWP, the THz source that will be used is a globar, which is essentially a hot object, or a blackbody. The THz signal from the blackbody radiation is quite weak, resulting in a weak optical signal from THz QWP. In this case, the measurement of THz QWP response requires amplification of the signal, while a low-noise electronic environment should be maintained.

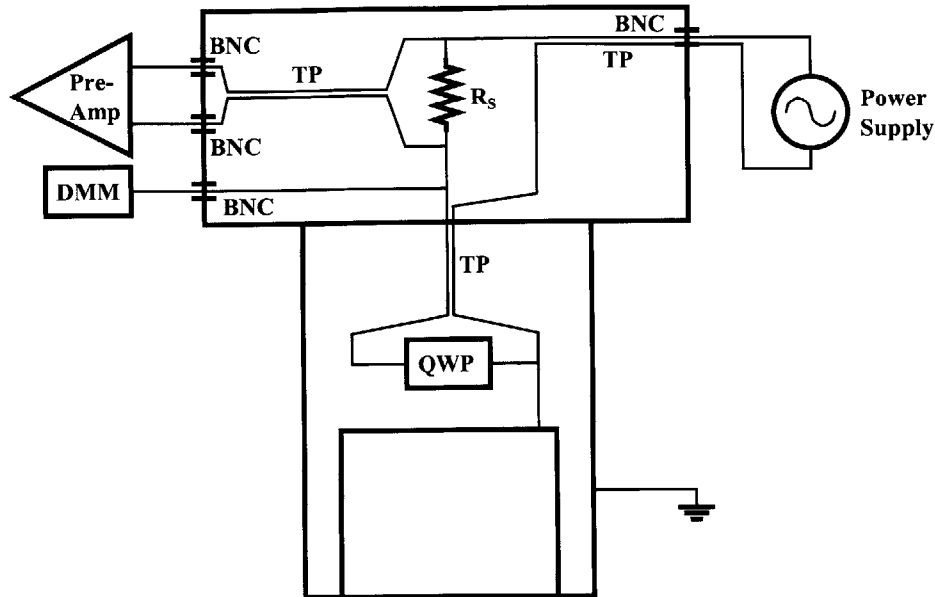


Figure 5-8: The QWP measurement diagram. In the figure, “TP” means twisted pairs, which are used in the dewar and metal box. Outside the box, BNC cables and connectors are used. All the BNC connectors have the common ground which is connected to the dewar case. This configuration is able to achieve low-noise feature. “DMM” is the digital multimeter, which is used to measure the voltage on the QWP.

The amplification of the signal is implemented using a sampling resistor of appropriate resistance, low-noise preamplifier EG&G PAR Model 113 and a lock-in amplifier EG&G PAR Model 5209.

A sampling resistor should be neither too large nor too small. Since the sampling resistor is connected in series with the THz QWP, a large sampling resistance results in low bias on the QWP, while a too small sampling resistance results in low voltage on the sampling resistor and a low response. A sampling resistance similar to the QWP resistance should be used. The THz QWP has a resistance of around $1M\Omega$ in dark condition, so a sampling resistor $R_s = 1M\Omega$ is used. Moreover, the material for the sampling resistor is chosen to be metal-film, because it has the best trade-off between low-noise and high-accuracy among all the common materials for resistors.

The low-noise preamplifier EG&G PAR Model 113 is used to pre-amplify the current signal generated on the QWP, which is essentially the voltage across the sampling resistor. A differential amplification configuration is used for the EG&G

PAR Model 113, because one terminal of the QWP is grounded while both terminals of the sampling resistor are floated. The reason for grounding the QWP is that the ground contact of the QWP is directly connected to the dewar case. Thus, the dewar case serves as a grounding shield to screen out the space electromagnetic waves and other noise. However, if the dewar is floated instead of grounded, it is a huge antenna and can pick up all the space EM wave noise, tremendously deteriorate the performance of the QWP measurement system. What is more, according to the specification of the EG&G PAR Model 113 [59], the noise figure is the lowest when operating frequency is between 100Hz and 1000Hz, and source resistance is on the order of $1M\Omega$. This matches very well with the sampling resistance chosen in our experiment.

The lock-in amplifier EG&G PAR Model 5209 is used to amplify the signal and filter out the noise in a noisy environment, especially when signal frequency distinguishes from the noise frequencies and the amplitude of the signal is much smaller than that of noise.

The low-noise feature is implemented by carefully using twisted pairs and stable signal shielding and grounding. On one hand, twisted pairs of wires are used in connecting QWP and sampling resistor, as can be seen in Figs. 5-4, 5-5 and 5-6. Twisted pairs can be used to shield against magnetic field noise, because they have minimized receiver loop area and the inductive currents generated on the two wires are equal and opposite thus the net field is cancelled out [60]. On the other hand, the low-noise feature also requires stable signal shielding and grounding. In order to do this, a metal box is made and in good contact with the dewar case. All the electrical components are placed inside the metal box, and the connectors are made on the walls of the box, as can be seen in Fig. 5-9. The figure shows the front panel, the rear panel, and the top view and inner side of the metal box. The rotary switch and the hermetic connector are used to switch between different THz QWPs because one chip has multiple THz QWPs. A PCB board is screwed on the sidewall of the metal box for wire connection of the measurement circuit. Twisted pairs of wires are used as mentioned above.

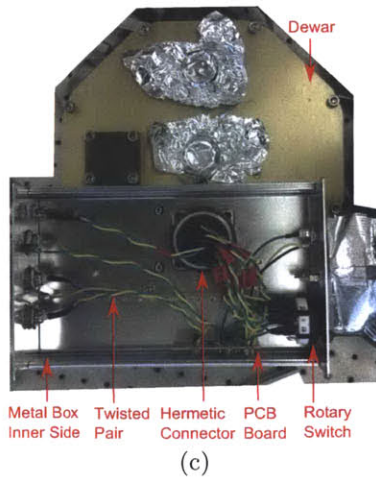
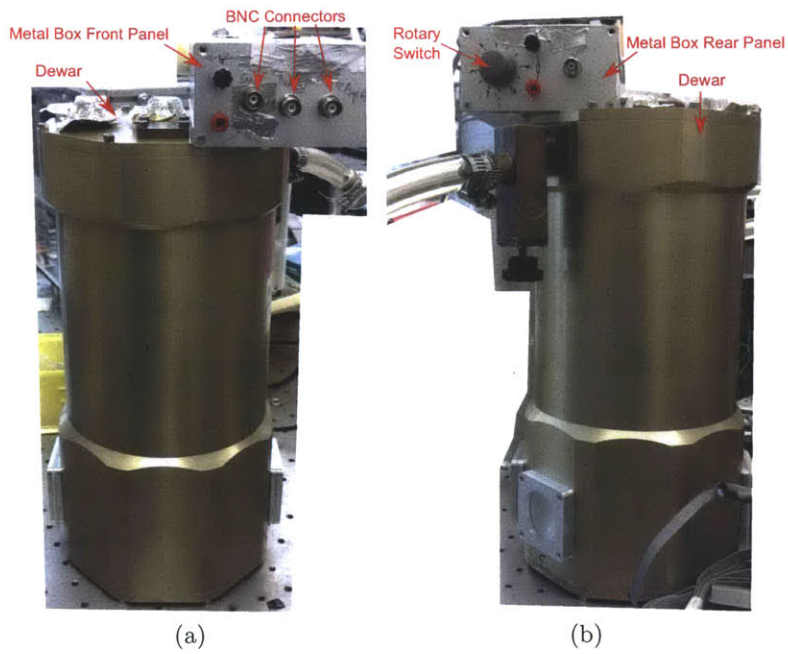


Figure 5-9: Dewar and the metal box attached to it. (a) Front panel. (b) Rear panel. The rotary switch can be seen. (c) Top view. The inner side of the metal box is shown. The rotary switch, the PCB board, the hermetic connector and the twisted pairs can be observed.

After the build-up of the measurement system, a noise performance test was made by replacing the QWP with a $1M\Omega$ metal film resistor. The resistance is chosen because it is similar to the resistance of a QWP at dark case. The noise of the whole measurement system, including the metal box, sampling resistor, preamplifier, digital-multimeters (DMMs), voltage source, and the lock-in amplifier, was measured with HP3561A. The result shows that the noise behavior matches the noise figure of the preamplifier EG&G PAR 113 [59], and the main noise source is the thermal noise. This shows that the measurement system fulfills the low-noise requirement and will not affect measurement result of QWP noise performance.

5.2 Measurement Results

Two types of THz QWPs are measured: the 45° QWP and the grating coupler QWP (wafer number VB0572). Two 45° QWPs (wafer numbers VB0570, M0570) with different MQW structures are included.

M0570 45° THz QWP is obtained from NRC (National Research Council, Canada). It is a THz QWP with MOCVD growth and the mesa size is $800\mu m \times 800\mu m$. Fig. 5-10 shows its current-voltage character (in both linear and log scales) in 4K in cases of Dark, 300K Background, Blackbody radiation, and blackbody radiation with Aluminum foil covering the window. The voltage bias on the QWP is from -0.3V to 0.3V. As seen in the figure, when the voltage bias is small (below approximately 0.1V for both forward and reverse biases), the current is approximately linearly increasing with the voltage. When the voltage further increases (over 0.1V), the current increases faster than linearly, and is quasi-exponential. The figure also shows the photoresponse of the QWP: in 300K background, the current increases compared to dark current; when shining the QWP with blackbody radiation (using a globar at around 1000K), the current further increases; when blocking the window with Aluminum foil with blackbody source still on, the current drops but still larger than 300K background case. This is because the Aluminum foil is also heated and also serves as a THz source for the QWP.

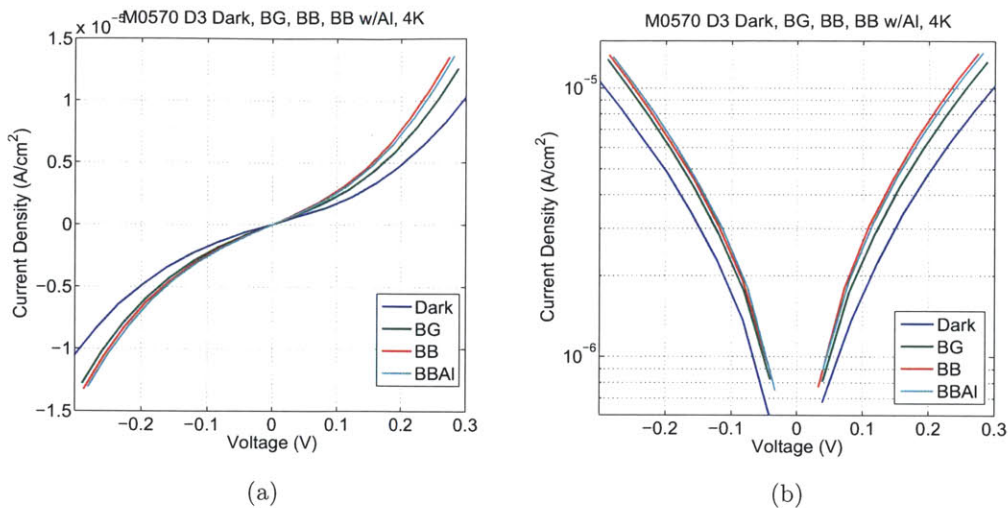


Figure 5-10: M0570's current-voltage character (in both linear and log scales) in 4K in four cases: Dark, 300K Background, Blackbody radiation, and blackbody radiation with Aluminum foil covering the window. These four cases are denoted as "Dark", "BG", "BB", "BBAI" in the legend, respectively. The voltage bias on the QWP is from -0.3V to 0.3V.

Fig. 5-11 shows the spectrum of M0570 and DTGS detector taken with FTIR Nicolet 850. The bias voltage on the QWP is -0.3V. In the spectrum measurement of M0570, a chopper is used to modulate the continuous THz light source and is placed immediately after the aperture for the global THz source. The chopper signal is then used as the reference signal for the lock-in amplifier, and the signal input of the lock-in amplifier is the pre-amplified voltage across the sampling resistor. Several parameter settings for the electrical instruments are tried in order to filter out the noise and get a QWP spectrum as good as possible. The best configuration is described below. Chopping frequency is 310Hz. The preamplifier gain is 100, low-frequency roll-off is 100Hz and high frequency roll-off is 1KHz, AC-coupled. The lock-in amplifier uses a time-constant of 100ms and voltage sensitivity of 300mV, resulting in a voltage percentage full-scale of approximately 9.3%. The FTIR uses an aperture size of 28, mirror velocity of 0.0475cm/s , resolution 1cm^{-1} , gain 8, and takes 10 scans for averaging. A good match and combination of these parameters are important to get a clean spectrum. The chopping frequency should be large enough to filter out low-frequency

noise and other fluctuations in the system, while a too large chopping frequency will deteriorate the performance of the preamplifier. This chopping frequency limits the low- and high- frequency roll-off of the preamplifier. While the frequency range set by the amplifier should include the chopping frequency and should not be very narrow, a too broad frequency range includes more noise in the system and is undesirable. The mirror velocity of the FTIR is thus dependent on the chopping frequency. A large mirror velocity can be used when the chopping frequency is large. Since the chopping frequency used here is small, the mirror can only move very slowly in order to get the signals for the spectrum. A slow mirror velocity also helps to reduce noise due to the averaging effect. However, too slow mirror velocity causes the problems of long measurement time, unsmooth movement of the mirror or even temporary movement halt of the mirror, and the measurement system is more subjective to the environment. Taking more scans for averaging can also lower the noise and partly compensate the drawbacks of the low mirror velocity, but it induces a long measurement time as well, and the mirror velocity still has upper limit no matter how many scans the FTIR takes. The chopping frequency and mirror velocity also limit the time constant of the lock-in amplifier: the larger the chopping frequency, the smaller the time constant can be; and the larger the mirror velocity, the smaller the time constant. Since the chopping frequency used here is quite small and so is the mirror velocity, the time constant should be relatively large. However, too large time constant will result in insufficient sampling. Finally, the size of the aperture is important, too. A large aperture allows more THz light and may result in larger signal, but since the global source is very poorly collimated, a small aperture helps collimate the light and eases the optical system alignment in the measurement. The optical alignment is also very important because the THz power from the global is already quite weak, not to mention it has to go through a long way in the FTIR before it reaches the QWP. A HeNe laser is used to align the optical components in the FTIR and the rough position of the QWP. A further fine tuning of the QWP position is based on the maximization of the QWP signal shown on the lock-in amplifier.

A further note on the spectrum measurement of the QWP is that a QWP is based

on the quantum mechanism and is a fast detector. Therefore, if the photoresponse is not very small, chopping is not necessary when taking spectrum. Therefore, a lock-in amplifier is not required either, and the mirror velocity does not need to be very small. In the case of M0570, this is true: spectrum can also be taken without chopping and with a mirror velocity as large as 0.6cm/s , and the resulting spectrum is similar as in Fig. 5-11. However, this is based on the fact that M0570 has a large mesa area and large 45° facet area, allowing more THz light incident on the device thus resulting in larger signal. In the case of VB0570 and VB0572, the mesa area is only approximately 1/8 of M0570, and the signal is much smaller. Chopping and lock-in amplification is necessary in the measurement of these QWPs, despite the preamplifier.

As can be seen in the spectrum of M0570 (Fig. 5-11), the cut-off frequency of this QWP is approximately 4.2 THz. The Reststrahlen band of GaAs (about 7.5-9 THz) can be observed, which is due to the optical phonon absorption. The dips in the spectrum is due to water absorption of THz light. These water absorption dips matches the High-resolution transmission molecular absorption (HITRAN) database [61] as well as the DTGS spectrum taken in the same day (also shown in Fig. 5-11), which further confirms the validity of the spectrum taken from THz QWP M0570. Moreover, this spectrum of M0570 matches the results from NRC [62].

The noise current of M0570 is $0.3789\text{pA}/\sqrt{\text{Hz}}$ under Blackbody radiation and $0.3534\text{pA}/\sqrt{\text{Hz}}$ in dark condition. The bias of the QWP is 0.4V. Consider the thermal (Johnson) noise current shown in Eqn. (2.79), $\frac{i_{n,J}}{\Delta f} = \sqrt{\frac{4k_B T}{R}} = 0.0086\text{pA}/\sqrt{\text{Hz}}$, much smaller than the noise current measured. This confirms that the Johnson noise is not the limiting component of noise current in this device. From this result, the photoconductive gain and dark current noise gain of this device can be calculated according to Eqn. (2.81) and Eqn. (2.82), and they are $g_{photo} = 0.0236$ and $g_{dark} = 0.0268$. Eliminating the uncertainty and inaccuracy due to the instrument and measurement system, the photoconductive gain and dark current noise gain are very close. This result matches the assumption in Chapter 2.2.

To estimate the NEP of M0570, consider the blackbody source used for noise cur-

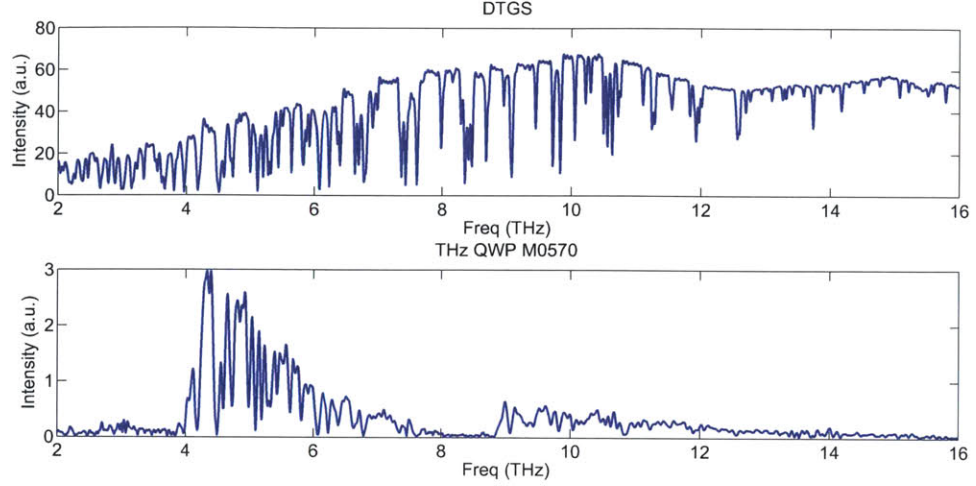


Figure 5-11: The spectra of the DTGS detector and THz QWP M0570. The bias voltage on the QWP is -0.3V. The cut-off frequency of the THz QWP is approximately 4.2 THz. The reststrahlen band of GaAs (about 7.5-9 THz) can be observed. The dips in the spectrum is due to water absorption of THz light. These water absorption dips matches the High-resolution transmission molecular absorption (HITRAN) database [61] as well as the DTGS spectrum taken in the same day. This spectrum of M0570 matches the results from NRC [62].

rent measurement. Its temperature is approximately 1000K during the measurement, and it is placed 26cm away from the QWP. Using Planck's Law of blackbody radiation, the THz power for 1THz bandwidth at approximately 4THz is approximately $4.49W/(m^2 \cdot steradian)$. Considering the loss due to the windows ($transmission \approx (74\%)^2$), reflection on the GaAs/air interface ($transmission$ is $\frac{2n_{air}}{n_{GaAs}}$), and 45° tilted incidence (1/2 power loss), and the entendue, the power absorbed by the QWP is around $P_{THz} = 4.49 \frac{W}{(m^2 \cdot steradian)} \times (74\%)^2 \times \frac{2n_{air}}{n_{GaAs}} \times \frac{1}{2} 4\pi \frac{(800\mu m)^2}{4\pi(26cm)^2} \cdot \pi(1cm)^2 \cdot 2 = 4.28 \times 10^{-9}W$. In this equation, 4π is the solid angle of the radiation, $\pi(1cm)^2$ is the area of the globar, and the last factor 2 is considering the reflection provided by the mirror at the backside of the globar used here. Therefore, combining the I-V curve, the responsivity of the QWP is approximately $Res = (I_{photo} - I_{dark})/P_{THz} \approx 7.88A/W$. Therefore, its NEP is around $NEP = i_{n,photo}/Res = 0.048pW/\sqrt{Hz}$. The specific detectivity is $D^* = \sqrt{Area}/NEP = 1.67 \times 10^{12}cm \cdot \sqrt{Hz}/W$. This detectivity value is comparable to that in [63, 26].

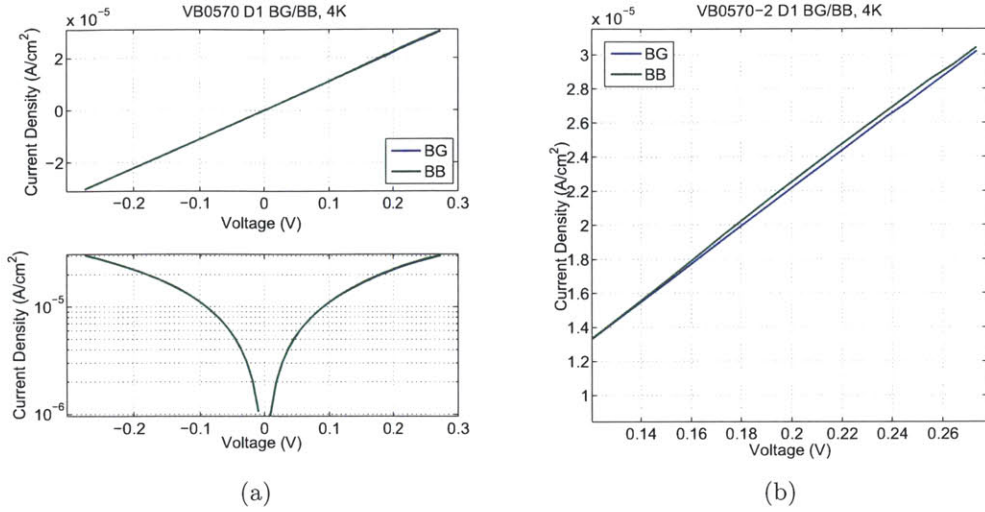


Figure 5-12: The figures show the I-V curve of THz QWP VB0570 at 4K. Both blackbody radiation case (denoted as "BB" in legend) and 300K background case (denoted as "BG" in legend) are shown. (a) shows the curves in both linear and logarithm scales and the bias range is from -0.3V to 0.3V. (b) is an enlargement of the linear scale I-V curve, showing the difference between blackbody radiation and dark case.

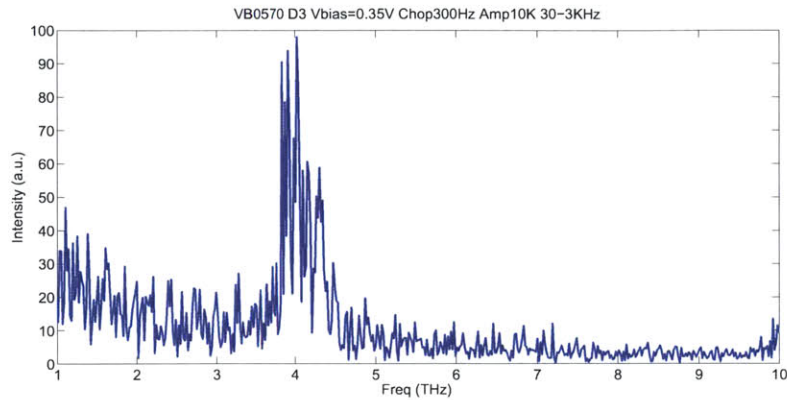
Fig. 5-12 shows the I-V curve of THz QWP VB0570 at 4K. This wafer is MBE grown and follows the design shown in Chapter 3. Both blackbody radiation case (denoted as "BB" in legend) and 300K background case (denoted as "BG" in legend) are shown. Fig. 5-12a shows the curves in both linear and logarithm scales and the bias range is from -0.3V to 0.3V. Fig. 5-12b is an enlargement of the linear scale I-V curve, showing the difference between blackbody radiation and dark case. The current density of this device is larger than that of M0570, due to the difference in MQW structures. However, the photoresponse is much smaller: the difference between blackbody case and dark case are very small. This is due to the shrink of the mesa size, and the imperfections on the tilted facet which reduces light coupling.

Because the photoresponse of this THz QWP is very small, chopping and lock-in amplification during photoresponse spectrum measurement is necessary. Moreover, a very slow mirror velocity is necessary. However, the slowest mirror velocity that the FTIR Nicolet 850 could achieve was 0.15cm/s during the period that the measurement

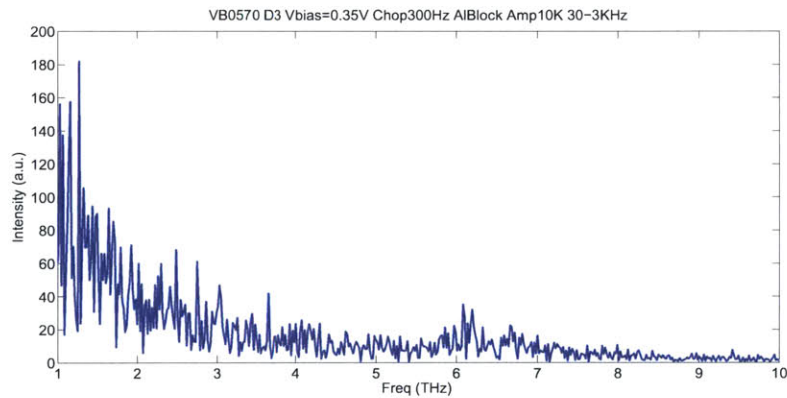
was taken. Therefore, a home-made FTIR is used to measure the spectral response of QWP VB0570. The smallest mirror velocity is as low as 0.05mm/s .

Fig. 5-13 shows the spectrum of one THz QWP VB0570. (a) shows the photoreponse spectrum. (b) shows the case when Aluminum was used to block the global THz source of the FTIR. It is essentially noise spectrum because all the other configurations are exactly the same as in (a). The QWP bias is 0.35V , chopping frequency 300Hz , pre-amplification is 10K and frequency range is $300\text{-}3\text{KHz}$. A mirror velocity of 0.08mm/s was used. Lock-in Amplifier time constant is 100ms . This combination of instrument parameters was finally chosen based on numerous trials and errors. It turns out this configuration gives one of the best spectra one can get. The global THz source is an external one and has much poorer light beam collimation than an internal global of FTIR. Thus, an $F/1$ THz Silicon lens is used to collimate the beam as best as possible. The focal length of this lens is $2''$. Things get much worse when an $F/3$ (focal length is $6''$) OAP (off-axis parabola) gold-coated mirror is used to collimate the beam. The reason may be that a longer focal length causes much more loss of THz signal, and the alignment using an OAP is much less straightforward than a lens. Also, no aperture is used in this measurement of spectrum. The chopping blade is placed directly after the global. Therefore, the chopping blade is easily heated up and serves as a blackbody source itself, though temperature somewhat lower than the global. This results in poor modulation of light, making the lock-in amplification much noisier. Overall, due to the poor light beam quality of the THz source and poor modulation, together with other electrical noise picked-up from space and existing in the electrical components, the spectrum of this QWP is much noisier than the previous one. However, comparing Fig. 5-13a and Fig. 5-13b, it is clear that the peak at about $3\text{-}5\text{THz}$ in Fig. 5-13a is the spectrum of the light response. Also, the peak situates at about 4THz , and matches well with the design and simulation. This is a further confirmation that this spectrum is the photoresponse spectrum of THz QWP VB0570.

The noise current of VB0570 is $0.00645\text{pA}/\sqrt{\text{Hz}}$ under Blackbody radiation and $0.00313\text{pA}/\sqrt{\text{Hz}}$ in dark condition. The bias of the QWP is 0.4V . The thermal



(a)



(b)

Figure 5-13: The figure shows the spectrum of one THz QWP VB0570. (a) shows the photoresponse spectrum. (b) shows the case when Aluminum was used to block the global THz source of the FTIR. It is essentially noise spectrum because all the other configurations are exactly the same as in (a). The QWP bias is 0.35V, chopping frequency 300Hz, pre-amplification is 10K and frequency range is 300-3KHz. A mirror velocity of 0.08mm/s was used. Lock-in Amplifier time constant is 100ms. The global THz source is an external one and its beam is collimated using an F/1 (focal length is 2") THz Silicon lens. The photoresponse peak situates at about 4THz, and matches well with the design and simulation.

(Johnson) noise current is calculated to be $0.004pA/\sqrt{Hz}$. This is smaller than the photocurrent noise while comparable to dark current noise. However, this still shows that the Johnson noise is not the limiting component of noise current in this device. From this result, the photoconductive gain is calculated to be $g_{photo} = 0.0055$.

To estimate the NEP of VB0570, consider the blackbody source at approximately 1000K during the measurement, and it is placed about $26.5cm$ away from the QWP. Similar to the estimation of M0570's NEP, the power absorbed by the QWP is around $4.12 \times 10^{-9}W$. The responsivity of the QWP is approximately $0.048A/W$. Therefore, its NEP is around $0.134pW/\sqrt{Hz}$. The specific detectivity is $2.24 \times 10^{11}cm \cdot \sqrt{Hz}/W$. This detectivity value is comparable to that in [63, 26].

For the grating coupler THz QWP VB0572, I-V curves for all the 8 devices on the same chip are measured. They have quite similar current characters. Fig. 5-14 shows the I-V curves for two of the eight grating coupler QWPs. The I-V curves include dark current and 300K background case, and I-V curves at different device temperatures are measured as well. Particularly, at 4K, a QCL (VB0523-M1) is used to shine THz radiation on the QWP. The QCL operates in pulse-mode with the modulation frequency of 10KHz and pulsewidth 500ns. Its peak power is 21mW. The lasing frequency of the QCL is 4THz. The I-V curves are measured using SMU2635. Although the SMU2635 cannot respond as fast as 10KHz, the difference in currents before and after QCL shining suggests that the grating coupler QWPs have photoreponse. Also, the current density magnitude at 4K is around $10^{-6} - 10^{-5}A/cm^2$, since the mesa area is $300\mu m \times 300\mu m$. As QWP temperature rises, the current increases. Notice that when device temperature is above about 28K, the increase of current due to the increase of temperature is very small. Because the dark current has exponentially dependence on temperature (Eqn. (2.55), Eqn. (2.39)) while the blackbody radiation power is only a polynomial function of temperature, the dark current gradually dominates when temperature increases. From 4K to 28K, the dark current density increase about 5 orders of magnitudes, which shows the increase in thermal activation of the electrons, and this is consistent with the carrier density terms in the dark current model for both 3D drift model and emission-capture model. Above 28K,

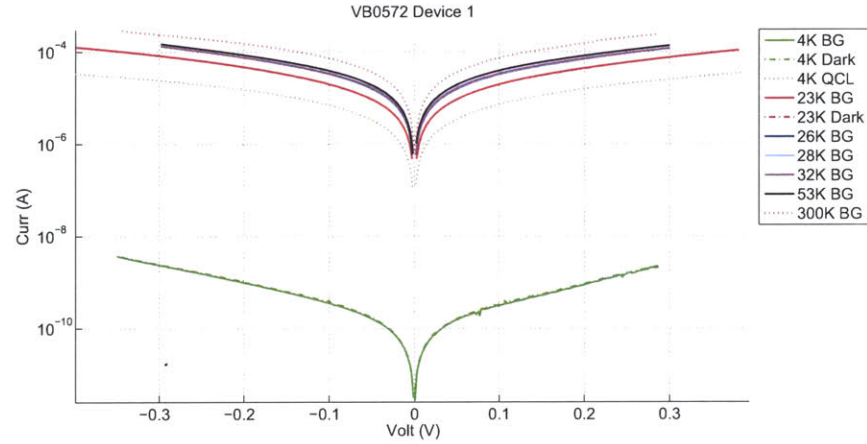
the increase of current slows down, which suggests that there are other mechanisms, e.g. scattering, contributing to dark current except for electron thermal activation. This is considered in the emission-capture model for dark current. Therefore, the measurement results suggest that the dark current model of emission-capture model combined with 3D drift model is reasonable in describing dark current of QWPs.

The noise of dark current and dark current noise gain of all the eight grating coupler THz QWPs on VB0572 are shown in Table 5.1. The dark current noise is also small and dark current gain is comparable to that of VB0570. The thermal noise current of these devices is on the order of $0.001 pA/\sqrt{Hz}$, smaller than the measured noise current, suggesting that Johnson noise is not the limiting factor for noise current here. Notice that in Table 5.1, Device 4 and Device 8 has much lower dark current noise than other devices. This may be caused by the nonuniform dry-etch for these two devices close to the edge of the chip, thus poor light coupling and low-quality mesa sidewalls may contribute to the small photocurrent, thus possibly small noise current.

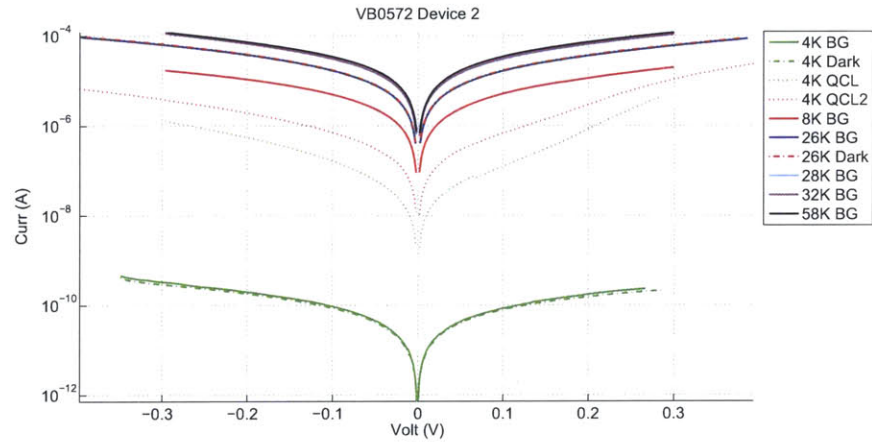
Device No.	dark current noise (pA/\sqrt{Hz})	dark current noise gain
1	0.1574	0.0475
2	0.1652	0.4490
3	0.1294	0.0448
4	0.0096	0.0003
5	0.1476	0.3236
6	0.1460	0.0093
7	0.1503	0.0022
8	0.0371	0.0178

Table 5.1: Dark current noise and dark current gain measured from the grating coupler THz QWP, wafer VB0572. Device 4 and Device 8 has much lower dark current noise than other devices. This may be caused by the nonuniform dry-etch for these two devices close to the edge of the chip.

As a conclusion, the measurement results show matched performance of the QWPs as described in the theory and simulation. The noise of the QWPs turns out to be small, which is promising for implementing fast and sensitive THz imaging FPA based on the THz QWPs.



(a)



(b)

Figure 5-14: The figure shows the I-V curves for two of the eight grating coupler QWPs in wafer VB0572. The curves include dark current and 300K background case, and at different device temperatures. Particularly, at 4K, a QCL (VB0523-M1) is used to shine THz radiation on the QWP. The QCL operates in pulse-mode with the modulation frequency of 10KHz and pulsewidth 500ns. Its peak power is 21mW. The I-V curves are measured using SMU2635. The current density magnitude at 4K is around $10^{-6} - 10^{-5} A/cm^2$, since the mesa area is $300\mu m \times 300\mu m$.

Chapter 6

Conclusion and Future Work

6.1 Conclusion

In this project, a THz QWP with 4 THz peak absorption and a low NEP is aimed. The theory on intersubband absorption and carrier transport is studied in detail, which leads to the design guideline of the QWP. Further design uses $k \cdot p$ method and FEM simulation on EM calculation. In order to avoid the drawbacks of selection rule, two schemes are used: 45° incidence QWP and grating coupler QWP. The grating coupler QWP, together with a plasma-reflector layer is designed and calculated with the FEM calculation software COMSOL. An absorption efficiency over 80% is predicted with the grating coupler QWP.

The fabrication processes of the 45° QWP and grating coupler QWP are designed and performed on the MBE grown wafers. A cryogenic and low-noise testing system is built-up to cater the needs and features of THz QWP. Measurement results show clear photoresponse of both THz QWPs. The spectra and current behaviors match that of the design, and the NEP satisfies the initial aim.

Besides THz QWP, a THz QWP-LED structure is also designed. Similar with THz QWP, both 45° incidence QWP-LED and grating coupler QWP-LED are designed with $k \cdot p$ method and FEM simulation. P-type plasma reflector is used. An absorption efficiency of 70% can be achieved. The fabrication processes are designed and tested, which requires the technique using BCB to bond sapphire substrate and GaAs pieces.

6.2 Future Work

With the results that has been obtained from the current work, several future directions can be aimed:

1. Improve the calculation on intersubband transition by taking into account the many body effect [62, 64] in QWP system and including the exchange-correlation potential in the quantum transport. However, the error introduced in the actual MBE growth may mask the error introduced by the omission in this calculation.

2. It turns out the bonding pad is not necessary. So simplification of the fabrication processes can be planned.

3. The cryogenic system can be further modified with better dewar or closed-cycle measurement system. The latter can control the temperature much easier, implementing more convenient measurement with different temperatures.

4. The responsivity measurement can be modified using either calibrated black-body radiation source, or a QCL and a THz camera to align the light beam and QWP surface. This method tends to be more accurate.

5. When the MBE growth of p-type GaAs is available, QWP-LED can be implemented.

6. With satisfactory pixel-size QWP and QWP-LED, a THz QWP FPA can be explored. Real-time THz imaging can be implemented based on the FPA.

7. In terms of THz detectors, some other directions may be worth exploring. Due to the recent discovery of graphene's [65] response in THz due to its plasmonic resonant frequency [66, 67], it may be a promising material to implement tunable THz photodetectors and other THz devices.

Appendix A

Device Mounts used in dewar

All the device mounts are designed using CAD software SolidWorks and machined using Oxygen-free Cu. For the 45° THz QWP, 3 mounts are needed: a chip carrier that holds the QWP, the top vertical mount that holds the chip carrier, and the base that holds the vertical mount and anchored on the He tank platform. The three parts are screwed together when mounted in the dewar and the screw holes are clearly observed in the figure. The base can be used for other THz QWPs or QWP-LEDs as well. The mechanical drawing of these three mounts are shown in Fig. A-1. These device mounts can also be used for the 45° THz QWP-LED.

The grating coupler QWP is mounted in similar fashion as the 45° QWP, except that the surface of the grating coupler QWP should face normal to the THz window, rather than backside facing at 45° in the 45° QWP. The device mounts for the grating coupler QWP also consist three parts: a chip carrier, a top vertical mount, and a base. The former two are shown in Fig. A-2.

Moreover, the device mounts for the grating coupler THz QWP-LED are also designed. They are similar to the mounts for the grating coupler THz QWP, except for a hole existed on the chip carrier and vertical top mount. The hole is for emitting out the generated NIR radiation from LED part. Its chip carrier and top vertical mount are shown in Fig. A-3.

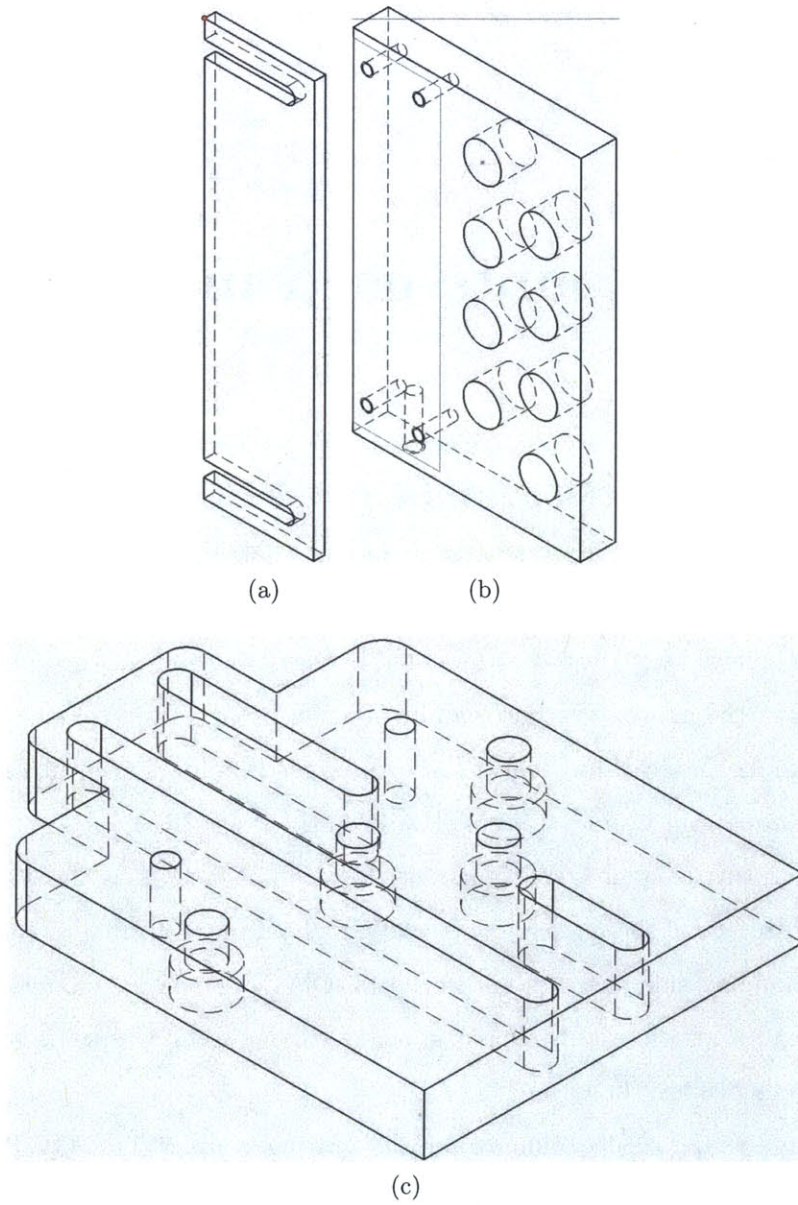


Figure A-1: Mechanical drawings of the device mounts used for the 45° THz QWP. (a) The chip carrier that holds the device. (b) The top vertical mount that holds the chip carrier. (c) The base that holds the vertical mount and anchored on the He tank platform. The base can be used for other THz QWPs or QWP-LEDs as well.

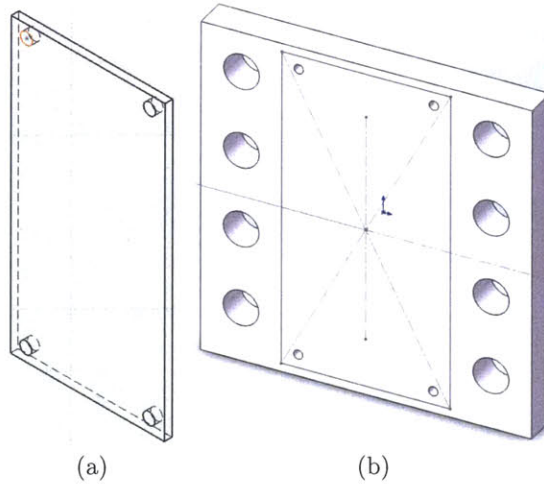


Figure A-2: Mechanical drawings of the device mounts used for the grating coupler THz QWP. (a) The chip carrier that holds the device. (b) The top vertical mount that holds the chip carrier. The base is the same as in 45° QWP and is shown in Fig. A-1c.

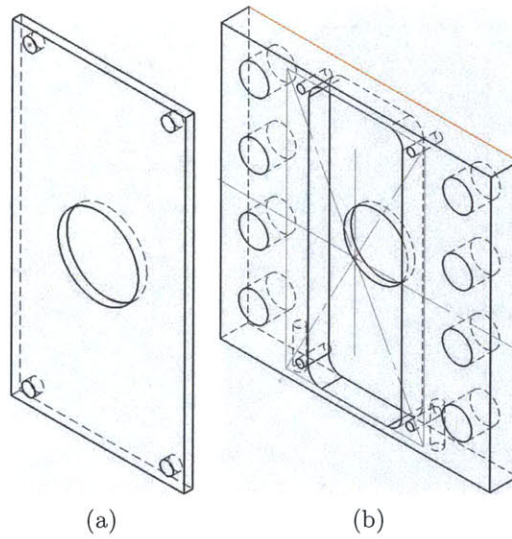


Figure A-3: Mechanical drawings of the device mounts used for the grating coupler THz QWP-LED. (a) The chip carrier that holds the device. (b) The top vertical mount that holds the chip carrier. The base is the same as in 45° QWP and is shown in Fig. A-1c.

Bibliography

- [1] Y.-S. Lee, *Principles of terahertz science and technology*. Springer Oregon, USA, 2008.
- [2] X.-C. Zhang, *Introduction to THz wave photonics*. Springer, 2010.
- [3] D. Woolard, E. Brown, M. Pepper, and M. Kemp, “Terahertz frequency sensing and imaging: A time of reckoning future applications?” *Proceedings of the IEEE*, vol. 93, no. 10, pp. 1722–1743, 2005.
- [4] R. Köhler, A. Tredicucci, F. Beltram, H. E. Beere, E. H. Linfield, A. G. Davies, D. A. Ritchie, R. C. Iotti, and F. Rossi, “Terahertz semiconductor-heterostructure laser,” *Nature*, vol. 417, no. 6885, pp. 156–159, 2002.
- [5] M. Rochat, L. Ajili, H. Willenberg, J. Faist, H. Beere, G. Davies, E. Linfield, and D. Ritchie, “Low-threshold terahertz quantum-cascade lasers,” *Applied Physics Letters*, vol. 81, no. 8, pp. 1381–1383, 2002.
- [6] B. S. Williams, H. Callebaut, S. Kumar, Q. Hu, and J. L. Reno, “3.4-thz quantum cascade laser based on longitudinal-optical-phonon scattering for depopulation,” *Applied Physics Letters*, vol. 82, no. 7, pp. 1015–1017, 2003.
- [7] S. Fatholouloumi, E. Dupont, Z. Wasilewski, C. Chan, S. Razavipour, S. Laframboise, S. Huang, Q. Hu, D. Ban, and H. Liu, “Effect of oscillator strength and intermediate resonance on the performance of resonant phonon-based terahertz quantum cascade lasers,” *Journal of Applied Physics*, vol. 113, no. 11, pp. 113 109–113 109, 2013.
- [8] N. Byer, S. Stokowski, and J. Venables, “Complementary domain pyroelectric detectors with reduced sensitivity to mechanical vibrations and temperature changes,” *Applied Physics Letters*, vol. 27, no. 12, pp. 639–641, 1975.
- [9] E. Fukada and T. Furukawa, “Piezoelectricity and ferroelectricity in polyvinylidene fluoride,” *Ultrasonics*, vol. 19, no. 1, pp. 31–39, 1981.
- [10] H. Li, J. Cao, Y. Han, Z. Tan, and X. Guo, “Temperature profile modelling and experimental investigation of thermal resistance of terahertz quantum-cascade lasers,” *Journal of Physics D: Applied Physics*, vol. 42, no. 20, p. 205102, 2009.

- [11] J. Yang, S. Ruan, and M. Zhang, "Real-time, continuous-wave terahertz imaging by a pyroelectric camera," *Chin. Opt. Lett.*, vol. 6, no. 1, pp. 29–31, Jan 2008.
- [12] A. Goss, R. Nixon, R. Watton, and W. Wreathall, "Infrared Television Using The Pyro-Electric Vidicon," *GEC Journal of Research*, vol. 2, no. 3, pp. 198–203, 1984.
- [13] R. B. Lal and A. K. Batra, "Growth and properties of triglycine sulfate (tgs) crystals: Review," *Ferroelectrics*, vol. 142, no. 1, pp. 51–82, 1993.
- [14] P. M. Downey, A. D. Jeffries, S. S. Meyer, R. Weiss, F. J. Bachner, J. P. Donnelly, W. T. Lindley, R. W. Mountain, and D. J. Silversmith, "Monolithic silicon bolometers," *Appl. Opt.*, vol. 23, no. 6, pp. 910–914, Mar 1984.
- [15] P. L. Richards, "Bolometers for infrared and millimeter waves," *Journal of Applied Physics*, vol. 76, no. 1, pp. 1–24, 1994.
- [16] E. E. Haller, M. R. Hueschen, and P. L. Richards, "Ge : Ga photoconductors in low infrared backgrounds," *Applied Physics Letters*, vol. 34, no. 8, pp. 495–497, 1979.
- [17] E. E. Haller, "Advanced far-infrared detectors," *Infrared Physics & Technology*, vol. 35, no. 2, pp. 127–146, 1994.
- [18] E. Gornik, "Far infrared light emitters and detectors," *Physica B+ C*, vol. 127, no. 1, pp. 95–103, 1984.
- [19] L. Wu and W. Shen, "Far-infrared upconversion imaging devices: Imaging characteristics and quantum efficiency," *Journal of applied physics*, vol. 100, no. 4, pp. 044 508–044 508, 2006.
- [20] S. Matsik, M. Rinzan, A. Perera, H. Liu, Z. Wasilewski, and M. Buchanan, "Cutoff tailorability of heterojunction terahertz detectors," *Applied physics letters*, vol. 82, no. 1, pp. 139–141, 2003.
- [21] A. Perera, "Quantum structures for multiband photon detection," *Opto-Electronics Review*, vol. 14, no. 2, pp. 99–108, 2006.
- [22] A. Perera, W. Shen, H. Liu, M. Buchanan, and W. Schaff, "Gaas homojunction interfacial workfunction internal photoemission (hiwip) far-infrared detectors," *Materials Science and Engineering: B*, vol. 74, no. 1, pp. 56–60, 2000.
- [23] B. Levine, "Quantum-well infrared photodetectors," *Journal of applied physics*, vol. 74, no. 8, pp. R1–R81, 1993.
- [24] H. Liu, C. Song, A. SpringThorpe, and J. Cao, "Terahertz quantum-well photodetector," *Applied physics letters*, vol. 84, no. 20, pp. 4068–4070, 2004.

- [25] H. Luo, H. C. Liu, C. Y. Song, and Z. R. Wasilewski, "Background-limited terahertz quantum-well photodetector," *Applied Physics Letters*, vol. 86, no. 23, p. 231103, 2005.
- [26] R. Zhang, X. Guo, C. Song, M. Buchanan, Z. Wasilewski, J. Cao, and H. Liu, "Metal-grating-coupled terahertz quantum-well photodetectors," *Electron Device Letters, IEEE*, vol. 32, no. 5, pp. 659–661, 2011.
- [27] Z. Tan, X. Guo, J. Cao, H. Li, X. Wang, S. Feng, Z. R. Wasilewski, and H. C. Liu, "Temperature dependence of current–voltage characteristics of terahertz quantum-well photodetectors," *Semiconductor Science and Technology*, vol. 24, no. 11, p. 115014, 2009.
- [28] H. Schneider and H. C. Liu, *Quantum-Well Infrared Photodetectors*, 2007.
- [29] B. F. Levine, C. G. Bethea, G. Hasnain, V. O. Shen, E. Pelve, R. R. Abbott, and S. J. Hsieh, "High sensitivity low dark current 10 μm gaas quantum well infrared photodetectors," *Applied Physics Letters*, vol. 56, no. 9, pp. 851–853, 1990.
- [30] H. C. Liu, E. Dupont, M. Byloos, M. Buchanan, C. Song, and Z. R. Wasilewski, "Qwip-led pixelless imaging," in *Symposium on Integrated Optoelectronic Devices*. International Society for Optics and Photonics, 2002, pp. 150–157.
- [31] H. C. Liu, A. G. Steele, M. Buchanan, and Z. R. Wasilewski, "Dark current in quantum well infrared photodetectors," *Journal of Applied Physics*, vol. 73, no. 4, p. 2029, 1993.
- [32] J. H. Smet, C. G. Fonstad, and Q. Hu, "Intrawell and interwell intersubband transitions in multiple quantum wells for far-infrared sources," *Journal of Applied Physics*, vol. 79, no. 12, pp. 9305–9320, 1996.
- [33] J. Smet, "Intrawell and interwell intersubband transitions in single and multiple quantum well heterostructures," Ph.D. dissertation, Massachusetts Institute of Technology, 1995.
- [34] B. Xing, H. C. Liu, P. H. Wilson, M. Buchanan, Z. R. Wasilewski, and J. G. Simmons, "Noise and photoconductive gain in algaas/gaas quantum well intersubband infrared photodetectors," *Journal of Applied Physics*, vol. 76, no. 3, pp. 1889–1894, 1994.
- [35] R. H. Kingston, "Detection of optical and infrared radiation," in *Berlin and New York, Springer-Verlag (Springer Series in Optical Sciences. Volume 10)*, 1978. 150 p., vol. 10, 1978.
- [36] D. Dini, R. Köhler, A. Tredicucci, G. Biasiol, and L. Sorba, "Microcavity polariton splitting of intersubband transitions," *Phys. Rev. Lett.*, vol. 90, p. 116401, Mar 2003.

- [37] E. Dupont, H. C. Liu, A. J. SpringThorpe, W. Lai, and M. Extavour, "Vacuum-field rabi splitting in quantum-well infrared photodetectors," *Phys. Rev. B*, vol. 68, p. 245320, Dec 2003.
- [38] Semiconductor parameters. <http://www.ioffe.ru/SVA/NSM/Semicond/index.html>.
- [39] The simulation code to calculate the Envelope Function Approximation (EFA) and $k \cdot p$ method for MQW developed by I.C.W. Chan.
- [40] A. A. Erchak, D. J. Ripin, S. Fan, P. Rakich, J. D. Joannopoulos, E. P. Ippen, G. S. Petrich, and L. A. Kolodziejski, "Enhanced coupling to vertical radiation using a two-dimensional photonic crystal in a semiconductor light-emitting diode," *Applied physics letters*, vol. 78, no. 5, pp. 563–565, 2001.
- [41] I. Schnitzer, E. Yablonovitch, C. Caneau, and T. J. Gmitter, "Ultrahigh spontaneous emission quantum efficiency, 99.7% from AlGaAs/GaAs/AlGaAs double heterostructures," *Applied Physics Letters*, vol. 62, no. 2, pp. 131–133, 1993.
- [42] E. F. Schubert, Y.-H. Wang, A. Y. Cho, L.-W. Tu, and G. J. Zydzik, "Resonant cavity light-emitting diode," *Applied Physics Letters*, vol. 60, no. 8, pp. 921–923, 1992.
- [43] H. Benisty, H. de Neve, and C. Weisbuch, "Impact of planar microcavity effects on light extraction—part i: basic concepts and analytical trends," *Quantum Electronics, IEEE Journal of*, vol. 34, no. 9, pp. 1612–1631, 1998.
- [44] S. Moller and S. Forrest, "Improved light out-coupling in organic light emitting diodes employing ordered microlens arrays," *Journal of Applied Physics*, vol. 91, no. 5, pp. 3324–3327, 2002.
- [45] R. Windisch, P. Heremans, A. Knobloch, P. Kiesel, G. H. Döhler, B. Dutta, and G. Borghs, "Light-emitting diodes with 31% outcoupling of lateral waveguide modes," *Applied Physics Letters*, vol. 74, no. 16, pp. 2256–2258, 1999.
- [46] M. Boroditsky, T. F. Krauss, R. Coccioli, R. Vrijen, R. Bhat, and E. Yablonovitch, "Light extraction from optically pumped light-emitting diode by thin-slab photonic crystals," *Applied Physics Letters*, vol. 75, no. 8, pp. 1036–1038, 1999.
- [47] S. Fan, "Photonic crystals: Theory and device applications," Ph.D. dissertation, Massachusetts Institute of Technology, 1997.
- [48] J. J. Wierer, A. David, and M. M. Megens, "InGaN nitride photonic-crystal light-emitting diodes with high extraction efficiency," *Nature Photonics*, vol. 3, no. 3, pp. 163–169, 2009.
- [49] A. Taflov and S. C. Hagness, *Computational electrodynamics*. Artech house Boston, 2000, vol. 160.

- [50] J. D. Joannopoulos, S. G. Johnson, J. N. Winn, and R. D. Meade, *Photonic crystals: molding the flow of light*. Princeton university press, 2011.
- [51] B. S. Williams, “Terahertz quantum cascade lasers,” Ph.D. dissertation, Massachusetts Institute of Technology, 2003.
- [52] A. G. Baca and C. I. H. Ashby, “Fabrication of gaas devices.” Institution of Electrical Engineers, 2005.
- [53] *Processing Procedures for CYCLOTENE 3000 Series Dry Etch Resins*, Dow Chemicals, Apr. 2008.
- [54] *Processing Procedures for BCB Adhesion*, Dow Chemicals, 2007.
- [55] A. Katsnelson, V. Tokranov, M. Yakimov, M. Lamberti, and S. Oktyabrsky, “Hybrid integration of iii-v optoelectronic devices on si platform using bcb,” in *Proc. of SPIE Vol.*, vol. 4997, 2003, p. 199.
- [56] Cryogenic wires specifications. <http://www.lakeshore.com/products/cryogenic-accessories/wire/pages/Specifications.aspx>.
- [57] Infrared Laboratories Inc., http://www.infraredlaboratories.com/Cryogenic_Solutions.shtml.
- [58] Y. Yang, H. Liu, W. Shen, N. Li, W. Lu, Z. Wasilewski, and M. Buchanan, “Optimal doping density for quantum-well infrared photodetector performance,” *Quantum Electronics, IEEE Journal of*, vol. 45, no. 6, pp. 623–628, 2009.
- [59] *Model 113 Low-Noise Preamplifier Operating and Service Manual*, EG&G Princeton Applied Research, 1980.
- [60] H. W. Ott, *Electromagnetic compatibility engineering*. Wiley, 2011.
- [61] High-resolution transmission molecular absorption (HITRAN) database, <http://www.cfa.harvard.edu/HITRAN/>.
- [62] M. Graf, E. Dupont, H. Luo, S. Haffouz, Z. R. Wasilewski, A. J. Spring Thorpe, D. Ban, and H. Liu, “Terahertz quantum well infrared detectors,” *Infrared Physics & Technology*, vol. 52, no. 6, pp. 289–293, 2009.
- [63] M. B. M. Rinzan, A. G. U. Perera, S. G. Matsik, H. C. Liu, Z. R. Wasilewski, and M. Buchanan, “Algaas emitter/gaas barrier terahertz detector with a 2.3 thz threshold,” *Applied Physics Letters*, vol. 86, no. 7, p. 071112, 2005.
- [64] X. Guo, Z. Tan, J. Cao, and H. Liu, “Many-body effects on terahertz quantum well detectors,” *Applied Physics Letters*, vol. 94, no. 20, pp. 201101–201101, 2009.

- [65] M. S. Dresselhaus, A. Jorio, M. Hofmann, G. Dresselhaus, and R. Saito, “Perspectives on carbon nanotubes and graphene raman spectroscopy,” *Nano letters*, vol. 10, no. 3, pp. 751–758, 2010.
- [66] F. Rana, “Graphene terahertz plasmon oscillators,” *Nanotechnology, IEEE Transactions on*, vol. 7, no. 1, pp. 91–99, 2008.
- [67] L. Ju, B. Geng, J. Horng, C. Girit, M. Martin, Z. Hao, H. A. Bechtel, X. Liang, A. Zettl, Y. R. Shen, and F. Wang, “Graphene plasmonics for tunable terahertz metamaterials,” *Nature Nanotechnology*, vol. 6, no. 10, pp. 630–634, 2011.